WHITE-LIGHT INTERFEROMETRY: APPLICATIONS TO FIBRE OPTIC SENSORS FOR AC AND DC MEASURANDS

by

António Barbosa Lobo Ribeiro

Thesis submitted for the degree of Master of Science in the Physics Laboratory of the University of Kent at Canterbury, England

1992

UNIVERSITY OF KENT AT CANTERBURY

FACULTY OF NATURAL SCIENCES

The following candidate has satisfied the examiners and completed all requirements:

MASTER OF SCIENCE IN PHYSICS

Name: ANTONIO BARBOSA LOBO RIBEIRO

Title of Thesis:

White-light Interferometry: Applications to fibre optic sensors for AC and DC measurands

Approved on behalf of the Faculty

Dean — Date 8.10.92

Approved on behalf of Senate

Vice-Chancellor — Date 12-10-92

PG92/220
MPH/SMB
7 October 1992

Dedicated to my parents

Abstract

In this work, we study the "white-light" interferometry technique, and apply it to fibre optic interferometric systems.

The theoretical study includes the properties of different low coherence sources used in this kind of optical system. The advantages of using multimode laser diodes as "white-light" sources are considered and investigated.

We also present experimental results obtained by applying this interferometric technique to fibre optic sensors, used in the measurement of acceleration, and in slowly varying measurands, such as pressure and temperature.

Experimental results obtained relate to the accuracy, resolution and linearity of a new receiving interferometric unit, used to read the status of the sensor in this type of system, are presented.

Also, the design and characterization of a pressure and temperature sensor probe, based on a low-finesse Fabry-Perot cavity is performed and a multiplexing scheme, to be used in the signal processing of the sensors, is reviewed.

Acknowledgments

I would like to express particularly my gratitude to Prof. David A. Jackson, Professor of Applied Optics of the University of Kent at Canterbury, England, for his indispensable support and constant guidance during all the phases of my work, without which this work could not have be done.

I would like to thank my collegue and friend, Mr. José Luis Santos for his encouragment and helpful advices, in the right moments, which he has dispensed to me during these years.
I would also to thank him for his valuable support during the writing-up stage of the thesis.

I also wish to thank all people, which in some way, helped me during my work, particularly to:

- Prof. António P. Leite, for his first encouragment in this field and his support during the writing-up of the thesis.
- Prof. José R. Salcedo, for the hardware and software facilities used in the preparation of this thesis.
- Miss Deb Bowyer, for her untiring and friendly help on any admnistration problem during my permanence in Canterbury.
- Mr. L. F. Link, for his long experience in mechanics, which helped me to develop the polarization controller used in this work.
- My father, for his financial support in the necessary travel expenses.
- All postgraduate students of the Applied Optics Group, for their encouragment and help in some difficult moments of the work.

CONTENTS

1. White-Light Interferometry

1.1 Introduction

Interferometric sensors offer the highest accuracy in optical metrology [1,2]. A basic problem in all systems of this type is how to transduce optical information from the interferometer to an electrical signal with sufficient accuracy and reproducibility over a resonably large measurement range, and with tracking techniques capable of re-initialization (thus avoiding that optical information being lost). A general technique providing a large measurement range is based on a classical scheme often called "white-light interferometry", where the system is illuminated either by the equivalent of a large number of monochromatic sources, as in a multimode laser, or a broad-band source. The transfer function of an interferometer illuminated by one of these sources has unique features, which can be utilized when sensor re-initialization is necessary. Moreover, the unambiguous measurement range is, in principle, unlimited. The idea of using a short coherence length source to transmit signals using a set of Michelson interferometers to modulate a white-light source was presented by Cielo [3]. The emitting interferometers are adjusted for path-length imbalances larger than the coherence length of the source. Demodulation is achieved using a receiving interferometer with an adjustable path-length imbalance. Interference occurs when this path-length imbalance is adjusted to each of the emitting ones and the signals are retrieved at the interferometer output. A more sophisticated solution was proposed in the early 1980s to demonstrate signal multiplexing in fibre links [4], using a low coherence source and electro-optic modulators to generate a sequence of optical delays larger than the source coherence length.

Al-Chalabi et al.[5] were the first to use the white-light technique in the fibre optic sensors field. Since then, a number of architectures based on coherence modulation of light (ie, white-light interferometry), using bulk and fibre interferometers, have been published in the literature. In the present work, a theoretical study is first presented for different types of low coherence sources. Secondly, an all-fibre white-light interferometric receiving system capable of tracking large amplitude AC signals will be investigated. Finally, the application of the technique for measuring slowly varying measurands, such as temperature or pressure, is also investigated.

1.2 Low Coherence Sources in Interferometers

In a two-beam interferometer (in our case, a Michelson interferometer), with path length difference ΔL, the resulting interference signal depends on the temporal coherence of the source, which is characterized by the normalized auto-correlation function $\gamma_{11}(\tau)$, where $\tau=\Delta L/c$ and c is the free-space velocity of light. If I_1 and I_2 are the intensities of these two beams, then, after their recombination (assuming the polarization properties of the light are maintained), the irradiance is expressed as follows [6]:

$$I = (I_1 + I_2)\left[1 + \frac{2\sqrt{I_1 I_2}}{I_1 + I_2} |\gamma_{11}(\tau)| \cos \Delta\phi(\tau) \right] \tag{1}$$

where

$$\Delta\phi(\tau) = \frac{2\pi n_c}{\lambda_o} \Delta L$$

where n_c is the index of refraction of the optical medium of the interferometer, and λ_o is the vacuum wavelength of the light. The following quantities are usually defined:

$$I_m = I_1 + I_2 \tag{2}$$

$$V = \frac{2\sqrt{I_1 I_2}}{I_1 + I_2} |\gamma_{11}(\tau)| = V_o |\gamma_{11}(\tau)| \tag{3}$$

where V is called the visibility (or contrast) of the interference signal and V_o is the visibility of the central fringe (or visibility constant), which corresponds to zero path length imbalance ($\tau=0$ and hence $\gamma_{11}(\tau)=1$). In a pattern of interference fringes, the irradiance I varies between two limits, I_{max} and I_{min}, as $\cos \Delta\phi(\tau)$ varies from +1 to -1. Due to the signal processing scheme used in our experiments, relations (2) and (3) are more conveniently expressed as follows:

$$I_m = \frac{I_{max} + I_{min}}{2} \tag{4}$$

$$V = \frac{I_{max} - I_{min}}{I_{max} + I_{min}} \tag{5}$$

Using these quantities, equation (1) may be written in the more familiar form

$$I = I_m [\, 1 + V \cos \Delta\phi(\tau) \,] \tag{6}$$

The visibility varies in the range of $0 \leq V \leq 1$, and is governed by the coherence properties of the source (ie, $|\gamma_{11}(\tau)|$), and by the quality of the interferometer (ie, V_o).

In practice, various effects lead to the situation $V<1$; these are:

(i) the intensities of the two beams (I_1 and I_2) are different

(ii) the path length difference between the two beams is greater than the coherence length of the source

(iii) the polarization states of the recombining beams are unmatched.

Assuming that we have a good quality interferometric system, ie, $V_0=1$, the irradiance will depend only on the spectral distribution of the source, which can be related to the auto-correlation function by the Wiener-Khintchine theorem† [7,8].

The auto-correlation function must be calculated from the statistical properties of the light source, which are governed by the radiation broadening mechanisms of the source, classified into homogeneous and inhomogeneous broadening [9].

When all of the radiating atoms have the same transition centre frequency and the same resonance lineshape, the broadening is homogeneous. This broadening is due, most often, to the finite interaction lifetime of the emitting or absorbing atoms. Some of the most common mechanisms are:

(1) the spontaneous lifetime of the excited state

(2) the collision of an atom embedded in a crystal with a phonon (collision broadening)

(3) pressure broadening of atoms in a gas.

The corresponding spectral profile is described by a Lorentzian spectral distribution function[9,10]. There are, however, many physical situations in which the individual atoms are distinguishable, each having a slightly different transition frequency. In this case, the spectrum of the spontaneous emission (its spectral distribution) will reflect the spread in the individual transition frequencies and not the broadening due to the finite lifetime of the excited state (which is one of the possible causes for the frequency spread of spontaneous emission). This type of broadening is referred to as inhomogeneous. The corresponding spectral profile is described by a Gaussian distribution function [9,10]. There are several possible causes for inhomogeneous broadening, such as: Doppler broadening; strain broadening; inhomogeneous DC magnetics fields; source crystal imperfections [9,10].

---

† The Wiener-Khintchine theorem states that the normalized auto-correlation function $\gamma_{11}(\tau)$ is given by the inverse Fourier transform of the normalized power spectral density function P(ν) as follows

$$\gamma_{11}(\tau) = \int_{-\infty}^{+\infty} P(\nu)\, e^{-2\pi i \nu \tau}\, d\nu \qquad \text{where} \quad \int_{-\infty}^{+\infty} P(\nu)\, d\nu = 1$$

There is, also, an intermediate lineshape between Lorentzian and Gaussian lineshapes, which is generally referred to as Voight-Profile. The exact shape of the Voight-Profile depends on both the homogeneous and the inhomogeneous linewidths, or more precisely, on the ratio of these two linewidths [10].Some sources, like multimode laser diodes with a low number of longitudinal modes, and some superluminescent diodes, exhibit a $\cos^2$-shaped power spectrum [11]. The normalized power spectral density functions of optical sources exhibiting Gaussian, Lorentzian and $\cos^2$-shaped lineshapes, can be described as follows [11]:

$$P_{lortz}(\nu) = \frac{2\Delta\nu_L}{\pi\left[4(\nu - \nu_o)^2 + \Delta\nu_L{}^2\right]} \tag{7}$$

$$P_{gauss}(\nu) = \frac{2\sqrt{\ln 2}}{\sqrt{\pi}\,\Delta\nu_G}\exp\left[-\left(2\sqrt{\ln 2}\,\frac{(\nu - \nu_o)}{\Delta\nu_G}\right)^2\right] \tag{8}$$

$$P_{cos2}(\nu) = \frac{1}{\Delta\nu_C}\cos^2\left(\frac{\pi\nu}{2\Delta\nu_C}\right) \otimes \delta(\nu - \nu_o) \;\; ; \text{for } \nu_o - \Delta\nu_C < \nu < \nu_o + \Delta\nu_C \tag{9}$$

$$= 0 \quad ; \text{elsewhere}$$

where $\otimes$ stands for convolution† ; $\delta(\nu - \nu_o)$ is the Dirac δ-function†† ; ν_o is the mean optical frequency of the source and $\Delta\nu$ is the frequency separation between the points where $P(\nu)$ is down to half of its peak value, ie., the mode line-width. These frequency separations,$\Delta\nu$, are related to the coherence time of the source (τ_c) by the following relations [8]:

$$\tau_c\,\Delta\nu_L = \frac{1}{\pi} \tag{10}$$

$$\tau_c\,\Delta\nu_G = \sqrt{\frac{2\ln 2}{\pi}} \tag{11}$$

$$\tau_c\,\Delta\nu_C = 1 \tag{12}$$

---

† The convolution product between two functions $H(\nu)$ and $G(\nu)$ is defined as:

$$H(\nu) \otimes G(\nu) = \int_{-\infty}^{+\infty} H(w)\,G(\nu - w)\,dw = \int_{-\infty}^{+\infty} G(w)\,H(\nu - w)\,dw$$

†† Dirac Delta-function $\delta(u)$, is defined by: $\int_{-\infty}^{+\infty} \delta(u)\,du = 1$, and $\delta(u) = 0$ for $u \neq 0$

Calculating the inverse Fourier transform of equations (7), (8) and (9) we obtain the corresponding normalized auto-correlation functions [8,11]:

$$|\gamma_{11}(\Delta L)|_{lortz} = \exp\left[-\frac{|\Delta L|}{L_c}\right] \tag{13}$$

$$|\gamma_{11}(\Delta L)|_{gauss} = \exp\left[-\frac{\pi}{2}\left(\frac{\Delta L}{L_c}\right)^2\right] \tag{14}$$

$$|\gamma_{11}(\Delta L)|_{cos} = \left|\frac{\sin(2\pi\Delta L/L_c)}{2\pi\frac{\Delta L}{L_c}\left[1-4\left(\frac{\Delta L}{L_c}\right)^2\right]}\right| \tag{15}$$

Figure (1.1) illustrates the normalized auto-correlation function versus the path-length imbalance of the interferometer, $\Delta L=|\tau|/c$, normalized with respect to the coherence length of the light, $L_c=\tau_c/c$. As we see, the visibility function V (for $V=|\gamma_{11}(\Delta L)|$ and $V_o=1$), is maximum when the path-length imbalance is zero and decreases towards zero when the path-length imbalance exceeds the coherence length of the light.

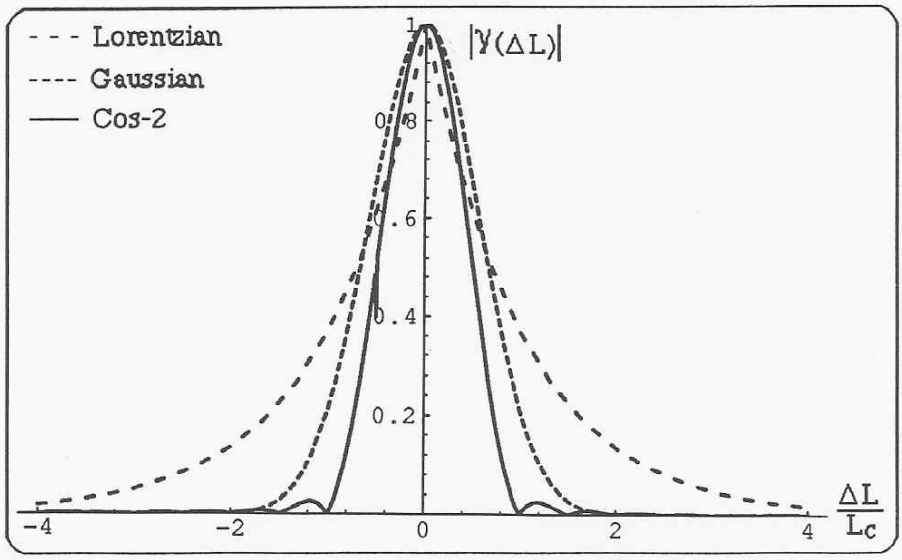

Figure 1.1 - The normalized auto-correlation function versus the path-length imbalance of the interferometer, normalized with respect to the coherence length of the light

For example, if an interferometer is illuminated by a low coherence source (coherence length L_c) with a Lorentzian and Gaussian line profile, the output irradiance will have a pattern of interference fringes as shown in figure (1.2a and 1.2b).

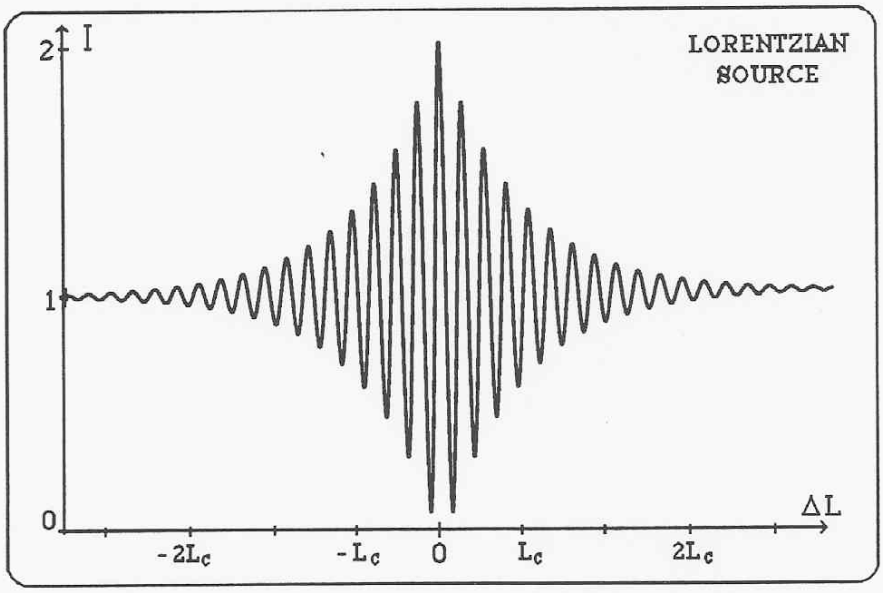

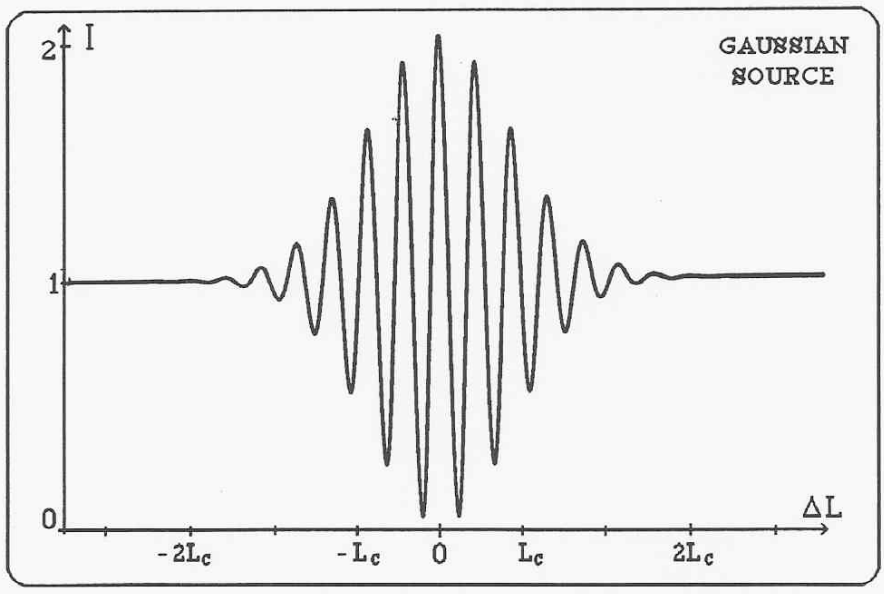

Figure 1.2 - Computer simulation of the irradiance in the output of an interferometer using a low coherence light source, as a function of the optical path imbalance

a) Lorentzian lineshape ; b) Gaussian lineshape.

The interference fringes occur only from $\Delta L=-\lambda_0/2$ to $\Delta L=+\lambda_0/2$ (λ_0 is the mean optical wavelength of the source) and the position of maximum fringe sensitivity occurs at $\Delta L=\lambda_0/4$, sometimes called the "first quadrature point with negative slope" [12].

Due to the relatively short coherence length of many common light sources, which correspondingly have a narrow function, the position of zero path-length imbalance of the interferometer may be uniquely determined, even when there is a momentary "power-off" followed by re-initialization of the system. Apart from the coherence properties of an optical source, it is also important, in the context of optical fibre sensors, to consider the ability to couple useful amount of power into the fibre, in order to have a large signal to noise ratio at the output of the system (and, hence, high phase resolution).

In figure (1.3) we can see the typical coherence lengths of various optical sources available in the market. These types of sources vary also from the points of view of coupling efficiency into a fibre and price.

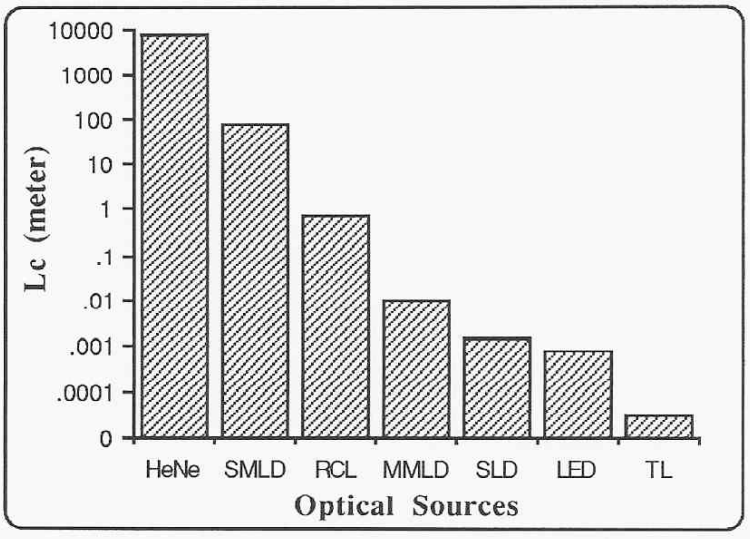

Figure 1.3 - Typical coherence lengths of various optical sources

HeNe-HeliumNeon single mode laser, SMLD-SingleMode Laser Diode

RCL-Red Cadmium Line, MMLD-MultiMode Laser Diode

SLD-SuperLuminescent Diode, LED-Light Emitting Diode,TL-Tungsten Lamp

The use of a Light Emitting Diode (LED), with coherence length of ≈30 μm or less, is possible for "white-light" interferometry, but the power coupling efficiency is low. On the

other hand, Superluminescent Diodes (SLD), which have sufficient power and a short coherence length, are well suited for this kind of application, but, at the present time, their price is much higher than that of LED's and even laser diodes sources [13].

Solid-state laser diodes seem to be the best choice, as claimed by many authors, to illuminate fibre optic interferometric systems, mainly because the coherence length can be tuned by changing the diode injection current; "sufficient" optical power output in conjunction with a small divergence beam is typical, and they are relatively inexpensive [13].

As we require a short coherence length, a multimode laser diode may be the best choice, due to the low price and a suitable level of optical power injected into a monomode fibre. However, the coherence properties of these sources are more complex and lead to certain restrictions in the operation on "white-light" interferometry.

The emission spectrum of a multimode laser is composed of a set of longitudinal modes of oscillation, superimposed on some level of continuous wide-band spontaneous emission spectrum, characteristic of a gaussian random noise. The envelope of the oscillation modes intensities is a nearly Lorentzian or $\cos^2$ function [11].

A simple model for a multimode laser can be developed, where it is assumed that:

(i) the spectrum is symmetrical around the peak frequency, ν_o

(ii) the emission frequencies of the lasing modes are equally spaced by $\delta\nu$

(iii) all the longitudinal modes have the same spectral width

It is known, however, that multimode lasers do not exactly fullfil the above conditions, specially when subject to dispersion effects, such as the second-order dispersion phenomenon [10,14]. Considering the multimode nature of the laser spectrum, the auto-correlation function of the optical field is determined by an unbalanced interferometer.

Assuming that we have a good quality interferometer, ie., $V_o=1$, and neglecting the contribution from spontaneous emission on the total optical power emitted from the laser diode, the auto-correlation function can be expressed approximately as follows [12,15]:

$$|\gamma_{11}(\Delta L)| = \frac{1}{\sum_{k=-m}^{+m} P_k}\left[P_o + 2\sum_{k=1}^{m} P_k \cos\left(\frac{2\pi}{c}\Delta L \delta\nu\, k\right)\right] e^{-\Delta L/Lcm} \qquad (16)$$

where P_k is the power in mode "k"; $\delta\nu$ is the frequency separation between successive modes; L_{cm} is the coherence length associated with each longitudinal mode (the total number of modes is 2m+1); ΔL is the path-length imbalance of the interferometer and P_o is the optical power in the central mode.

The interference pattern which is generated by each mode adding in phase results in strong peaks for the visibility function occurring at $\frac{2\pi}{c}\Delta L\delta\nu$ equal to an integer multiple of 2π, corresponding to optical path-length imbalance ΔL for the interferometer given by:

$$\Delta L = 2pn_{cav}\, L_{cav} = pc/\delta\nu \qquad (17)$$

where p is an integer and n_{cav}, L_{cav} are the refractive index and length of the laser cavity, respectively. When condition (17) is not satisfied, the longitudinal modes rapidly dephase resulting in low visibility. This behaviour is shown in figure (1.4).

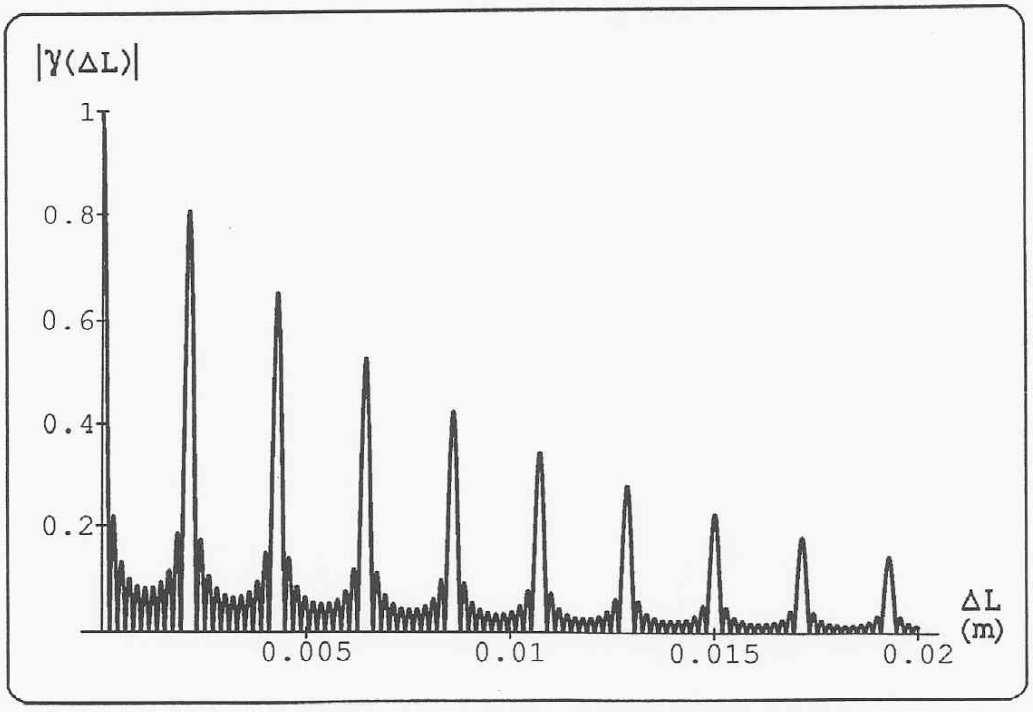

Figure 1.4 - Normalized auto-correlation function (visibility) versus path-length imbalance of an interferometer for a multimode laser source with m=5(11modes); half-power width for the gain curve (supposely gaussian in shape) is 1200 GHz ; mode separation is $\delta\nu$ = 140 GHz and mode line-width is 30 GHz [15].

The employment of a multimode laser diode in "white-light" interferometry applications, due to its unique visibility function pattern, bring us advantages with respect to the "effective" coherence length of the source, because we can choose the coherence length mode (L_{cm}) or the

coherence length of the modal envelope (L_c), depending on the particular application, as we will explain in the following section. It can be used as an alternative to conventional low coherence sources (such as LEDs), normally used in "white-light" interferometry, provided certain operating conditions are met.

1.3 The Tandem White-Light Interferometer

This type of configuration, which uses a low coherence light source, usually consists of two unbalanced interferometers, remotely coupled via a fibre optic link, and having their optical path-length imbalances closely matched[16,17,18].

The system is powered by a low coherence source, with a coherence length much shorter than the optical path-length imbalance of the interferometers, such that no interference signal will be observed at the output of each individual interferometer.

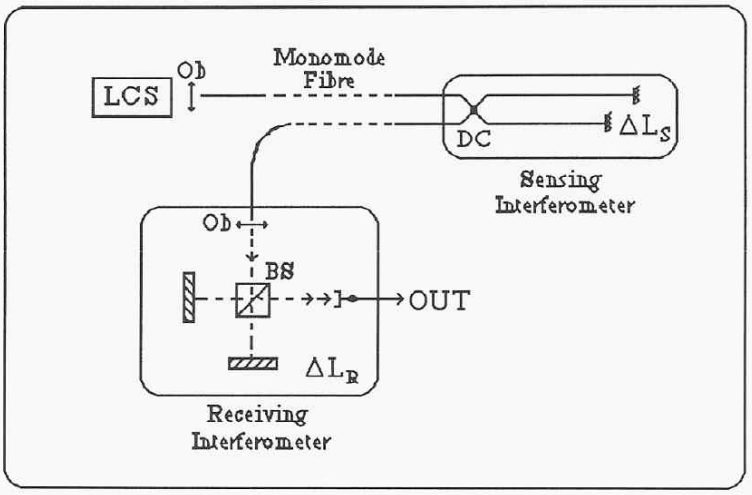

Figure 1.5 - Tandem "white-light" interferometer composed of two Michelson interferometers (DC-directional coupler, LCS-Low coherence source,Ob-Objectives, BS-Beam Splitter)

The basis of the technique is that, in order to detect interference fringes at the output of the system, the optical path-length imbalance of the receiving interferometer (see figure (1.5)) must be tuned to match that of the sensing interferometer, within the coherence length of the light source. So, a path-length change in the sensor may be tracked remotely by the receiver.

Figure (1.5) shows an example of this kind of configuration, where the sensing interferometer is a fibre optic Michelson interferometer, while the receiving interferometer is a bulk-optic one. Assuming, for simplicity, that the amplitude reflection coefficients for the directional coupler and for the beam splitter are $1/\sqrt{2}$ and neglecting all the optical losses in the system, it can be shown [19] that the irradiance (I) at the output of the whole system is given by:

$$I = \frac{I_o}{4} \left\{ 1 + 1/2\, |\gamma_{11}(\Delta L_s - \Delta L_r)| \cos\left[\frac{2\pi\nu_o}{c}(\Delta L_s - \Delta L_r)\right] + |\gamma_{11}(\Delta L_s)| \cos\left(\frac{2\pi\nu_o}{c}\Delta L_s\right) + |\gamma_{11}(\Delta L_r)| \cos\left(\frac{2\pi\nu_o}{c}\Delta L_r\right) + 1/2\, |\gamma_{11}(\Delta L_s + \Delta L_r)| \cos\left[\frac{2\pi\nu_o}{c}(\Delta L_s + \Delta L_r)\right] \right\} \quad (18)$$

where I_o is the input power to the system; $\gamma_{11}(\Delta L)$ is the auto-correlation function of the low coherence source; ν_o its mean light frequency and ΔL_s and ΔL_r are the optical path-length imbalances of the sensing and receiving interferometers, respectively.

Because the system is illuminated with a low coherence source, such that its coherence length is shorter than the optical path-length imbalance of the sensing interferometer, the interference effects will only be observed at the output of the receiving interferometer when:

(1) its path-length imbalance is zero, $\Delta L_r = 0$

(2) its path-length imbalance is equal to the imbalance in the sensing interferometer, ie., $\Delta L_r = \pm \Delta L_s$.

In figures (1.6) and (1.7) we show the predicted output of the receiving interferometer as a function of its path-length imbalance (ΔL_r), when it is illuminated by a low coherence source with an auto-correlation function given by (13) such as a LED or a SLD, (fig.1.6), or multimode laser diode with an auto-correlation function given by (16), (fig.1.7).

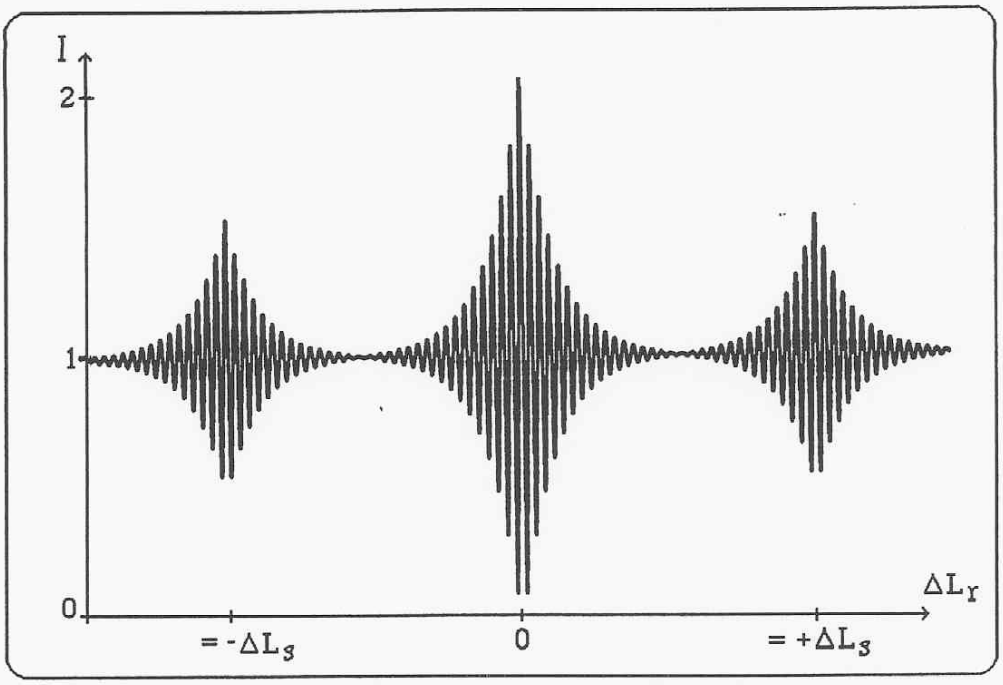

Figure 1.6 - Output of the receiving interferometer vs. optical path-length imbalance, when it is illuminated by a LED or a SLD.

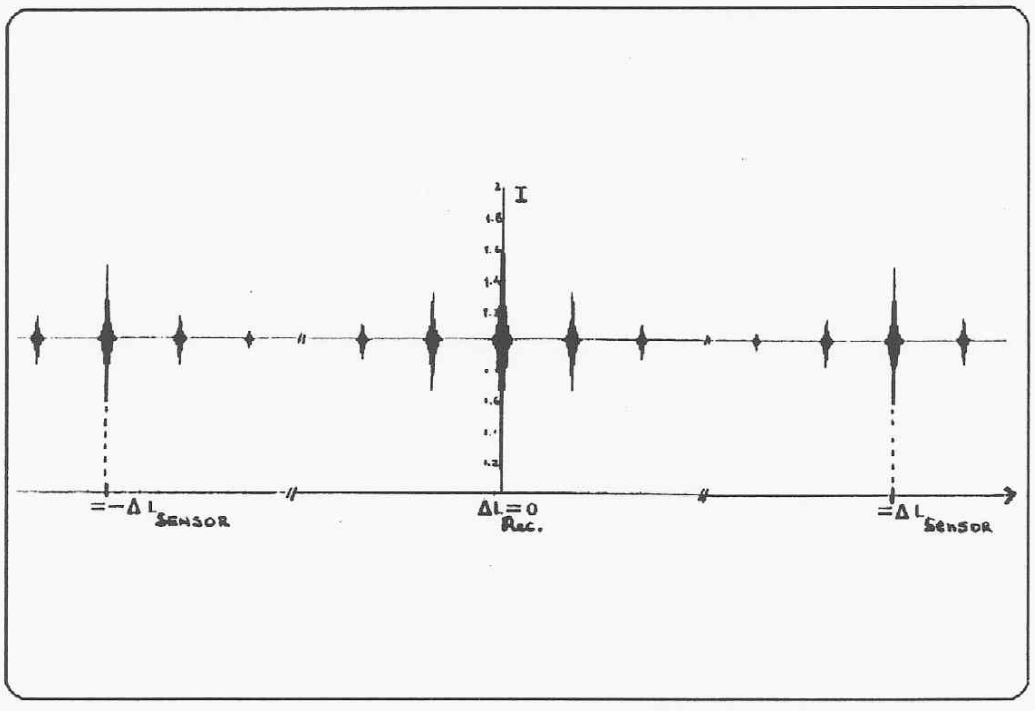

Figure 1.7 - Output of the receiving interferometer vs. optical path-length imbalance, when it is illuminated by a multimode laser diode.

Far from the central pattern of interference fringes , which are produced only via the receiving interferometer, interference can occur only in two regions where ($\Delta L_s \pm \Delta L_r$) is less than the coherence length of the low coherence source.

However, if a multimode laser diode is used, we must choose the path-length imbalances of the sensing and receiving interferometers in such a way as to coincide with a region of low visibility, which can occur in two cases:

(I) in the range between two successive packets of interference, as we see in figure 1.4.

(II) out of the modal envelope of the corresponding auto-correlation function.

Matching the two path-length imbalances such that ($\Delta L_s \pm \Delta L_r$) is less than the coherence length of a longitudinal mode, L_{cm} (case I), or less than the coherence length of the modal envelope, L_c (case II), will came interference to occur at the output of the receiving interferometer. In chapter 2, we will use case II and in chapter 3 the path-lengths are chosen such that case I is obeyed.

When this technique is used, the accuracy of the measurement is governed by two factors:

(i) the ability to identify the condition $\Delta L_r = \pm \Delta L_s$.

(ii) the precision obtainable in the measurement of the optical path-length imbalance of the receiving interferometer.

The technique has the following positive attributes [19]:

(1) it allows sensor initialization on "power-up".

(2) the system can be operated in such a way that the measurement accuracy is independent of the source stability, or such that the effects of wavelength instability of the source are greatly reduced.

(3) the output signals from many sensors can be multiplexed.

But, unfortunately, there are also disadvantages, such as:

(1) the requirement of a receiving very stable interferometer with a facility for precision displacement measurements.

(2) the optical power available from typical short coherence sources is very low.

It is clear, from the above considerations, that by using a multimode laser diode with specific properties and an all-fibre optic receiving interferometer with sufficient dynamic tracking range, these two disadvantages can be almost suppressed.

2. *Large Dynamic Range Coherence Tuning System for AC Measurands*

2.1 Introduction

In this chapter a "white-light" all-fibre optic receiving interferometer with large tracking range is presented, which can be used for signal processing of AC measurands, such as acceleration, acoustic pressure or surface velocity.

We begin by discussing the characterization of the optical source through the measurement of its auto-correlation function. The sensor consists of a bulk Michelson interferometer, which serves as an accelerometer simulator. Following the study, design and characterization of the receiving interferometric system, the study involved consideration of three different parts:

(i) Theoretical and experimental study of the efficiency and electrical impedance responses of the piezoelectric ceramic elements.

(ii) Design and experimental characterization of the polarization controller, through the use of the Poincaré geometrical representation.

(iii) Development and testing of the electronic servo control circuit used to maintain the tandem interferometers at the quadrature point of the output signal.

Finally, the predicted resolution data for a fibre optic compliant-cylinder type accelerometer is presented.

2.2 The Laser Source

The light source used in this experiment was the multimode laser diode ML4406 from Mitsubishi, with a mean wavelength of 781 nm. The emitted light power is 3 mW when the laser is operated at 10 mA above the threshold value [20].

To measure the auto-correlation function [21], ie., the visibility function, a variable path-length bulk Michelson interferometer, with piezoelectric (PZT) modulator mounted mirrors (M1,M2), was used (see figure 2.1). Applying a sine-wave modulation to one of the mirrors (M1), and adjusting the amplitude of the driving waveform in order to modulate the interferometer output over one fringe† , we measured the visibility of the detected signal (ie., the resulting transfer

† For the Michelson configuration, one cycle (or fringe) of the transfer function occurs for a displacement of $\lambda_o/2$; ie., a one fringe change is equivalent to $\lambda_o/2$.

function) with the oscilloscope, by making use of relation (5). The total scan (25 mm) was performed using the translation stage (TS) attached to the mirror. For constant power in the interferometer, the amplitude of the resulting signal is proportional to the fringe visibility; however, it was observed that the fringe amplitude fluctuated slightly, depending on the value of the static phase of the interferometer during the modulation. To eliminate this effect, a low bandwidth (80 Hz) servo was incorporated into the system (see figure 2.1), providing an error voltage signal to the second mirror drive (M2), in order to keep the interferometer in quadrature††.

This technique is usually called the Active Phase Tracking Homodyne (APTH) [13] demodulation scheme, and it will be further explained in the following section.

It should be pointed out that the use of an optical isolator is not necessary when a multimode laser diode is the light source, because the effect of the feedback light on the level of the system noise floor is practically negligible [20,21].

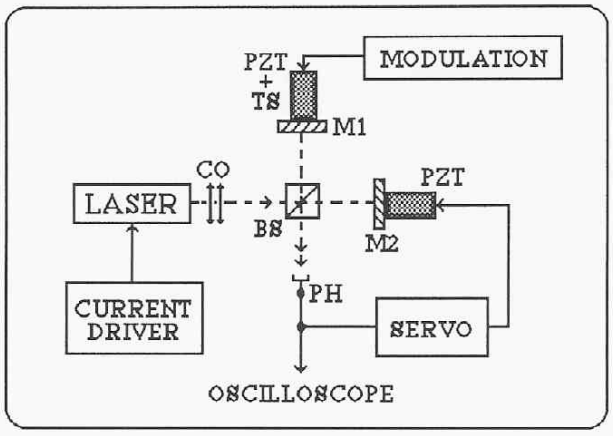

Figure 2.1 - Experimental arrangement used to measure the auto-correlation function of the laser diode.

(PH- Photo-Detector, TS-Translation Stage, M1,M2-Mirrors)

(BS- Beam Splitter, CO- Collimating lens,PZT- Piezoelectric)

†† The quadrature condition occurs when the optical path-difference between the two beams is $\lambda_0/4$, ie., when the sensitivity, defined by $dI_{out}/d\Delta\phi$, is maximum.

We started by measuring the optical output power versus forward laser current. As it can be seen from figure 2.2, the threshold current (I_{th}) for lasing occurs approximately at 60 mA at room temperature (25 °C). Above threshold, the optical output power increases linearly with current, as expected.

In figure 2.3 the fringe visibility of the laser diode ML4406 is shown as a function of the optical path-length imbalance of the Michelson interferometer for CW operation with the laser diode running at 10 mA above threshold. This peaked structure of the visibility function is typical of multimode laser illumination [21]. The peak separation is 2.2 mm, which gives a laser cavity length of 300 μm (for an active layer refractive index of 3.5), and a longitudinal mode separation of 140 GHz. Assuming a Lorentzian mode profile, the obtained value for the coherence length, L_c†, is approximately 2 mm. Using relation (10), the corresponding mode line-width is $\Delta\nu_L(CW) \approx 48$ GHz.

It has been shown [22] that if the laser is modulated, the form of the visibility function is virtually unchanged; however, the coherence length (L_c) of the laser is altered, this change occurs because the modulation causes broadening of the individual longitudinal modes, and the modal envelope is determined by the longitudinal mode line-width.

This direct injection current modulation (>1MHz) can be used to reduce the excess phase noise at the output of the tandem interferometer, because the last three terms in equation (18) are each associated with large path imbalances and are, therefore, highly sensitive to laser frequency jitter (ie, noise in the laser frequency) [23].

Thus by applying a high frequency modulation to the laser at frequencies higher than the signals of interest the effects of laser frequency jitter on the noise floor of the system can be reduced by suitably filtering the output signal. The noise reduction capability of this technique has been shown to be -40 dB compared to that obtained with a free-running laser [23].

---

† The coherence length L_c, which is determined by the envelope of the visibility function, is estimated by the 1/e=37% criterion.

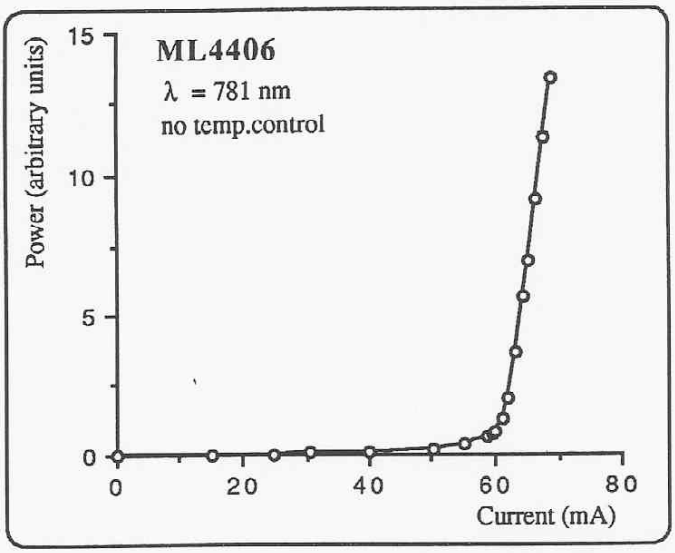

Figure 2.2 - Output characteristic of the laser diode ML4406

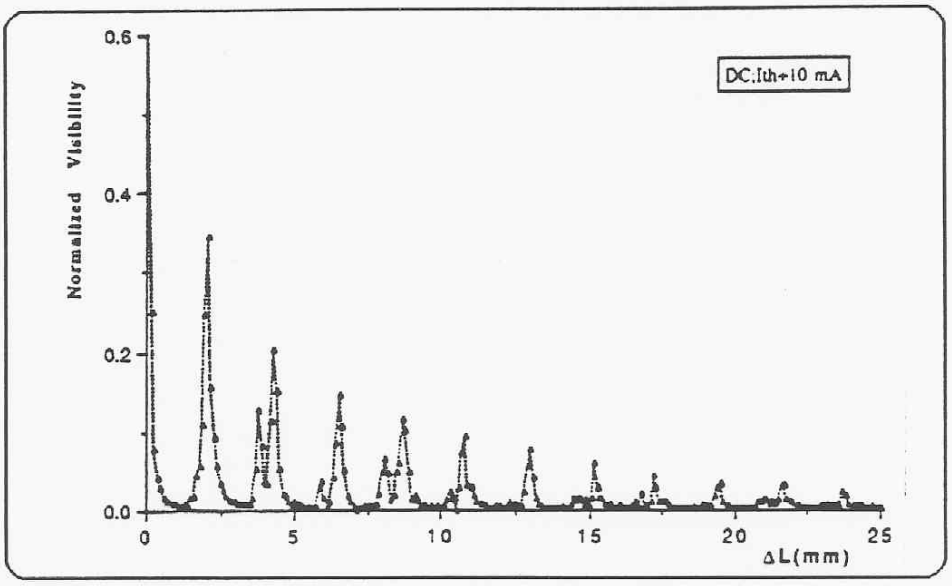

Figure 2.3 - Fringe visibility versus optical path-length imbalance for the laser diode operating CW at I_{th}+10 mA (visibility normalized to its value at ΔL=0).

In the tandem configuration used to coherently interrogate the simulator of a vibration sensor, the path-length imbalances were chosen to meet the "white-light" condition expressed in section 1.3 (case II). In other words, the path-length imbalance of the two interferometers (sensor and receiver) must be greater than 20 mm, at least. Although the coherence length (L_c) is 2 mm, the real value taken for the path-length imbalance for this particular "white-light" application should

be ≈ 20 mm because, below this value, we can still have some residual coherence due to the characteristic visibility function of this multimode laser diode.

2.3 The Fibre Optic Receiving Interferometer

The experimental arrangement of the large range coherence-tuned fibre optic interferometric system is shown in figure 2.4. It consists of a bulk Michelson interferometer constituted by two mirrors (M) and one beam splitter (BS), which serves as a sensor simulator, and an all-fibre (monomode) Michelson receiving interferometer, made by the directional fibre coupler (DC2).

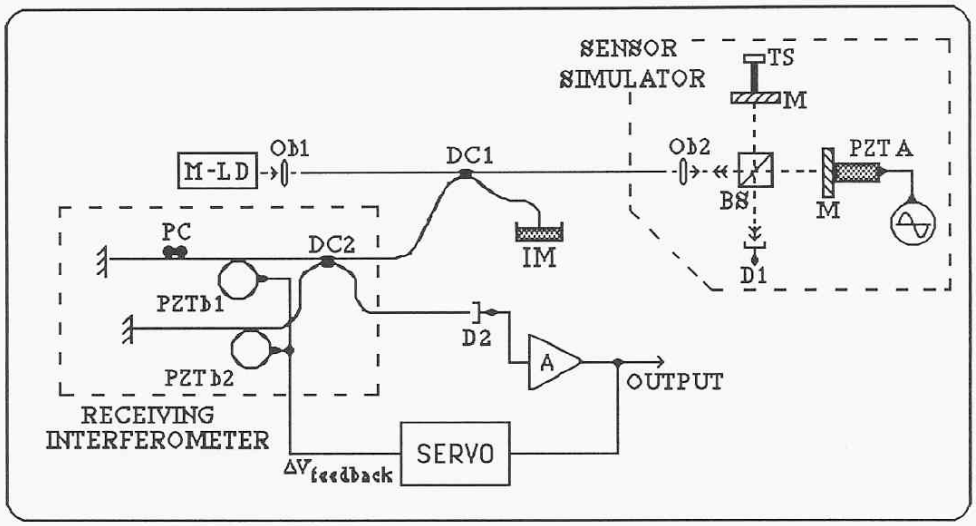

Figure 2.4 - Basic "white-light" system with bulk Michelson sensor simulator and an all-fibre receiving interferometer with tracking servo system.

(M-LD: Multimode Laser Diode; PC: Polarization Controller; IM: Index Matching Gel)

(DC1,DC2: Directional Fibre Couplers; Ob1,Ob2: Microscope Objectives; M: Mirror)

(D1,D2: Photodetectors; TS: Translation Stage; BS: Cube Beam Splitter)

The optical source used was the multimode laser diode ML4406, with mean wavelength of 781nm . The output of the laser is coupled into the monomode fibre link (using a microscope objective (Ob1) of 0.25 numerical aperture and 6 mm operating focal length), which incorporated a nominally 50/50 directional coupler (DC1). The laser light, after illuminating the bulk Michelson interferometer, is coupled back into the same fibre link by an identical microscope objective (Ob2), and transferred to the receiving interferometer via the coupler (DC1). Index-matching gel (IM) was used to eliminate the Fresnel reflection at the unused arm

of the directional coupler (DC1). One polarization controller † (PC) was used for the alignment of the polarization states in the two arms of the fibre Michelson interferometer, in order to increase the fringe visibility of the interference signal at the output of the system (D2).

Due to the physical length of the arms of this interferometer (≈ 26 m each), the static path-length imbalance was measured by an OTDR†† technique [24] and set at 36.9 mm, such that it exceeded the coherence length of the light source, as discussed in section 2.2. This result is shown in figure 2.5, where the two signal peaks correspond to the Fresnel reflections from the fibre ends of the two arms of the interferometer. One signal is stronger than the other, because in one arm of the interferometer the splice had a smaller loss than in the other (about 0.13 dB difference).

The two small signals are due to the time response of the photodetector. From the data below, we obtained a time delay difference of ΔT=360 ps, thus the physical path-length imbalance can be calculated using:

$$\Delta L_{receiver} = \frac{c\,\Delta T}{2\,n_c} \tag{19}$$

where c is the velocity of the light in free space and n_c is the effective refractive index of the core.

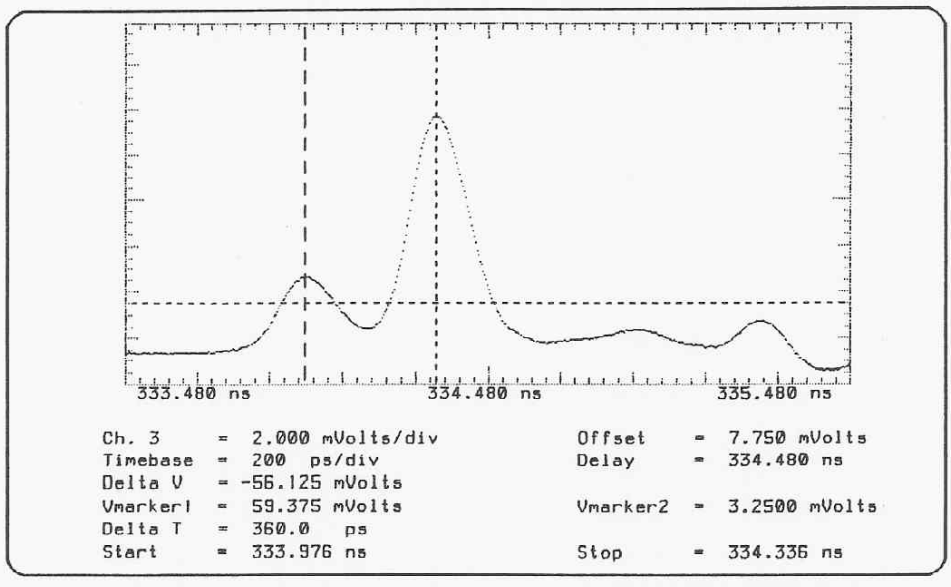

Figure 2.5 - Experimental data of the OTDR technique for the measurement of the path-length imbalance of the fibre Michelson interferometer.

(time difference: ΔT= 360 ps => $\Delta L_{receiver}$ = 36.9 mm)

† See section 2.3.2

†† OTDR : Optical Time Domain Reflectometry

The output signal from the fibre Michelson interferometer was fed into an electronic servo, which applied a voltage signal in antiphase to the two identical PZTs, in order to maintain the tandem interferometers at a quadrature point (ie, phase difference for half of the light power circulating in the system: $\pm \pi/2$) of their overall transfer function.

A sinusoidal test signal (amplitude 6 volt and frequency 3.75 kHz) was applied to the modulator (PZTA) in the bulk Michelson interferometer, which had an efficiency of 0.78 rad/volt and the corresponding fringe visibility at the output of the receiving interferometer (ie, in photodetector D2) when the system was coherently tuned to the sensor, was found to be 0.29 (the maximum possible value being 0.5).

As shown in figure 2.6, no interference occurs in photodetector D1, ie, in the sensor, but only at the receiving interferometer, as we expected for the "white-light" interference condition, when $\Delta L_{receiver} = \pm \Delta L_{sensor}$. The intensity output from the receiving interferometer is measured relative to some reference level, in this case I_{mean} (I_{mean}= 214 mV, see figure 2.6), where the reference level corresponds to the output at quadrature. The relative measurement is therefore zero when the interferometer is at quadrature. Otherwise, the relative measurement serves as an error signal in a servo loop feeding back to a phase control element (the PZT) in the interferometer, which is hence driven to quadrature.

This is the basic principle of the Active Phase Tracking Homodyne (APTH) signal processing scheme [13]. Two modes of operation are possible with this processing scheme, depending on whether the frequency of the measurand is within or above the bandwidth of the servo loop. If the response of the loop is sufficient to follow the measurand, then we are operating, in the so called "high gain bandwidth product (HGBP) mode". When the frequency of the test signal is higher than the bandwidth of the loop, only the drift information (low frequency phase drifts) is corrected for by the action of the feedback loop, and any higher frequency signal information is recovered from photodetector D2. This is the case of the low gain bandwidth product (LGBP) mode, shown in figure 2.6.

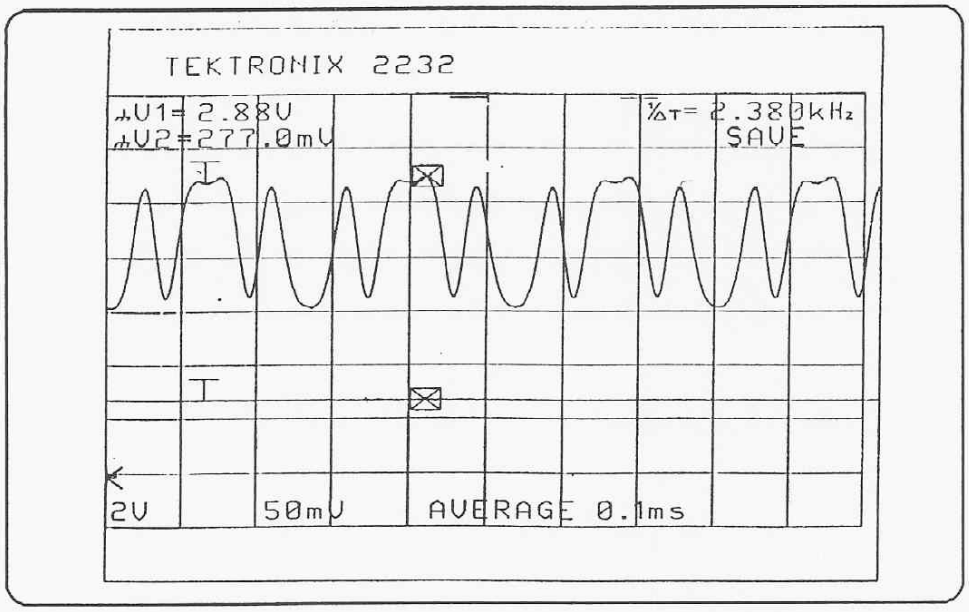

Figure 2.6 - Outputs from both photodetectors in the condition $\Delta L_{receiver} = \pm \Delta L_{sensor}$

(top - photodetector D2: Visibility = 0.29 ; I_{mean}=214 mV)

(bottom - photodetector D1: Visibility ≈ 0.00 ; I_{mean}=2.88 V)

In this particular example, only one of the two PZTs in the receiving interferometer was operational. The measurement range is always restricted by the limited phase tracking range of the piezoelectric element, which necessitates frequent resetting of the system, consequentially leading to the value of the measurand being lost. This last drawback can be offset by using "white-light" interferometry.

In order to increase the dynamic tracking range of the receiving interferometer, two piezoelectric elements working in antiphase can be used, combined with a high voltage output from the electronic servo system. To improve the dynamic tracking range, the fringe visibility and the bandwidth of the servo, it was necessary to study and characterize the different parts which compose the receiving interferometer, namely: the piezoelectric elements; the polarization controller; and the electronic servo, these are discussed in the following sections.

2.3.1 The Piezoelectric Elements

The two identical piezoelectric hollow cylinders used in the receiving interferometer, were supplied by VERNITRON Ltd. and were fabricated from a proprietary ceramic material classified as PZT-4, which is recommended for use with high voltage signals, because of their

ability to withstand high levels of electrical excitation and mechanical stress. The cylinder had an external diameter of 76 mm, wall thickness of 5 mm and length of 76 mm, their first resonant frequency for the circumferential mode of vibration was approximately 13 kHz, as given by the manufacturer [25]. Single mode fibre, with nominal external diameter of 125 μm and core index of refraction of 1.462, was tension wrapped with 101 turns on each PZT.

A theoretical model is developed to predict the efficiency and its results are then compared with the experimental measurements. In order to understand the frequency-dependent behaviour of the piezoelectric elements, different possible equivalent electrical circuits, with reasonable values for the circuit parameters, were computer simulated, and the predicted performance was compared with the experimental value. Finally, the tracking range of the low coherence system at low frequency is presented.

2.3.1.1 Efficiency Response

The phase modulation efficiency of a hollow cylindrical single mode optical fibre piezoceramic phase modulator, in the frequency range below resonance, can be estimated by making use of the theoretical model presented in [26].

The optical phase modulator, ie., the PZT wrapped with optical fibre under tension, is usually inserted in one of the arms of the interferometer, and slowly varying refractive index variations caused by temperature changes for example produce a low frequency phase difference between the two arms. The longitudinal fibre strain due to the piezoelectric ceramic deformation and the associated dynamic refractive index variations produce a dynamic phase delay ($\Delta\phi_m$). This phase delay is calculated from the variation of the optical path, and is generally a combination of two terms: the mean phase delay ($\Delta\phi_i$) and the differential phase delay ($\Delta\phi_d$), where this last term is associated with the fibre birefringence. In our case, we consider only the mean phase delay ($\Delta\phi_i$), because it is much greater than the differential one[26]. Using the same model, the phase modulation efficiency ($\eta_{\phi i}$) of the piezoelectric ceramics in the receiving interferometer, at the frequency range below resonance, can be calculated in terms of the mean phase delay by the following equation [26]:

$$\eta_{\phi i} = \frac{\Delta\phi_i}{NV} = \frac{4\pi^2 C}{\lambda_o}\left[n_c + \frac{(1+\nu)n_c^3}{2}\left[\frac{(P_{11}+P_{12})r}{2R} - P_{12}\right]\right] \qquad (20)$$

where N is the number of fibre turns wrapped on the PZT, V is the applied voltage, λ_o is the mean wavelength of the light source, n_c is the mode effective refractive index, r is the external fibre radius, R is the outer radius of the piezoelectric cylinder, ν is the Poisson's ratio, P_{11} and P_{12} are the strain optical coefficients, and C is the radial displacement of the PZT per unit of voltage. The efficiency ($\eta_{\phi i}$) is expressed in radians per unit of voltage and turns.

The parameter C depends on both the geometry and the material of the piezoelectric ceramic, and can be obtained from a graph of [26]. For our case, the PZT was from class PZT-4 and had an aspect ratio of inner to outer cylinder radius of 0.87; hence from the graph in ref. [26] a value for the parameter $C \approx 6.1*10^{-10}$ mV^{-1}, was obtained. For single mode silica fibre, we have the following values for the other constants [27]: $\nu = 0.17$, $P_{11} = 0.121$ and $P_{12} = 0.270$. Substituting all the values for the variables in equation (20), we obtained for the phase modulation efficiency the value† $\eta_{\phi i} = 59.76*10^{-3}$ rad V^{-1} $turn^{-1}$. Then, for 101 turns of single mode fibre wrapped around the PZT, we obtained the theoretical efficiency:

$$k_{pzt} = \eta_{\phi i} N = 6.04 \text{ rad } V^{-1}$$

To experimentally determine this value, we used the following procedure. A sawtooth waveform, at a frequency much less than the first resonance frequency of the PZT, was applied to the piezoelectric cylinder placed in one of the arms of the interferometer, and the drive amplitude (V_{amp}) was adjusted to modulate the interferometer output signal over one fringe, i.e., 2π radians enabling the efficiency to be determined from the following relation:

$$k_{pzt}(\text{exp}) = \frac{2\pi}{V_{amp}} \qquad (\text{rad } V^{-1}) \qquad (21)$$

Using this technique, we obtained the experimental efficiencies of both PZTs in the receiving interferometer, and for the case of both working in antiphase, below the first resonance frequency:

$$k \text{ (PZTb1)} = 5.90 \text{ rad } V^{-1}$$

$$k \text{ (PZTb2)} = 6.54 \text{ rad } V^{-1}$$

$$k \text{ (both)} = 12.08 \text{ rad } V^{-1}$$

---

† Because we used a Michelson interferometer, the relation (20) must be multiplied by a factor of two, thus giving the presented value of $59.76*10^{-3}$ rad V^{-1} $turn^{-1}$.

In figure 2.7, one example of experimental data obtained using this technique is shown.

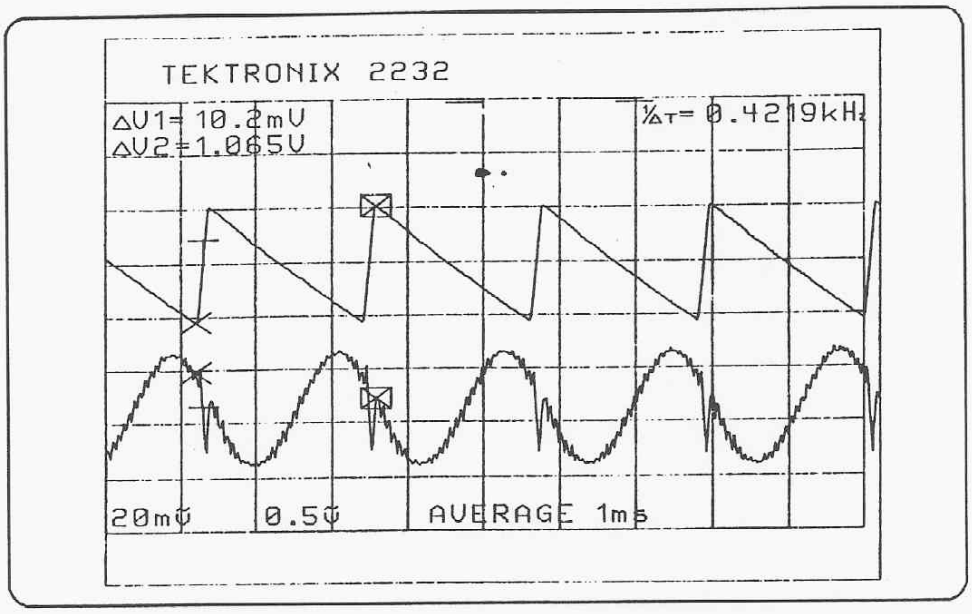

Figure 2.7 - Experimental result for the efficiency of PZTb1 in the receiving interferometer (top - the modulation signal applied to PZTb1: V_{amp}= 1.065 V,frequency = 420 Hz) (bottom - output interference signal from the interferometer modulated by 2π radian).

The difference between the theoretical and the experimental results is small (theo: 6.04 rad/V; exp:5.90 rad/V for PZTb1), showing that the theoretical model is consistent.

The discrepancy between the two experimental values for these PZTs could be due to several factors: the PZTs are not exactly the same; number of turns not being equal; the tension applied in the wrapping process was slightly different; etc.

The value for the efficiency of the PZTA (0.78 rad/V) in the sensing interferometer was measured using the technique explained here.

However, the efficiency does not remain constant as we approach the resonance frequency of the piezoelectric ceramic. Figure 2.8 shows the experimental efficiency response of the PZTs used in the receiving interferometer (the data was obtained using the same technique). As we expected (from the information provided by the manufacturer), we can see that the first resonance frequency is approximately 13 kHz.

With this last result, the transfer function which relates the applied voltage to the phase modulation is fully characterized.

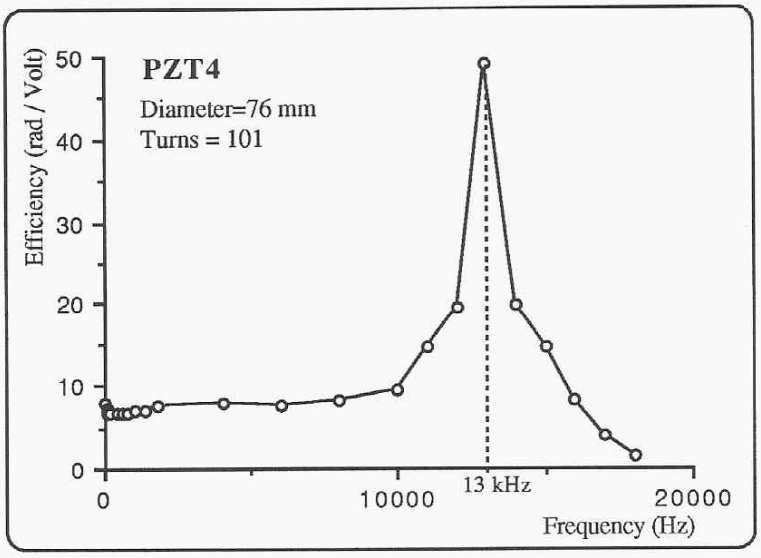

Figure 2.8 - Efficiency response of the PZT-4 type, with an external diameter of 76 mm and wrapped around with 101 turns of single mode fibre.

2.3.1.2 Impedance Response

As has been shown in [28], the properties of piezoelectric resonators with two electrodes may be studied from an equivalent electrical circuit (a two-terminal network) with related resonant frequency (w_h). The model consists of a resonant circuit with one resistor (R_h), one inductor (L_h) and one capacitor (C_h) connected in series, and a parallel low frequency capacitor (C_0), as shown in figure 2.9.

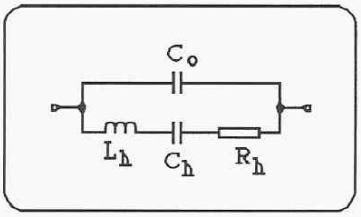

Figure 2.9 - Equivalent electrical circuit of the piezoelectric ceramic.

Considering this schematic diagram of the equivalent electrical circuit, the behaviour of the piezoelectric resonator in the vinicity of the h-th resonance frequency may be described from the complex impedance:

$$Z_h(w) = \frac{\left[R_h + jwL_h + \frac{1}{jwC_h}\right]}{jwC_o\left[R_h + jwL_h + \frac{1}{jwC_h} + \frac{1}{jwC_o}\right]} \tag{22}$$

This equivalent electrical circuit exhibits a parallel resonance frequency (w_{hp}) and a series resonance frequency (w_{hs}), which are defined as follows [28]:

$$w_{hs} = \frac{1}{\sqrt{L_h C_h}} \tag{23}$$

$$w_{hp} = \frac{1}{\sqrt{L_h \frac{C_o C_h}{C_o + C_h}}} = w_{hs}\sqrt{1 + \frac{C_h}{C_o}} \tag{24}$$

An important parameter of the equivalent electrical circuit is the mechanical quality factor (Q_m), which is defined as the ratio of the energy supplied per cycle to the energy dissipated per cycle, this can be calculated from either of the following relations [25,28]:

$$Q_m = \frac{w_{max}^2}{w_{min}\,|Z_{min}|\,C_o\,(w_{max}^2 - w_{min}^2)} = \frac{w_{hs}\,L_h}{R_h} \tag{25}$$

where $|Z_{min}|$ is the minimum impedance modulus and w_{max} and w_{min} are the frequencies of maximum and minimum impedance, respectively. These frequencies are slightly different from w_{hp} and w_{hs}; however, when the mechanical quality factor (Q_m) becomes infinitely large, these frequencies, w_{max} and w_{min}, coincide with the parallel and series resonance frequencies, respectively. The separation between the series and parallel resonance frequencies of the equivalent circuit depends on the magnitude of the piezoelectric module of the material from which the resonator is made, and can be modified by external reactances connected in series or parallel to the piezoelectric resonator [28]. The resonance frequency of piezoelectric resonators

depends, to some extent, on the magnitude of the excitation current of the resonance, and its mathematical description makes it necessary to use a non-linear impedance characteristic for the piezoelectric resonator. This study is beyond the scope of this work. A convenient method, often used to determine the values of the electric elements in the equivalent circuit of the PZT, is to measure the frequencies of minimum impedance (w_{min}) and maximum impedance (w_{max}); for piezoelectric ceramics, the error resulting from this method is very small, less than 0.1% [25]. Figure 2.10 shows the impedance response of the PZT-4; the data was obtained using an network analyser (Hewlett Packard-HP). However, this model is not very accurate in the frequency range 0 Hz to 50 kHz.

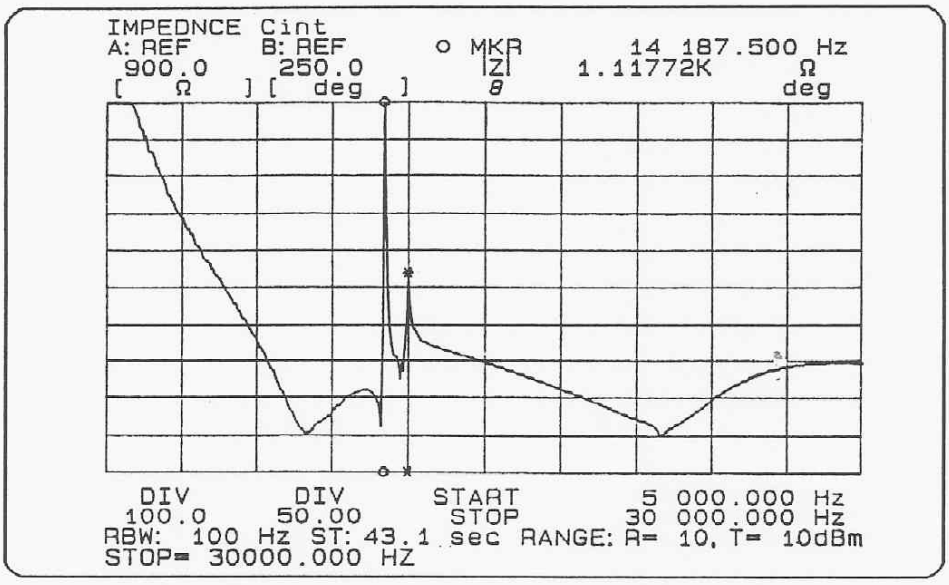

Figure 2.10 - Experimental results of the PZT impedance response (Vernitron PZT-4).

From the experimental data, the PZT exhibits a series resonance at 14.063 kHz, where its impedance is about 29.2 Ω, and a parallel resonance at 14.188 kHz, where its impedance is about 1.118 kΩ. It exhibits a second series resonance at 14.739 kHz, where its impedance is about 158 Ω, and a second parallel resonance at 15 kHz, where its impedance is about 442Ω. The other small peak before the first resonance frequency could be due to parasitic capacitances in the connection between the PZT and the network analyser probe. The low frequency capacitance (C_0) was measured to be 31.7 nF at 1 kHz.

The equivalent circuit for the PZT shown in figure 2.9, will be valid for frequencies well below the second resonance frequency of the PZT, which is, in this case, very close of the first resonance frequency. Neglecting this fact, only for the theoretical analysis, and assuming that the second resonance frequency of the PZT is much higher than the real one, the equivalent circuit assumed for the PZT (fig.2.9) is adequate as far as the analysis is concerned.

Making use of the relations (22),(23),(24),(25) and from the impedance data of the PZT, considering only the first parallel and series resonance frequencies, the circuit parameters of the PZT were approximately estimated as R_h= 28.4 Ω, L_h= 0.224 H, C_h= 0.571 nF and C_o= 31.7nF. The theoretical impedance response for these values is shown in figure 2.11.

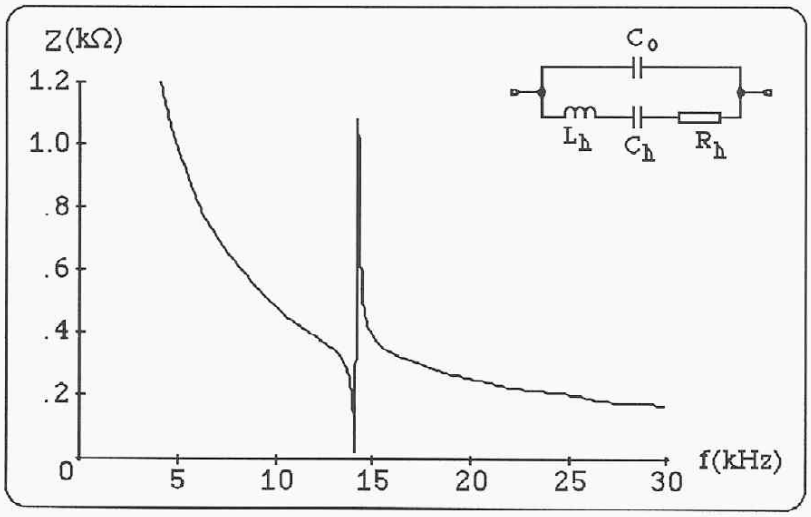

Figure 2.11 - Impedance of the circuit shown as function of frequency.

This equivalent circuit is valid, if there is no other resonance frequency close to w_h, which is, for this case, the first resonance frequency. However, from the results shown in figure 2.10, it is clear there are several resonances, hence to better model the PZT behaviour we consider other equivalent circuits based on the equivalent circuit shown in figure 2.9 [28]. Thus, using this equivalent circuit for each resonance frequency (w_h), with different series or parallel resonances associated with them, and applying the same mathematical relations on each resonance frequency, we can estimate all the parameters of the circuits, for the possible equivalent circuits shown in figures 2.12 and 2.13.

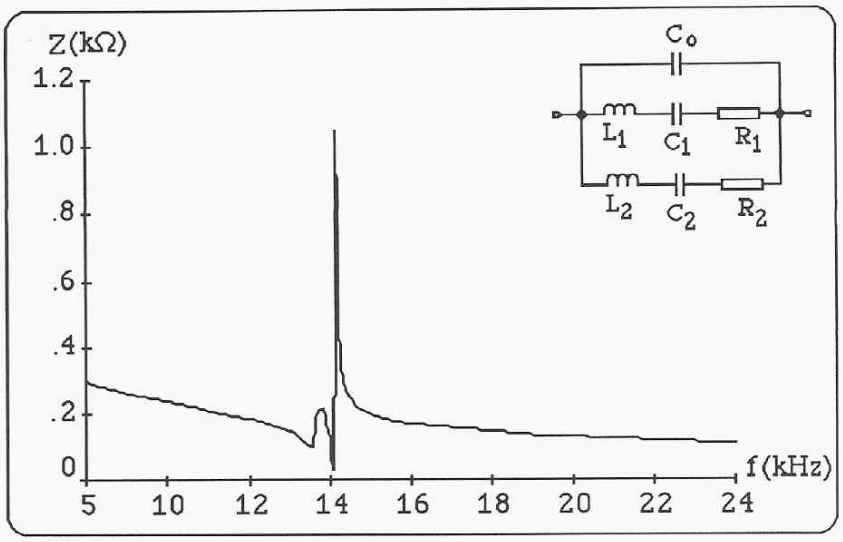

Figure 2.11 - Impedance of the circuit shown as function of frequency

(C_o= 31.7 nF, L_1 = 0.224 H, C_1 = 0.571 nF, R_1 = 28.4 Ω)

(L_2 = 0.103 H, C_2 = 1.133 nF, R_2 = 152.9 Ω).

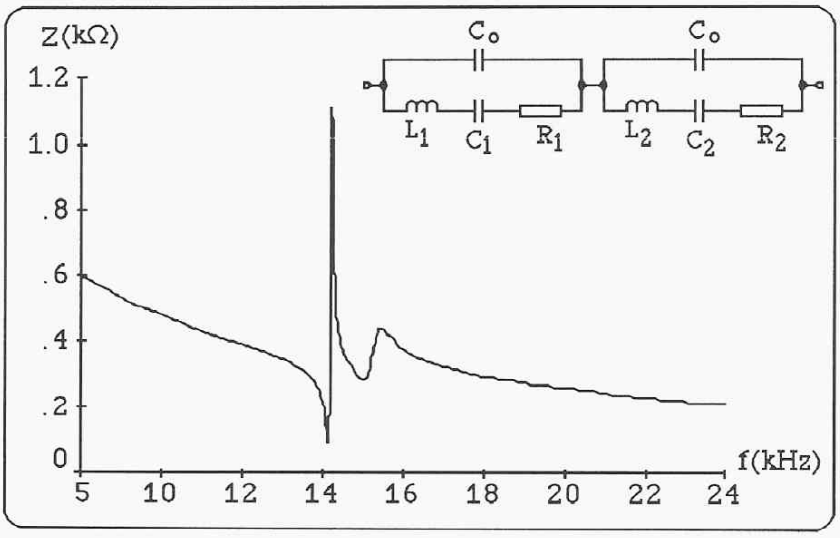

Figure 2.12 - Impedance of the circuit shown as function of frequency

(C_o= 63.4 nF, L_1 = 0.113 H, C_1 = 1.13 nF, R_1 = 28.6 Ω)

(L_2 = 0.051 H, C_2 = 2.20 nF, R_2 = 153 Ω).

As can be seen, the form of these two computer simulated curves is similar to the experimental data; however, they do not match exactly. This mismatch could be due to approximations in the theoretical models used. If we take into account the stray capacitances and the mismatch

impedances between the probes and the PZT contacts in the equivalent circuit, it will probably be possible to get a better approximation to the experimental data obtained, as shown in [29]. The implications of this complex behaviour are very important when the objective is to develop a feedback loop system, for phase control, using these modulators, because of the stability and bandwidth of the loop.

The observed behaviour implies that the bandwidth of the servo system must be restricted to prevent it from oscillating. This problem will be discussed in more detail in section 2.3.3, where the servo system used in this interferometric reading scheme is presented.

2.3.1.3 Tracking Range

As one of the applications envisaged for this interferometric system is monitoring the complex vibrations of a gearbox, operating at high temperature, it was necessary for the servo system to have a large dynamic tracking range, in order to keep the receiving interferometer coherently tuned to the sensing interferometer, ie, the sensor. For example, for an all-fibre Michelson interferometer working as a vibration sensor, with a path-length imbalance of $\approx$ 40 mm, a temperature variation of 250 K causes the static path-length imbalance to change by $\approx$ 62 μm.

The receiving interferometer was designed with two PZTs working in anti-phase with $\approx$26 meters of monomode fibre wrapped around each of them, in order to produce a large scan, by shortening one path and increasing the other. The receiving system could track induced optical path changes in the sensor simulator up to $\pm$ 550 μm (= 1.1 mm) at very low frequencies, as shown in figure 2.14. The tracking range of the whole system is limited by the allowable tracking range of the active device (ie, the PZT) controlling the optimum path-length of the of receiving interferometer.

Difficulties were experienced with the system when attempting to track such large displacements at frequencies above 500 Hz. The main reason for this was the relatively low resonance frequency of the PZTs (about 13 kHz), and the difficulty in generating very large currents required to drive the PZTs at high frequency.

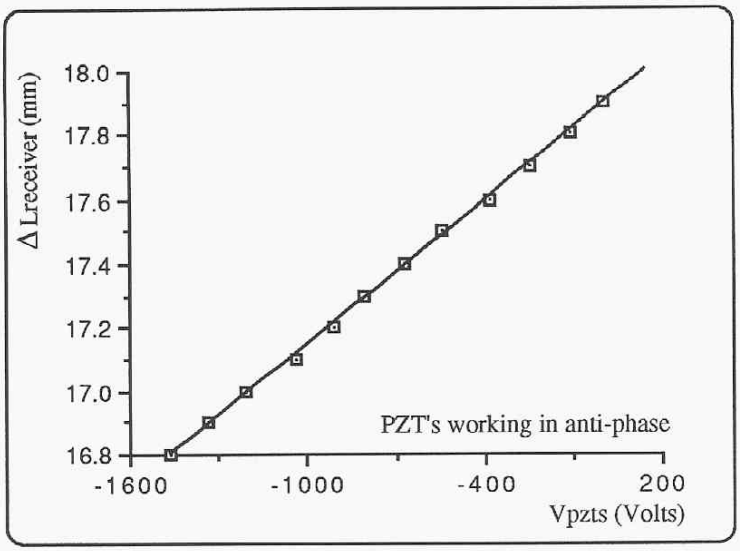

Figure 2.14 - Dynamic tracking range of the receiving interferometer.

2.3.2 The Polarization Controller

To maximise the fringe visibility of the interference signal, a polarization controller made of fractional-wave elements [30,31,32], can be used to ensure that the two beams, in the fibre Michelson interferometer, recombine at the detector (D2) with their polarization vectors parallel. Otherwise, the resulting interference will not be optimized.

Some other solutions have already been proposed for adjusting the polarization : stress with electromagnets [33], twist [34] and use of polarization maintaining fibres [32,35]. However, the use of fractional-wave elements seems to be the easiest and cheapest solution.

The polarization controller was designed using the formula presented by Lefevre [30], and a particular combination of fractional-wave plates which obey the retardation conditions (the octahedron transformation space) [31].

First, a theoretical prediction of the behaviour of the fractional-wave plates using the Poincaré sphere representation is presented. Then an experimental study of the performance of this fractional-wave plates based in the same graphical representation is shown.

2.3.2.1 Fractional-Wave Plates and the Poincaré Sphere

Fractional-wave devices, including waveplates and fibre loops, provide a type of transducer useful for state of polarization (SOP) transformations. These elements have a fixed retardation angle (ϕ), and vary the axis of retardation. It can be shown [31] that the best configuration for transforming between any static SOP's consists of three plates of quarter-wave retardation. However, many combinations other than this one can be used. For example, two quarter-wave plates alone are known to match two arbitrary static SOP's [31].

An equivalent all-fibre device is shown in figure 2.15; it comprises three disks wound with loops of conventional monomode fibre. Optically, each disk behaves as a fractional-wave plate, with retardation angle determined by the diameter of the disk and the number of loops of fibre. The retardation angles (ϕ) are fixed, but the plates may be rotated about the direction of propagation of the light at particular angles (α), in order to achieve the desired SOP matching.

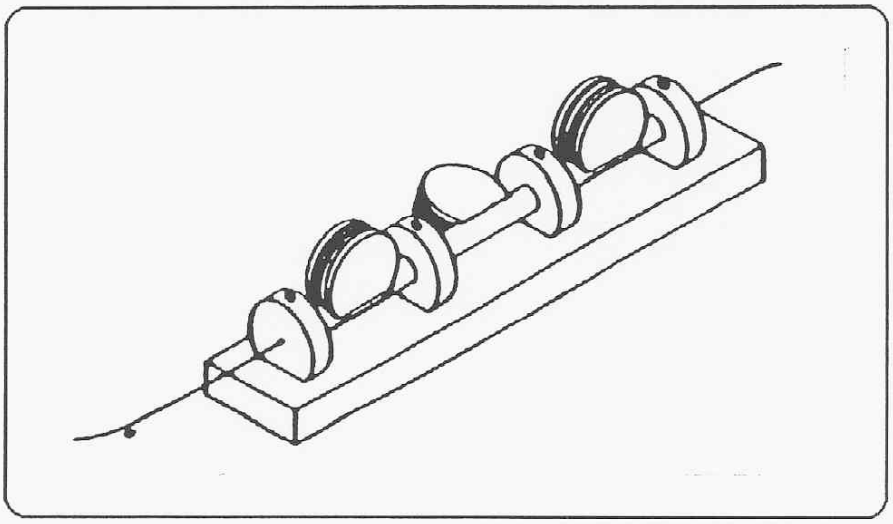

Figure 2.15 - Polarization controller with three fractional-wave plates.

For the design of this type of polarization controller it is necessary to know which radius (R) of the disk with a number (N) of turns of monomode fibre should be chosen, to get a λ_o/m fractional-wave plate (where m=2,4 or 8).The relation can be expressed as follows [30,31]:

$$R\ (m,N) = \frac{0.836\ r^2\ N\ m}{\lambda_o} \qquad (26)$$

where "r" is the nominal radius of the fibre (typically, r = 62.5μm), N is the number of turns, λ_o is the wavelength of the light and m=2,4 or 8.

The analysis made by Lefevre [30] does not include the compliance and thickness of the fibre jacket and, if needed, a small correction must be made [32] in the formula (26).

A mechanical schematic design of one section of the fractional-wave polarization controller used in our experiements is shown in the appendices (appendix A).

A convenient way to represent states of polarization is the Poincaré sphere [33,36] (the method is applicable only if the incident beam is completely polarized).The SOP of any polarized light, ie., an arbitrary elliptical polarization, can be represented by a point on the sphere (for example: point C), shown in figure 2.16. The tilt angle of the elliptical polarized light is represented by ψ, and 2ψ is the coordinate on the Poincaré sphere indicating the angle from the x-z plane. The degree of ellipticity is represented by χ , which is the modulus of the inverse tangent of the ratio of the minor to major axis of the elipse. On the Poincaré sphere, 2χ is the angle from the x-y plane. Concerning the polarity of χ, it is usually defined so that $\chi > 0$ for right-handed rotating polarization, and $\chi < 0$ for left-handed rotating polarization.

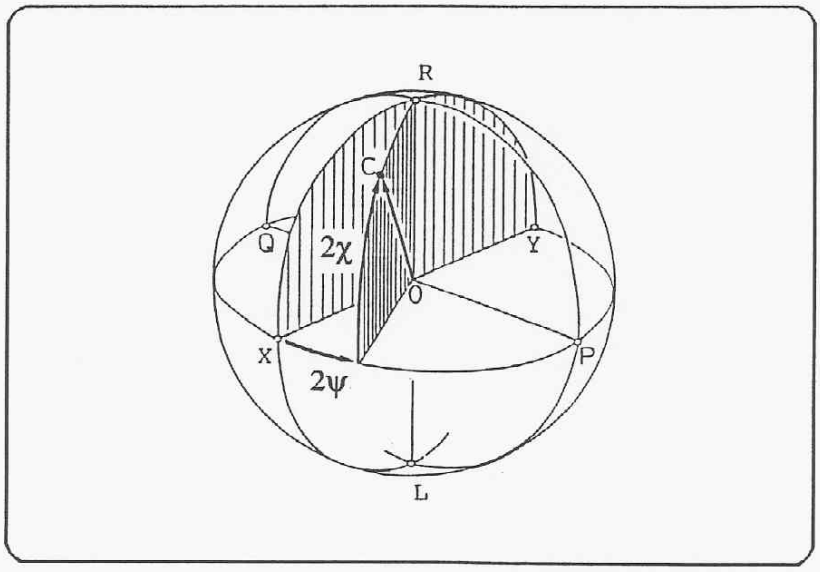

Figure 2.16 - The Poincaré Sphere.

There are some particularly important points on the sphere, such as: (R and L) for the right- and left-handed circular polarized light ($2\chi = \pm 90°$) which correspond to the north and south poles, respectively; and (X,Y,P,Q) for all linearly polarized states ($\chi = 0°$, therefore they are

all represented along the equator). Any two orthogonal polarization states are diametrically opposite on the sphere. Birefringence is seen as a rotation of the sphere around an axis corresponding to the diameter through the two principal SOP´s. Therefore, circular birefringence represents rotation around the axis through L and R on the sphere. Using the Poincaré representation, it is possible to predict the effect of a retarder on a beam of polarized light, with a certain polarization state, say C (figure 2.16), by a rotation of the sphere about the appropriate axis and through the appropriate angle [36].Then, the new location of point C (relative to the original sphere) characterizes the polarization of the emerging beam.

The Poincaré sphere has a drawback in that it can not obviously be drawn or printed on a flat surface. So, a convenient way to represent the effects of fractional-wave plates, which work as retarders with retardances of λ_0/m (m=2,4 or 8) was presented by Koehler et al. [32].

It consists of a top view of the Poincaré sphere, where 2χ is incremented linearly in the projection, ie., the figure it is not a perspective view of the sphere. Twice the ellipticity (2χ) is plotted radially inward and the coordinate (the azimuth), 2ψ, is given by the angle around the perimeter of the equator, as shown in figure 2.17.

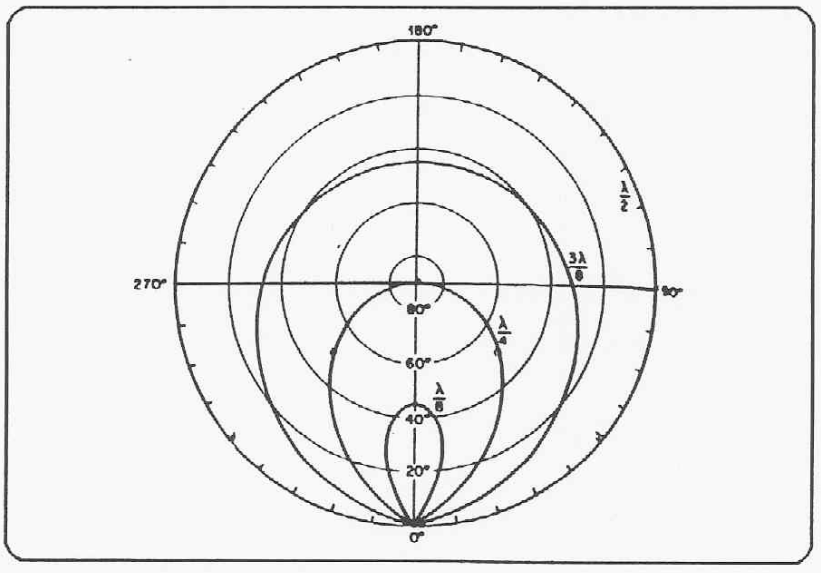

Figure 2.17 - Non-perspective top view of the Poincaré sphere showing the effect of $\lambda_0/2$, $\lambda_0/4$, $3\lambda_0/8$ and $\lambda_0/8$ plates on a linear horizontal input polarization [32].

For 180° rotation (α angle) of the wave plates, the locus shows a double loop, one in the upper hemisphere and one in the lower hemisphere. So, rotating a perfect quarter-wave plate (ie, $\lambda_0/4$

or $\phi = \pi/2$) gives output polarizations which follow the indicated curves (in one of the hemispheres - for the first 90° rotation - and then following the same path on the other hemisphere). In the projection of figure 2.17, the two curves are coincident. A half-wave plate (ie, $\lambda_o/2$ or $\phi = \pi$) introduces 180° phase difference between the principal axes, therefore maps linear polarizations to linear polarizations, where the ellipticity remains zero, (the $\lambda_o/2$ curve in figure 2.17 follows the equator). This graph, however, does not show how ψ varies with the angle of the plate (α). We can plot a graph of ψ versus α , or label the parameter α at each data point on fig. (2.17). In these polarization controllers, the fractional-wave plates usually do not behave as predicted by the theory, because there are other effects which introduce birefringence, such as: shear stress (by turning the fibre) and also twist. Twisting introduces circular birefringence, which rotates the Poincaré sphere around the LR axis, and the stress also mixes into the coil of fibre, yielding elliptical birefringence from the combination of circular and linear birefringence, which results in a complicated effect [34]. Using this representation of the Poincaré sphere we can characterize the fractional-wave plates, which will be used in the polarization controller of the receiving interferometer.

2.3.2.2 Experimental Performance

A convenient method for pratical determination of the polarization ellipse is to measure the Stokes parameters [36]. These can be measured with the aid of a linear polarizer (P, figure 2.18) and a $\pi/2$ retarder ($\lambda/4$ plate, see figure 2.18), the latter being a device for imposing 90° phase retardation on one linear optical polarization component, compared with its orthogonal component. If $I(\theta,\varepsilon)$ (figure 2.18) denotes the intensity of the light passed by the linear polarizer at angle θ to O_x, after the O_y component has been retarded by angle ε (in the presented case, $\varepsilon = \pi/2$) as the result of inserting the retardation element, then the Stokes parameters are defined as follows[36]:

$$S_o = I(0°,0) + I(90°,0) \qquad S_1 = I(0°,0) - I(90°,0) \tag{27}$$
$$S_2 = I(45°,0) - I(135°,0) \qquad S_3 = I(45°,\pi/2) - I(135°,\pi/2)$$

Only three of these parameters are independent, since:

$$S_o^2 = S_1^2 + S_2^2 + S_3^2 \tag{28}$$

The measurement of the S_n parameters provides the ellipticity and the orientation of the polarization ellipse via the relations [36]:

$$\chi = \frac{1}{2}\left|\sin^{-1}\left(\frac{S_3}{S_o}\right)\right| \tag{29}$$

$$\psi = \frac{1}{2}\left|\tan^{-1}\left(\frac{S_2}{S_1}\right)\right| \tag{30}$$

The Stokes parameters S_1, S_2 and S_3 may be regarded as the cartesian coordinates of a point in the sphere referred to axes OX, OP and OR all points lying on a sphere of radius S_o, ie., the Poincaré sphere (figure 2.16).

Figure 2.18, shows the experimental arrangement used to study the performance of the $\lambda_o/2$ and $\lambda_o/4$ wave plates (the λ/m coil in the figure 2.18), by measuring the Stokes parameters. Then, by a graphical representation of the polarization states using a non-perspective top view of the Poincaré sphere, as presented in the previous section.

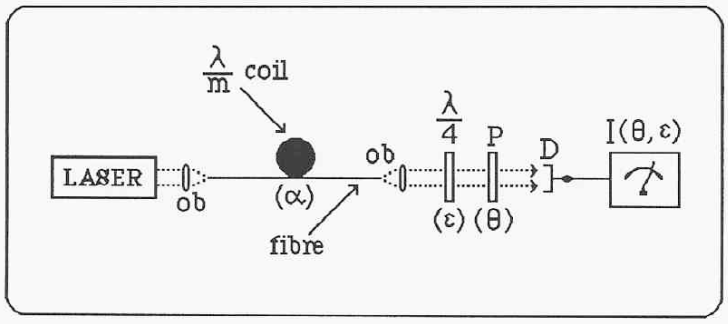

Figure 2.18 - Experimental arrangement for the measurement of the Stokes parameters, for different fractional-wave plates.
(P: Polarizer, D: Photodetector, ob: Microscope Objective)

Varying the angle (α) of the fractional-wave plate, by rotation around the direction of propagation of the light in the fibre, we measured the Stokes parameters for different positions of the fractional-wave plate. On the Poincaré sphere, the plate produces a rotation through an angle equal to the angle of retardation of the plate (ϕ), about an axis lying in the equatorial plane at an angle (α) to the direction (X,Y) [36]. The axes rotate in the equatorial plane of the Poincaré sphere as the fractional-wave plates are rotated in space. If a train of three retarders is

used, three rotations must be performed in succession, and the rotations are described by three arcs on the sphere, each one connected to the next [36]. Figures 2.19-a and -b, show the experimental behaviour, for radiation with $\lambda_0 = 781$ nm, of single $\lambda_0/2$ and $\lambda_0/4$ wave plates with one turn of monomode fibre, respectively, and for linear horizontal input polarization.

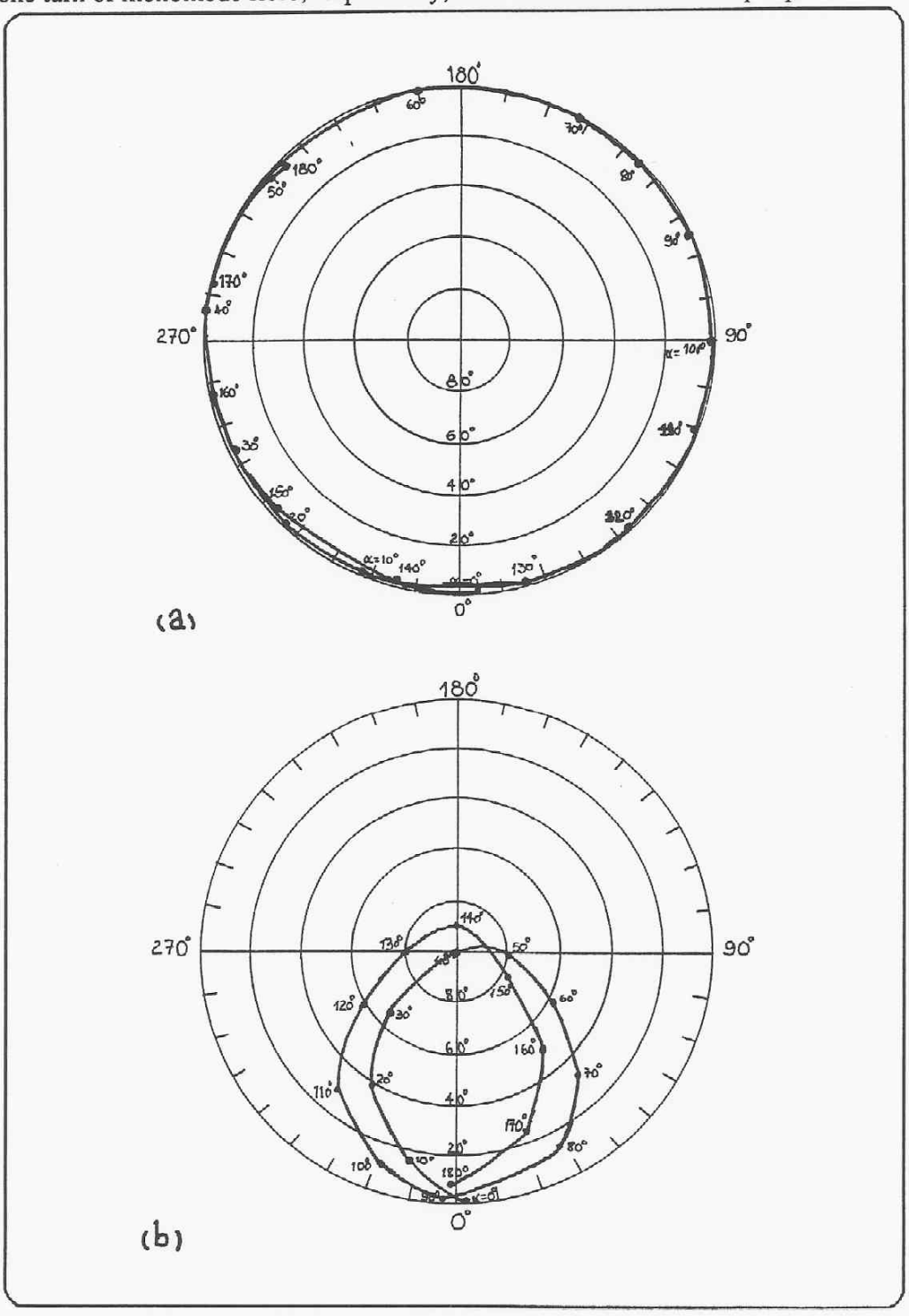

Figure 2.19 - Non-perspective top views of the Poincaré sphere. Data points were taken every α=10° rotation of the plate (2.19-a - $\lambda_0/2$ wave plate, 2.19-b - $\lambda_0/4$ wave plate).

These figures show both ψ and χ for the same fractional-wave plate. Here, the 2-D variation of the polarization state is recorded, as a function of the angle (α), where this parameter is labelled at each data point. A comparison with the theoretical curves, shown in figure 2.17, shows the good agreement for the $\lambda/2$ plate; however, for the $\lambda/4$ plate the agreement is not as good as that for the halfwave plate. The curve has two loops, presumably one in each hemisphere, and ideally, both should pass through the pole.

This mismatch could be due to several reasons; for example, the input polarization on the coil being not exactly linear, or the existence of twist and shear stress introduced when turning the coil. In figure 2.20, it is shown the behaviour of one halfwave plate ($\lambda/2$ plate) when the fiber is twisted around the coil is shown. As can be seen, this effect is very complicated, introducing strange effects on the fractional-wave plate work. This experimental result agrees with the work by Ulrich and Simon [34].

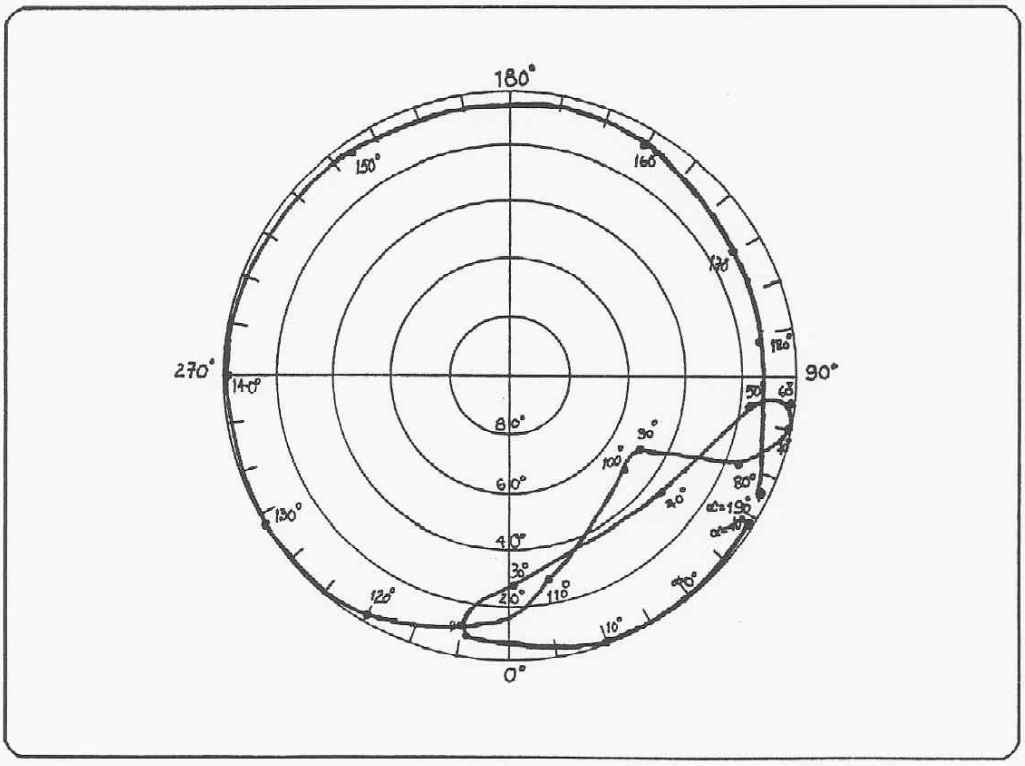

Figure 2.20 - Non-perspective top view of the Poincaré sphere for a $\lambda_0/2$ wave plate, with the fibre being twisted around the coil; data points were taken at every α=10° rotation of the plate.

The twist effect on the fibre can be graphically described on the surface of the Poincaré sphere by cycloidical curves [34]. Plotting, in a linear scale, 2χ as a function of 2ψ for the data of figure 2.20, and comparing with the experimental results of Ulrich and Simon [34], we can observe approximately the same behaviour (figure 2.21). However, our twist effect was not experimentally controlled as in their experiments.

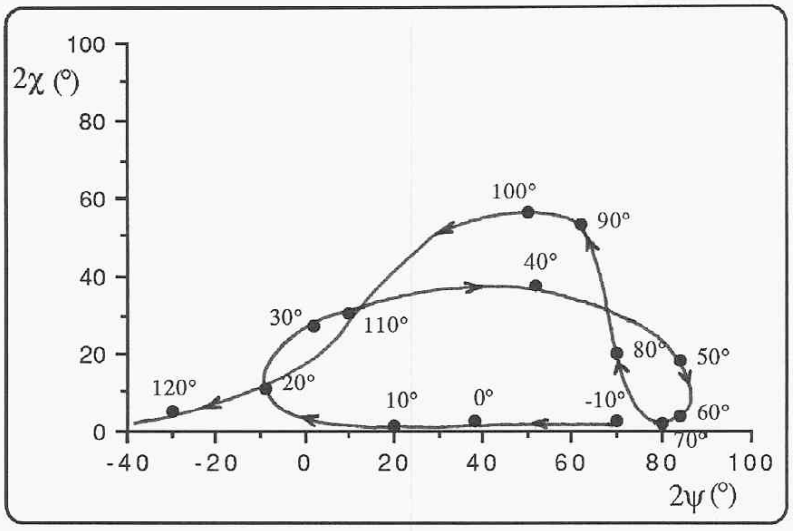

Figure 2.21 - Ellipticity vs. azimuth for a $\lambda/2$ wave plate with one turn of single mode fibre, illuminated by a source with λ=781 nm, the fiber being twisted around the coil. Data points were taken at every α=10° rotation of the plate.

2.3.3 The Servo System

It was shown, by D.Jackson et al.[37], how low frequency drifts in a single mode optical fibre interferometer may be eliminated by using a piezoelectric ceramic in the reference arm of the interferometer, with an electronic servo circuit. This allows the sensitivity to be maintained at the maximum, by always keeping the system in quadrature in the presence of drifts. This system had a bandwidth of approximately 200 Hz, and as the information carrying signals were above this frequency they were not affected by the action of the feedback loop.

The system developed here is designed to demodulate signals of large dynamic range in the presence of disturbances (such as thermal drift and low frequency acoustical noise), with frequencies between 100 Hz and 1.3 kHz.

Several feedback loop circuits were tried, but due to the small resonance frequency of the PZT´s (about 13 kHz) the loop was unstable ans tended to oscillate, as we will seen in the following sections. Clearly, the observed behaviour implies that the bandwidth of the servo must be restricted to prevent it from oscillating. The developed electronic system was found to be stable with a bandwidth up to ≈1.3 kHz. A phase resolution pf better than 1 mrad/√Hz at frequencies below 600 Hz was obtained, with dynamic range of ≈ 90 dB.

2.3.3.1 The Feedback Loop

A block diagram of the circuit is presented in figure 2.22. To emphasize the features important for the feedback analysis, the complete schematic diagram of the servo circuit is shown in appendix B. With the assumption of large loop gain, the system is held in quadrature and linearized equations may be used [38].

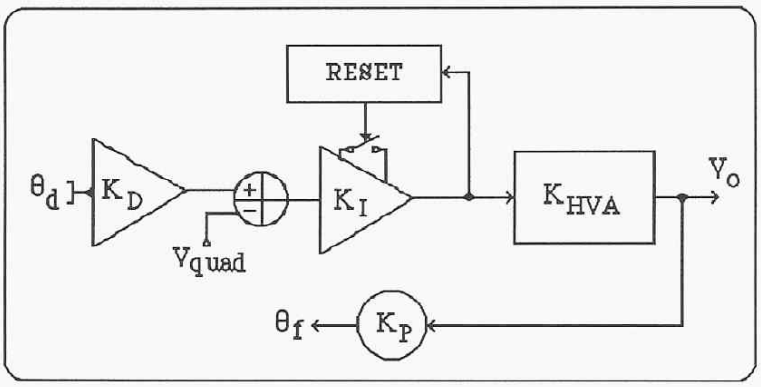

Figure 2.22 - Block diagram of the feedback stabilization loop.

From figure 2.22, one may write:

$$V_o(s) = \theta_d(s)\, A(s) = [\, \theta_i(s) - \theta_f(s) \,]\, A(s) \qquad (31)$$

where $V_o(s)$ is the Laplace transform† of the output voltage, $\theta_i(s)$ is the Laplace transform of the phase of the light wave in the signal arm, $\theta_f(s)$ is the corresponding transform for the wave in the reference arm, V_{quad} is the voltage used to set the quadrature point, and A(s) is the forward gain of the loop. The quantities A(s) and $\theta_f(s)$ may be expressed as:

---

† Given a function f(t), defined for every t≥0, we form the integral: $F(s) = \int_0^{+\infty} f(t)\, e^{-st}\, dt$. For values $s=\alpha+j\omega$, of the complex variable s, for which it converges, it defines a function F(s), known as the Laplace Transform [7].

$$A(s) = K_D K_I(s) K_{HVA} \tag{32}$$

$$\theta_f(s) = B(s)V_o(s) = K_P V_o(s) \tag{33}$$

where B(s) is the feedback gain; K_D represents the conversion gain of the photodetector, which depends on the visibility of the interference pattern and has dimensions of volts per radian. K_P is the conversion gain of the PZT cylinder (it is constant only for the frequency range below resonance), around which is wrapped the fibre of the reference arm, and has dimensions of radian per volt. $K_I(s)$ represents the transfer function of the integrator circuit with reset switch, and K_{HVA} is the conversion gain of the linear high voltage amplifier (HVA). Combining the equations (31),(32) and (33), we obtain the closed-loop transfer function:

$$H(s) = \frac{V_o(s)}{\theta_I(s)} = \frac{A(s)}{1 + A(s)B(s)} \tag{34}$$

where A(s)B(s) is the open-loop gain. The quantity $K_I(s)$ is expressed as follows [38]:

$$K_I(s) = \frac{1}{sRC} \tag{35}$$

where R and C are the values of the resistor and the capacitor of the integrator, respectively. Using relation (35) in equation (34), the closed-loop transfer function will be of the first-order loop type:

$$H(s) = \frac{\frac{K_D K_{HVA}}{RC}}{s + \frac{K_D K_{HVA} K_P}{RC}} = \frac{K}{s + KK_P} \tag{36}$$

where the natural frequency of the first-order loop is given by:

$$f_n = \frac{KK_P}{2\pi} \tag{37}$$

The loop gain (KK_P) is the only parameter available in the design of the circuit for the necessary adjustment. If it is necessary to have large loop gain (often needed to ensure good tracking), the bandwidth must also be large, and this must be choosen taking into account the low frequency resonance of the PZT´s used. Therefore, large bandwidth and good tracking are incompatible in the first-order loop. Other feedback loops were tried [39,40,41] using a second-order loop, where there are two circuit parameters available, whereas, usually, three loop parameter specifications must be met, and they cannot be chosen independently [38]. If it

is necessary to have large gain and small bandwidth, the loop wiil be badly underdamped and the transient response will be poor. Using a lag-lead filter, which has two independent time constants, the natural frequency and damping can be chosen independently. Furthermore, the loop gain can be made as large as necessary for good tracking.

We tried this approach; however, it was impossible to lock the servo at the quadrature point of the interference signal, for large amplitude signals, even at low frequencies. This could be due to the low resonance of the PZT´s. If we use the equivalent electrical circuit for the PZT [42], as shown in figure 2.23, then, from the previous feedback equations (the first-order loop), we will get a fourth-order loop transfer function, because the transfer function of the PZT, $B(s) = C(s)K_P$ is now given by :

$$C(s) = \frac{1}{s^3RC_oC_hL_h+s^2(RC_hC_oR_h+C_hL_h)+s(RC_h+RC_o+R_hC_h)+1} \qquad (38)$$

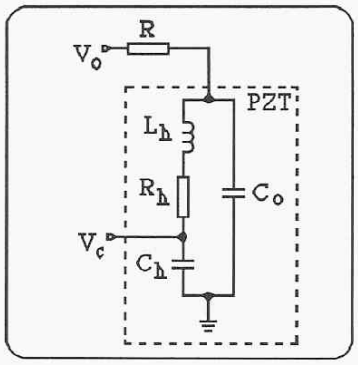

Figure 2.23 - Electrical equivalent circuit for the piezoelectric element [42].

where R is the output resistance of the last amplification stage of the servo, V_c is the voltage across the PZT capacitor C_h, which causes an optical phase change (θ_f) in the reference arm of the interferometer (the phase change can be assumed to be proportional (K_P) to V_c for frequencies below resonance), and V_o is the output voltage of the amplifier.

The closed-loop parameters of high-order loops, as the fourth-order loop, tend to be overly sensitive to changes of gain and circuit components, and it is more difficult to stabilize than the first- or second-order loops. To increase the open-loop control bandwidth, it is tempting to use a notch filter to suppress the gain around the resonance frequency of the PZT, but this selection

will add extra poles, thereby giving a poor phase response, which may induce oscillation of the closed-loop system.

A better solution can be achieved by reducing the gain around the resonance frequency with a low-pass filter or by choosing the cutoff frequency several decades below the series resonance frequency of the PZT [41]. The stability criterion of the feedback loop implies that it can oscillate if its open-loop gain exceeds unity, and simultaneously its open-loop phase shift exceeds 180 degrees. This means that, at least, one of the closed-loop poles of the loop will lie in the right half of the s-plane.

This stability analysis can be done by the root-locus method or by means of Bode plots, where a pair of graphs of the magnitude and phase of the frequency response of the open-loop gain, (A(s)B(s)), are both plotted on logarithmic scales. The Bode criterion for unconditional stability is that the gain must fall below unity (0 dB) before the phase shift reaches 180 degrees. The first-order loop has the simplest root-locus, which is a single pole at the origin, a single zero at infinity, and the closed-loop pole moves along the negative real axis from zero to infinity as the gain increases. For higher order loops, the root-locus representation becomes more complicated. For example, for a third-order loop, one feature of the plot is very striking [38]: the locus enters the right half-plane for low values of gain, and the loop will be unstable for that condition. This is in direct contrast to the first- and second-order loops which are unconditionally stable for all values of gain. Therefore, in a third-order loop, the gain must be prevented from falling into this unstable region .

In our experiments we decided to implement the first-order loop because the stabilization was better and the bandwidth achievable was the highest (1.3 kHz); however, for different values of the RC parameters of the integrator circuit, we observed a second-order behaviour, as will be shown in the next sections. This was the reason why the feedback analysis presented here was made only for the first-order loop (future work should take into account the equivalent circuit of the PZT on the theoretical analysis, which will give high-order loops and, obviously, the stabilization criterion for the loop will be more difficult to achieve, which implies that different designs of the electronic circuit should be tried). Alternatively we can use only one integrator (first-order loop), and select a PZT´s with high resonance frequency in order to approximate the transfer function of the loop by the first- or the second order type.

The linearity of the servo system, the response of the feedback stabilization circuit for different waveforms and the minimum optical phase resolution (ie, the sensitivity) will be presented in the following sections.

2.3.3.2 Characterization

The electronic servo system (appendix B) used in the experiment was operating in mode A, which is the first-order loop (ie, only one integrator stage), with a 0 to 300 volt swing in the compensation output signal. The detection block used the photodiode BPX65 (from RS Components)and had several cascaded amplification stages (see appendix C1), with an overall gain of 3.9×10^5 volt/watt. The -3 dB bandwidth was ≈1.2 MHz and a noise floor of 5.73 $\mu V/\sqrt{Hz}$ was measured The conversion gain of the PZTs at the receiving interferometer was K_P=12.08 rad/V (both PZT´s working in anti-phase), measured using the technique described in section 2.3.1.1. The conversion gain of the photodetector (K_D) was measured by driving the PZT cylinder with a small amplitude signal (ie, < 0.28 radian†), and observing the output from the photodetector (the feedback loop was not in operation). Because of the presence of the drift, the signal varies from zero to the maximum value as the phase difference reaches the quadrature condition. The maximum signal was used in the calculations.

K_D, was obtained by dividing the observed voltage gain by the conversion gain of the PZT, and was found to be 0.025 V/rad. The gain of the linear High Voltage Amplifier (HVA) was found to be 13.

In the loop analysis K_P and K_D were treated as constants, since their frequency-dependent behaviour starts well above the 5 kHz bandwidth, which is sufficient for our needs.

Different values of the integration constant (R_1C) were used in order to have the best feedback loop, which is a loop with sufficient bandwidth and with a large dynamic range for the tracking of large amplitude AC signals. The laser current for the ML4406 was set to be 70.5 mA, giving a fringe visibility of 0.31 at the output of the receiving interferometer. Modulating PZTA in the sensing interferometer with a small amplitude sine-wave, and considering different values of the integrator time constant (R_1C), the frequency response of the feedback loop for mode A of

---

† For a small signal (ϕ_s), the first-order Bessel function $J_1(\phi_s)$ is approximately $\phi_s/2$. Calculating the relative error of this approximation and assuming that the error should be less than 1%, the signal to be applied (ϕ_s) must be smaller than 0.28 radian.

operation was measured at the output of the photodetector. As we have seen, the frequency response for particular values of R_1C has the behaviour of a second-order loop with small damping ratio [38], and for other cases it will exhibit a first-order loop behaviour.

Because the resonance frequency of the PZT´s in the receiving interferometer was very small (≈13 kHz), the feedback loop sometimes tended to oscillate easily, as we can see in figure 2.24. This strange behaviour could be due to the other higher-order harmonics of the applied signal falling into the non-linear region of PZT, and hence being amplified by its conversion gain, which is very high (≈50 rad/V for each PZT) in that region (as shown in fig.2.8).

In figure 2.24, the point A is the applied signal with the system locked in the quadrature point and the point B is the oscillation due to the PZT4 at 15 kHz (the signal was obtained at the output of the photodetector and just only one PZT was working in the receiving interferometer).

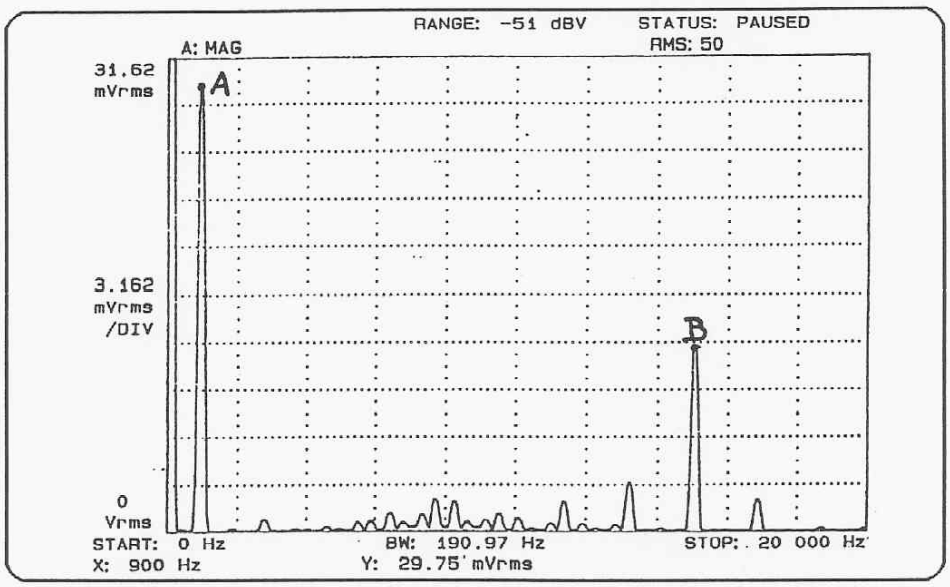

Figure 2.24 - Oscillation of the feedback loop when the system is locked at a quadrature point (R_1= 56 kΩ, C=0.86 nF).

Due to this last result, different values of R_1C were tried and the bandwidth of the servo was reduced until a better stability was achieved. The following experimental results show the second- and first-order frequency response behaviour of the feedback loop, for different values of "R_1C" (due to technical problems in the environmental isolation of the receiving interferometer, to achieve a reduction of the low frequency acoustic vibrations effects, only one

PZT was physically connected to the circuit when the data was taken). These values were taken at the ouput of the system. Figure 2.25 shows a second-order behaviour for R_1=1.2 MΩ and C=0.86 nF; figure 2.26, shows, for different values of "RC_1", an approximation to the first-order behaviour (Data taken using only one integrator).

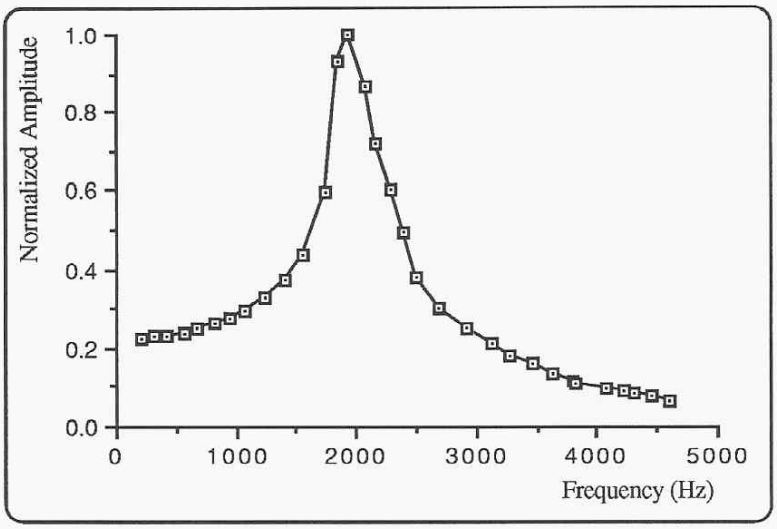

Figure 2.25 - Frequency response of the feedback loop for R_1=1.2 MΩ and C=0.86 nF.

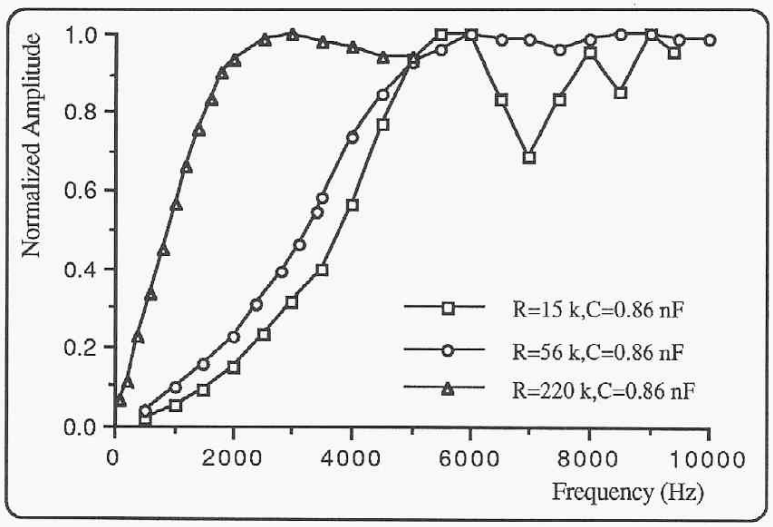

Figure 2.26 - Frequency response of the feedback loop showing an approximation for a first-order behaviour.

The best configuration was found to occur for R_1=220 kΩ and C=0.86 nF, giving a bandwidth of 1.3 kHz even for high amplitude test signals. The theoretical curve was calculated from the Fourier transform of the feedback voltage (V_{PZT}),which is given by the differential equation (first-order loop) [13]:

$$\frac{dV_{PZT}}{dt} = \pm KK_P V_{PZT} \tag{39}$$

Thus, applying the Fourier transform, $F\{V_{PZT}(t)\}$, we obtained:

$$F(\omega) = \frac{\omega}{\sqrt{\omega^2 + (KK_P)^2}} \tag{40}$$

where $\omega=2\pi f$ and f is the frequency. Then taking the values for the following quantities: K_D=0.025 V/rad; K_{HVA}=13 V/V; K_P=5.61 rad/V; R_1=220 kΩ; C=0.86 nF and substituting into equation (40), we obtain the frequency dependence shown in figure 2.27, for several frequencies.

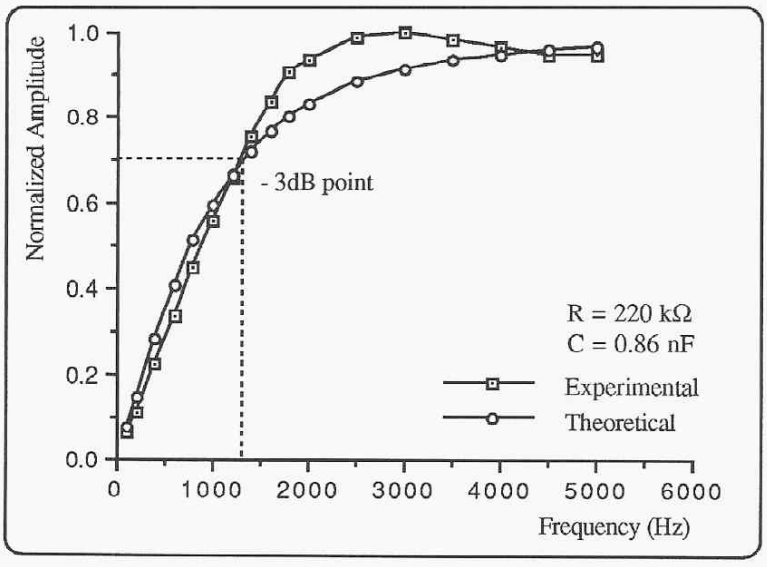

Figure 2.27 - Frequency response of the feedback loop for the first-order behaviour (data taken from the output of the detector).

As we can see from this figure, the prediction is reasonable and the natural frequency, which coincides with the frequency at the -3 dB point, is approximately equal to the theoretical one (this can be calculated from equation (37)).

By measuring the output voltage of the servo (V_{PZT}) as a function of the amplitude voltage of the applied signal (for a small applied signal with a frequency of 240 Hz, with the system in quadrature and maintaining the same experimental conditions), the linearity of the servo system was determined, giving good results, as figure 2.28 shows.

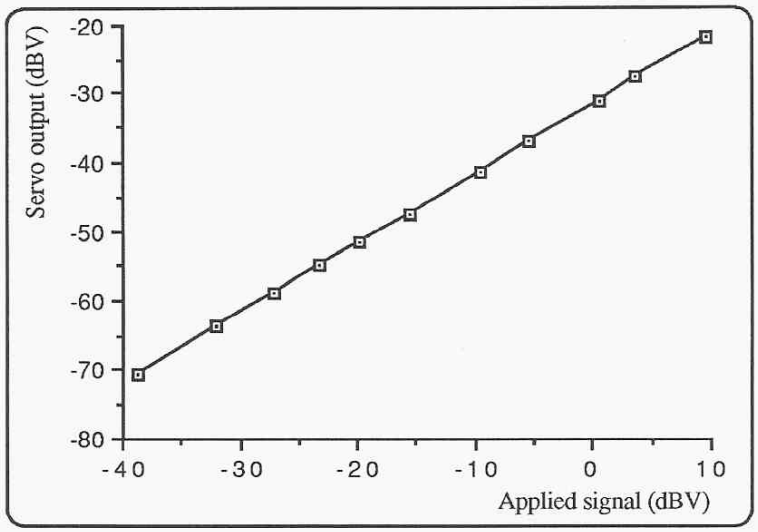

Figure 2.28 - Linearity of the servo system (quadrature point).

Figures 2.29 and 2.30 show the response of the system (operating at quadrature) for AC signals, when the PZTA in the sensing interferometer was driven with sinusoidal (fig.2.29) and square wave signals (fig.2.30). The system was found to be stable with a bandwidth up to 1.3 kHz.

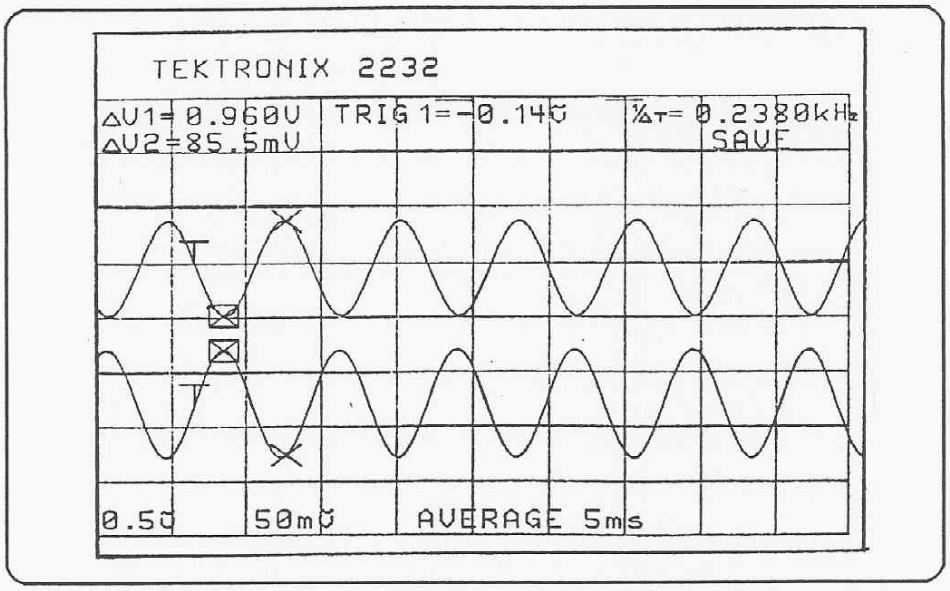

Figure 2.29 - System response for AC measurements, sine wave with f=476 Hz applied to PZTA (top: servo output, 86 mV_{pp} ; bottom: input signal, 0.96 V_{pp}).

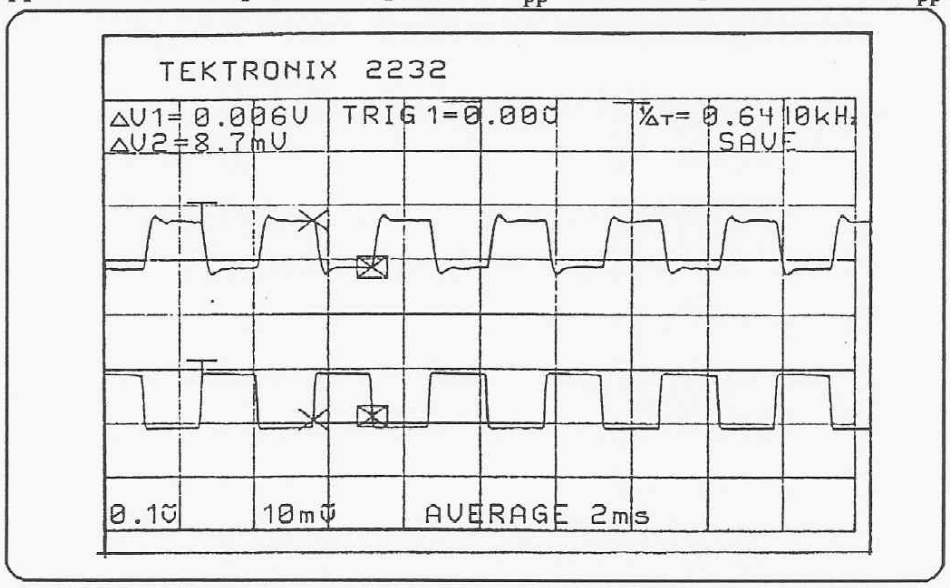

Figure 2.30 - System response for AC measurements, square wave with f=1.28 kHz applied to PZTA (top: servo output, 9.3 mV_{pp} ; bottom: input signal, 0.10 V_{pp}).

From these two figures, it can be seen that the "white-light" interferometer works very well for the tracking of AC measurands, even for signals with frequency up to 1.3 kHz. These two results show the realization of the principle of Active Phase Tracking Homodyne (APTH) signal processing, operating in the mode HGBP, ie, the signal frequency is recovered from the servo's output voltage ($\Delta V_{feedback}$) because the signal frequency is less than the corner

frequency of the feedback servo, and hence the photodetector output voltage will remain pratically constant.

2.3.3.3 Resolution

To estimate the phase resolution ($\Delta\phi_{min}$) of the "white-light" interferometric system, a small amplitude (rms value) test signal ($\phi_{signal} < 0.28$ radians), with a frequency inside the bandwidth of the servo (HGBP mode), was applied to the PZTA (sensing interferometer).

With the system maintained in quadrature and for a signal-to-noise ratio (S/N) of one, the phase resolution can be estimated using the following relation:

$$\Delta\phi_{min} = \frac{\phi_{signal}}{\sqrt{B}}\ 10^{(N-S)/20} \qquad (41)$$

where ϕ_{signal} is expressed in radians, N is the noise floor expressed in dBV, S is the interference signal detected at the output by the photodetector also in dBV, and B is the bandwidth used by the spectrum analyzer in the measurement. Thus, $\Delta\phi_{min}$ will be expressed in radian/$\sqrt{Hz}$. This value represents the minimum optical phase which can be detected by the system, or, in other words, the sensitivity (or resolution) of the system, and it is normalized within 1 Hz bandwidth for S/N ratio of one.

Figure 2.31 shows one measurement of the output of the system for an applied phase signal of 100 mrad (peak amplitude) to the PZTA at 482.5 Hz, with the system locked at quadrature and with the two PZT´s (PZTb1 and PZTb2) working in anti-phase.

At 482.5 Hz the S/N ratio was 41.42 dB (N=-97 dBV, S=-55.58 dBV), measured in a bandwidth of B=9.5485 Hz, which, substituted in the relation (41), gives a minimum detectable phase of $\Delta\phi_{min} = 0.27$ mrad/$\sqrt{Hz}$ (peak amplitude).

The laser diode was biased at 71 mA and the corresponding fringe visibility was 0.34. The harmonics that we can observe in multiples of 50 Hz are due to the servo circuit, which was not shielded.

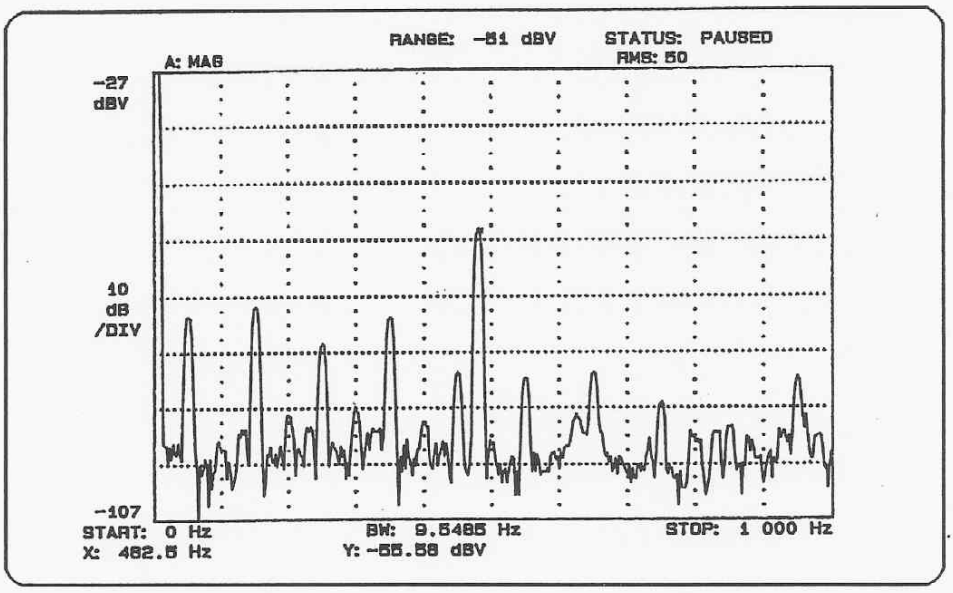

Figure 2.31 - System output for an applied signal of
100 mrad (peak amplitude) to PZTA (f=482.5 Hz).

In figure 2.32, with the same previous conditions, the amplitude of the applied signal was increased and we observed that the noise level remains the same (noise level ≈ -98 dBV).

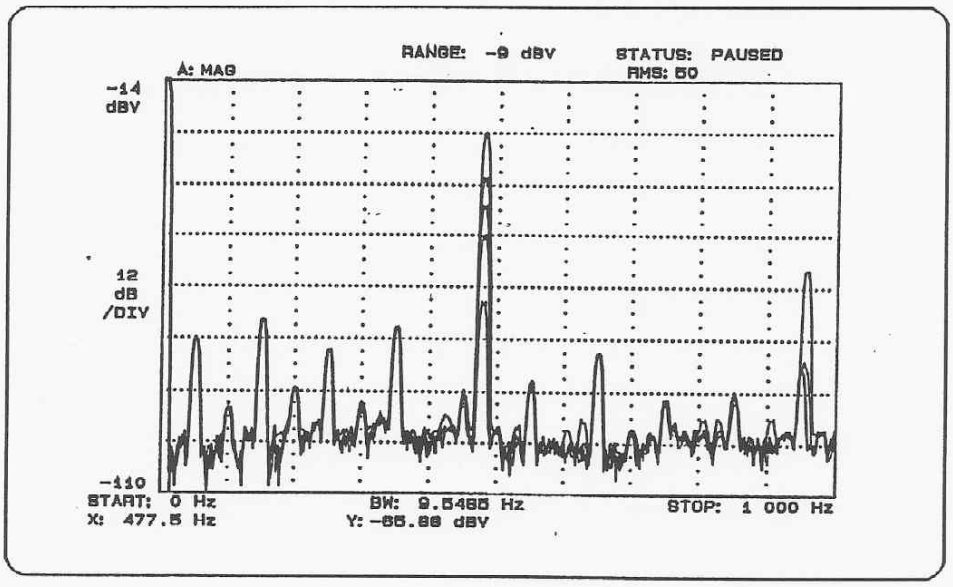

Figure 2.32 - System output for several
signal amplitudes applied to PZTA.

Figure 2.33 shows the phase resolution of the system, for a S/N ratio of one, and with the system in quadrature, for an applied phase signal of 100 mrad (peak amplitude).

A phase resolution between 1 mrad/√Hz and 0.3 mrad/√Hz was obtained in the frequency range 30 Hz to 600 Hz.

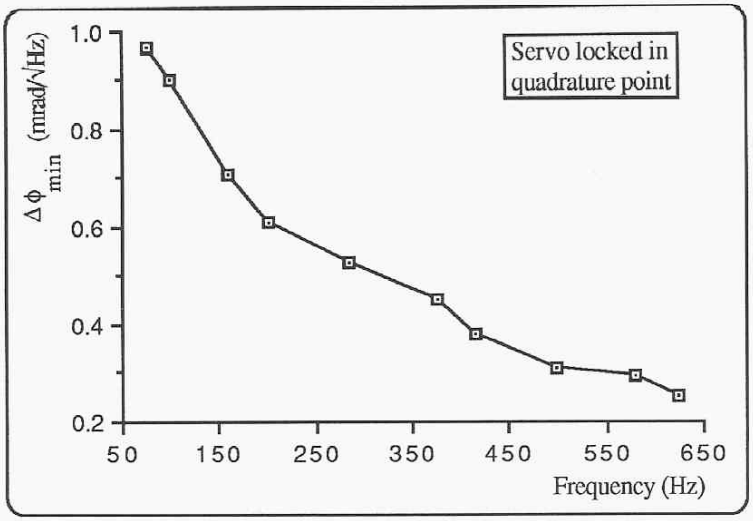

Figure 2.33 - Minimum detectable phase of the system (100 mrad - peak amplitude - applied to PZTA).

The dynamic range† of the system was ≈ 90 dB over the same frequency range, as shown in figure 2.34.

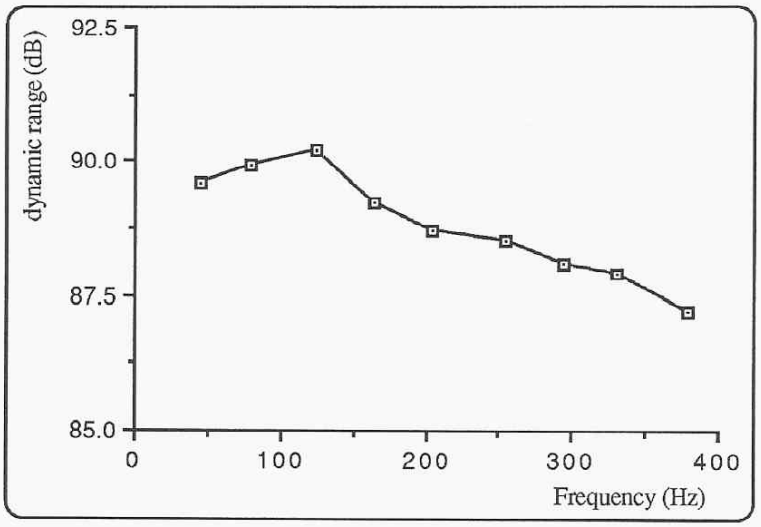

Figure 2.34 - Dynamic range of the system.

---

† The dynamic range was calculated using the following relation: $dyn = 20 \log\left(\frac{\phi_{max}}{\Delta\phi_{min}\sqrt{B}}\right)$, where ϕ_{max} is the maximum tracking range of the servo.

2.4 Applications to Accelerometers/Geophones

The measurement of acoustic pressure, acceleration or surface velocity is important for industrial applications and geophysical surveys. Several authors have described accelerometers [43,44,45] and hydrophones [46] based upon fibres wrapped around some form of compliant cylinder. In a typical arrangement, the fibre forms one or both arms of the fibre optic interferometer, which may be a Mach-Zehnder or a Michelson configuration. The measurand induced dimensional changes in the cylinder are transferred to the fibre, inducing a phase change in the interferometer. The sensitivity has been further enhanced by using dual compliant cylinders in a "push-pull" arrangement in the fibre Michelson configuration, as the light passes through each sensor coil twice [43,44].

The "push-pull" configuration also acts to greatly reduce the sensor's cross sensitivity to temperature and pressure variations, since both cylinders are affected by these influences, and the differential operation provides common mode rejection of these effects [43,44]. Using this approach, resolutions better than 10^{-9} g/$\sqrt{Hz}$ have been achieved in prototype accelerometers, with dynamic ranges of $\approx$ 100 dB. In many applications such high resolutions are not required. As the sensitivity of the compliant cylinder accelerometer is determined by the number of fibre turns, the inertial mass, the bulk modulus and the diameter of the cylinder, the ratio "range to resolution" can be tailored for a specific application. In many industrial applications for accelerometers, resolutions between 10^{-6} g/$\sqrt{Hz}$ to 10^{-3} g/$\sqrt{Hz}$ are adequate, thus modest resolutions of only 10^{-3} rad/$\sqrt{Hz}$ to 1 rad/$\sqrt{Hz}$ are necessary for accelerometer configurations similar to those described in references [43,44,45]. This level of resolution (10^{-3} rad/$\sqrt{Hz}$) can be readily achieved with "white-light" interferometry (WLI).

Although resolutions obtainable using WLI are lower than those obtainable using a highly coherent source, the WLI technique provides several advantages : (i) as the low coherence source is not affected by feedback, an isolator is not required [15,22]; (ii) the absolute value of the measurand is recoverable on "switch-on" [12,13], enabling the accelerometer to be used in applications such as inertial guidance.

Data is presented in figure 2.34, which shows that if the system was used to process the output from a compliant cylinder type accelerometer, resolutions of $\approx 10^{-7}$ g/$\sqrt{Hz}$ could be achieved.

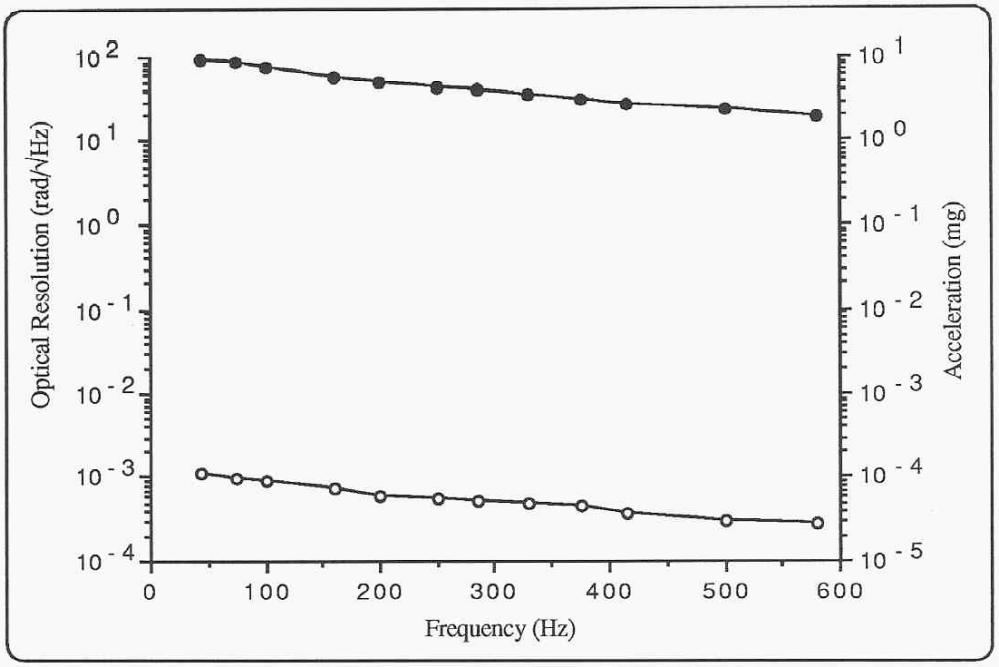

Figure 2.34 - System performance, as a function of frequency, when the system is used to interrogate a mass loaded compliant cylinder fibre optic accelerometer/geophone [43,44].

In figure 2.34, the lower data points give the minimum detectable phase changes, and the upper data points represent the maximum tracking range of the servo. The right hand column shows the predicted resolution and maximum acceleration levels achievable when the system is used to interrogate a mass loaded compliant cylinder fibre optic accelerometer with a sensitivity of 10^4 rad/g as reported by Gardner [43,44].The predicted acceleration resolution is better than 10^{-6} g/$\sqrt{Hz}$ in the frequency range 30 Hz to 600 Hz.

3. *Fibre Optic Pressure/Temperature Sensor for Down-Hole Environment*

3.1 Introduction

In this chapter, a dual fibre optic Fabry-Perot sensor adapted to the permanent monitoring of oil-wells and providing a simultaneous determination of pressure and temperature in a down-hole environment is described.

The sensor includes two low-finesse Fabry-Perot interferometers, which will be connected in a reflective array network, to be multiplexed in time, and with their status read using coherence sensing. In the evaluation of the system, two low coherence sources, one Surface Light Emitting Diode (SLED) and one multimode laser diode at 1.3 μm wavelength, were used. We begin by measuring the auto-correlation functions of the two light sources.

The receiving interferometer consists of a bulk Michelson interferometer with a servo incorporated, in order to eliminate the static phase fluctuations. Following the study, we present the design and characterization of each sensor (pressure and temperature) for different light sources, using the "white-light" interferometry approach.

Finally, the combination of time division multiplexing with coherence sensing for the demodulation scheme is reviewed.

3.2 The Optical Sources

For the measurement of the auto-correlation function of the two optical sources, we used the same experimental arrangement described in the section 2.2, where a variable path-length bulk Michelson interferometer was used. The normalized auto-correlation function of the Surface Light Emitting Diode (SLED) is described by equation (14) whilst that of the multimode laser diodes is approximately described by equation (16).

3.2.1 The SLED

The light source was the Surface LED IRE-161 from Laser Diode, Inc., with an operating wavelength of 830 nm and spectral width of 45 nm. The averaged emitted light power is 1.4 mW when it operated with a forward current of 100 mA [47].

In figure 3.1 the fringe visibility function of the SLED is shown as a function of the optical path-length imbalance of the Michelson interferometer, for a DC current of 100 mA.

The scan was not performed using a translation stage, but by applying a DC voltage to the PZT mounted on mirror M1 (see figure 2.1), in order to have small displacement steps (of the order of a micron). For this PZT and for λ=830 nm, 1 μm of displacement (d) was equivalent to 58.8 mV applied voltage ($\Delta L=2d$).

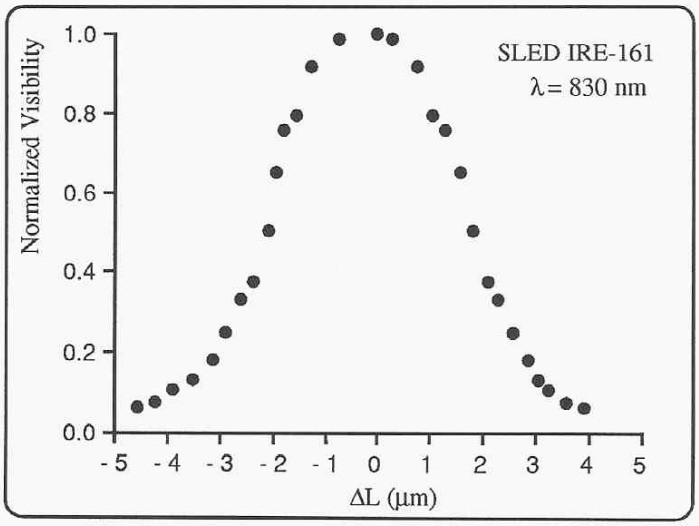

Figure 3.1 - Fringe visibility versus path-length imbalance
(data normalized to the visibility at $\Delta L=0$).

From figure 3.1, the coherence length (assuming a gaussian lineshape) is 10 μm. Using equation (11), and for a spectral width of 45 nm, the theoretical coherence length is 10.2 μm. As we can see, the agreement is very good. The advantage of having this type of light source is the low price and also the short coherence length, which is very important, if we want to implement a low-finesse Fabry-Perot sensor using "white-light" interferometry.

To have sufficient light power at the optical sensor probe, we used multimode graded-index fibre; however, difficulties were experienced when a low-finesse Fabry-Perot cavity built with this type of fibre was used. This problem will be explained in section 3.3.

3.2.2 The Multimode Laser Diode

The multimode laser diode was the HLP5400 from Hitachi, with a lasing wavelength of 1318 nm, at 3 mW of output power. The emitted output power is 3 mW when the laser is biased at 20 mA above threshold, as we can see from the experimental data shown in figure 3.2 (this data was measured without temperature control and was obtained using a Photometer from UDT - model 370 - with the photodetector head 300nm-1500 nm and a neutral filter providing an attenuation of 30 dB. The slope efficiency was found to be 0.14 mW/mA and the threshold current (I_{th}) 16 mA, which agree with values given by the manufacturer [48]. The HLP5400 laser type is easily damaged by excess current, because of the low threshold current and the high slope efficiency. The laser diode chip is mounted in a way that it is open to the air (A-type package); therefore, some precautions should be taken in handling it [48].

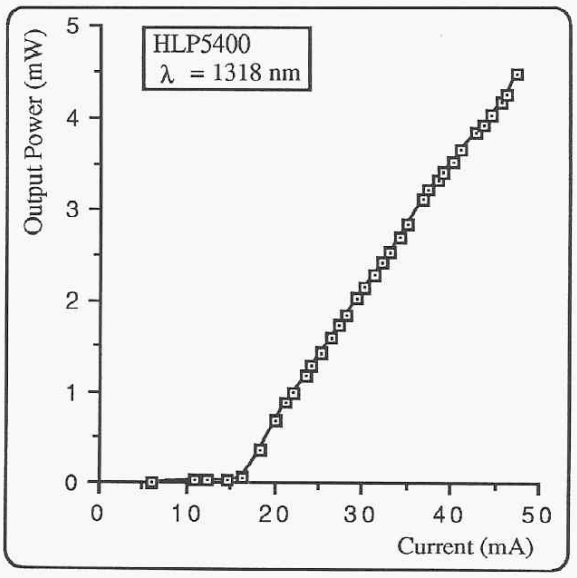

Figure 3.2 - Ouput characteristic of the laser diode HLP5400.

Figures 3.3 and 3.4 show the fringe visibility using the laser diode HLP5400, as a function of the path-length imbalance of the Michelson interferometer. Figure 3.3 is for CW operation, with the laser diode running 15 mA above threshold; figure 3.4 is for the case of the laser being modulated with a 6 MHz square wave, biased at threshold and with an injection current amplitude of 15 mA. These figures show the peaked structure for the visibility function that is typical of multimode laser illumination, as we have already described in chapter 1.

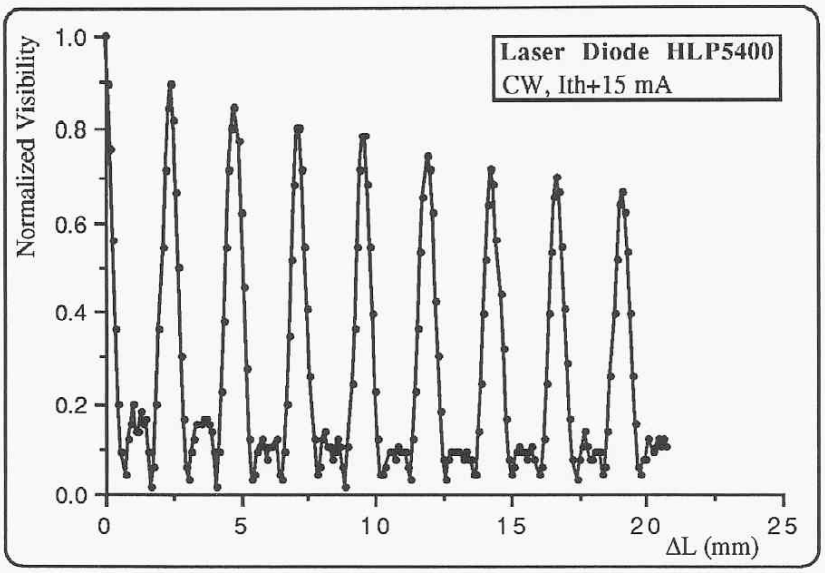

Figure 3.3 - Fringe visibility versus optical path imbalance for the laser operating CW (visibility normalized to its value at ΔL=0).

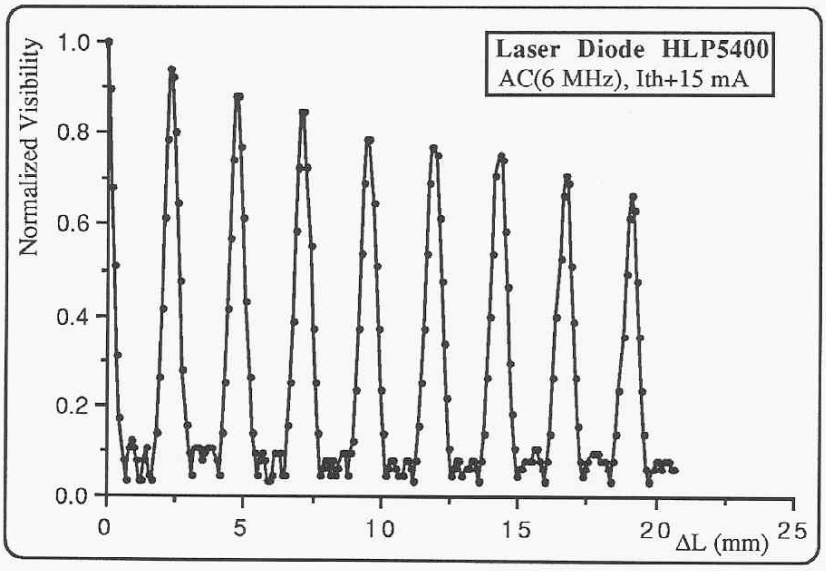

Figure 3.4 - Fringe visibility versus optical path imbalance for the laser being modulated (visibility normalized to its value at ΔL=0).

The peak separation is ≈ 2.4 mm, which gives a laser cavity length of ≈ 330 μm (for an active layer refractive index of 3.5), and a longitudinal mode separation of ≈130 GHz. It can be seen that the laser diode modulation does not change the form of the visibility function, hence a

multiplexing scheme based on time division plus coherence tuned sensing can be achieved, by direct modulation of the laser injection current [22].

Because the coherence length (L_c) of the laser radiation (as determined by the envelope of the visibility function) is very large relative to the desired cavity length of the low-finesse Fabry-Perot, the mode 2 of operation corresponding to case II (in section 1.3) for "white-light" processing cannot be applied. Therefore, we must operate the system in case I (section 1.3), where coherence tuned sensing is implemented choosing the optical path-length imbalance of the sensing and the receiving interferometers in such a way that they coincide with a region where the corresponding visibility is very low, ie, in the range between two successive peaks of interference visibility. Figure 3.5 gives the visibility variation in the central interference zone, again for the laser operating CW and modulated.

The width at half-height (W) for the central interference area is W(CW; I_{th}+15 mA)≈ 334 μm and W(AC; I_{th}+15 mA)≈ 298 μm. The optical path-length imbalance of the interferometers must be at least 550 μm, in order to obey the condition explained above.

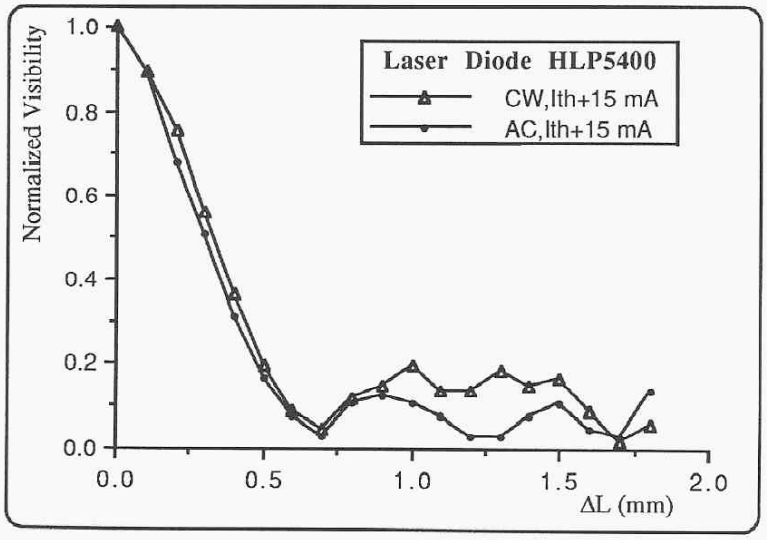

Figure 3.5 - Central area of the visibility funtion (I_{th}+15 mA).

When coherence sensing is combined with time multiplexing, the path-length imbalance of the sensing interferometers can be equal. This is an important advantage because the sensitivities of the sensors can all be identical, and they could be increased if the first regions of low visibility (ie, the first two interference areas) were selected, which gives an important practical consideration when miniature sensors are required.

3.3 The Pressure/Temperature Sensor

In this experiment we tried two different types of design for the sensor heads according to the power capability of the light sources available (SLED and multimode laser diode).

Using the SLED with multimode graded-index fibre, the low-finesse Fabry-Perot design did not work, because the interference produced between the two Fresnel reflections (P1 and P2), one from the fibre end and the other from the low reflection mirror (see inset box in figure 3.6) are not spatially correlated, ie, they will propagate in distinct modes of the multimode fibre, hence the resulting fringe visibility is very low. At the ouput of the multimode fibre we will have a speckle pattern due to the interference between modes. The visibility of the resulting fringes pattern vary, depending on the relative delay of the modes relative to the coherence length of the light source [49]. So, it is possible that the light which is reinjected (P2) into the fibre in the Fabry-Perot cavity, will be only due to a small fraction of the modes of the fibre. Then, that fraction (P2) will recombine with the 4% originated in the Fresnel reflection (P1), which have the contribution from all guided modes of the fibre; hence, only a weak interference effect will be produced. Due to this problem, we used a bulk Michelson miniature interferometer for the sensor head, because with this type of interferometer we have more power at the output of the system and also the fringe visibility will be greater.

Using the multimode laser diode with single mode fibre, the low-finesse Fabry-Perot design for the sensor probe was a good choice. To simulate the pressure action on a deformable membrane, we used a PZT disc with a silvered planar glass mirror attached, and by application of a high DC voltage (HVA) we produced the corresponding deformation of the membrane.

The experimental arrangement used for the calibration and characterization of the sensors is shown in figure 3.6. When the sensor was the low-finesse Fabry-Perot the LCS used was the multimode laser diode HLP5400, operating CW with an injection current of 28 mA, and emitting an average power of 1.3 mW. The PZT disc had an efficiency of 0.43 rad/V at 500 Hz, and the cavity length was $\approx$ 620 μm in order to work in the low visibility region, as we will show in the following section. In the receiving interferometer, the photodetector (D) used was a InGaAs PIN photodiode PD7005 (for λ=1300 nm, from Mitsubishi [20]), with two amplification stages (A) (see appendix C2), giving an overall gain of 6.94×10^5 V/W, a -3 dB bandwidth of $\approx$ 2.3 MHz and a noise floor of 2.6 $\mu V/\sqrt{Hz}$.

The conversion gain of the PZT in the receiving interferometer ($\Delta\Phi/\Delta V_{feedback}$) was found to be 0.52 rad/V. The high voltage amplifier (HVA) was from Physik Instruments (model P-263), with an amplification factor of 136, a - 3 dB bandwidth of 80 Hz (for a 10 nF load) and an output voltage range of 0 to -1360 V, for an input voltage variation of 0 to 10 V. On the servo circuit (appendix B) the HVA amplification stage was removed and the output was modified in order to adjust the voltage to the range of the input voltage of the P-263 HVA; also, the values for the integration constant and the monostable (appendix B) were changed to the following values: R_1=10 kΩ, C=0.22 μF; (timer) R_o=510 kΩ, C_o=1 μF. Therefore, the - 3 dB bandwidth of the feedback loop was approximately 80 Hz, which was sufficient for this type of quasi static measurement of temperature and pressure. The length of the lead fibre (L_d) was 1.2 km (fibre attenuation: 0.5 dB/km), which was used to simulate the large distance in the oil-wells (the DC coupler had a nominal coupling ratio of 50%). The microscope objectives had a numerical aperture of 0.25 and an operating focal length of 6 mm.

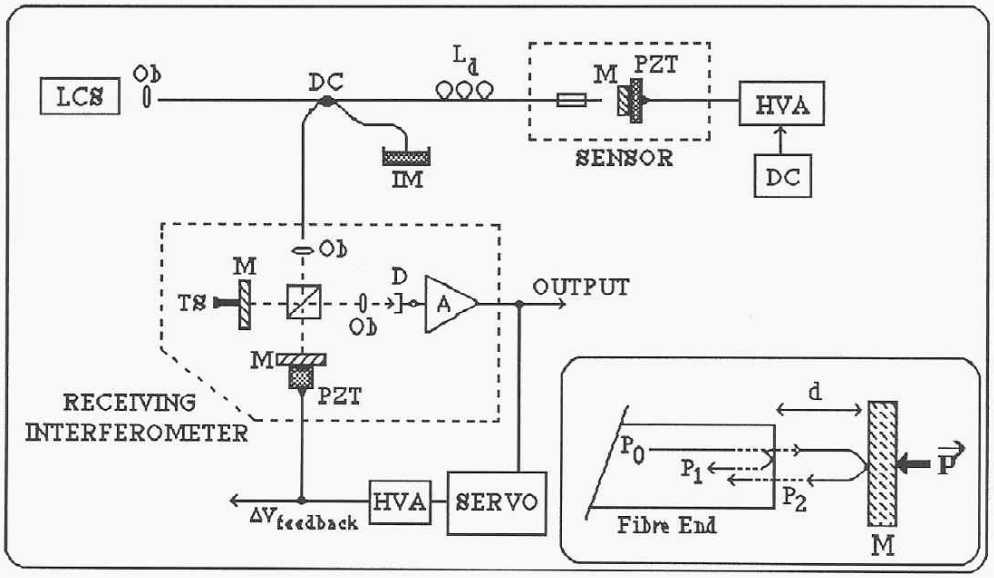

Figure 3.6 - "White-Light" system with a low finesse Fabry-Perot sensor and a bulk Michelson receiving interferometer with a tracking servo system.

(Ld: Lead Fibre; HVA: High Voltage Amplifier; D: Photodetector)

(LCS: Low Coherence Source; DC: Directional Fibre Coupler; M: Mirror)

(IM: Index Matching Gel; TS: Translation Stage; Ob: Microscope Objective)

For the case of the sensor probe based on a bulk Michelson miniature interferometer, we used the SLED source operating at 100 mA, emitting an average power of ≈ 1.4 mW. The photodetector was the same used in the previous experiment (appendix C1). The multimode graded-index fibre was from Corguide, Inc. (attenuation at 830 nm : 3.7 dB/km) and the nominally 50/50 directional coupler (DC) was also built with multimode graded-index fibre, from Gould, Inc. The lead fibre (L_d) had a length of 300 m, for this case. These two types of optical sources were tried, in order to have a comparative study between both approaches. The use of the SLED source, is not a convenient alternative in the application of deep down-holes, because the optical power supplyed is very low and, in conjunction with larger fiber attenuation at 830 nm. Using a laser diode source at 1300 nm wavelength, substantial light power can be coupled into the fibre, and the fibre attenuation will be small, which allows for the distance between the surface control unit (light source plus receiving unit) and the sensor head, to be very large (7 to 15 kilometers). In the following sections, the design, characterization and resolution of each sensor type, will be presented for the two light sources considered.

3.3.1 The Low-Finesse Fabry-Perot Sensor

Fibre optic Fabry-Perot sensors have many applications because they are highly sensitive to temperature, mechanical vibration, acoustic waves, magnetic fields, etc [50].

Techniques to produce the Fabry-Perot cavities have been described in the literature, using air-glass interfaces at the fibre ends as the reflectors [51], semi-reflective splices in a continuous length of fibre [52], birefringent quartz crystal cavities [53], or glass plates with partial reflective coatings [54]. For pressure measurements over a wide temperature range, the requirement of a small sensor head, in order to minimize the temperature cross sensitivity, is of paramount importance, and can be fulfilled using a low-finesse Fabry-Perot interferometer with a short optical cavity. The use of "white-light" interferometry for the interrogation of such small optical cavities with the requirement of miliradian resolution, is very problematic. Recently, a new approach used to interrogate a low-finesse Fabry-Perot optical cavity has been demonstrated [55], based on the generation of two interferometric outputs in quadrature, which does not impose any basic constraint on the minimum cavity length as well as on the resolution that can be achieved. However, this technique uses a large coherence length source

(singlemode laser diode), which is not the case of our "white-light" interferometric system. This system, used two low-finesse Fabry-Perot sensors, providing a simultaneous determination of pressure and temperature for a down-hole environment. Their phase information can be multiplexed in time, and the temperature value, given by the temperature sensor, will be used to correct the residual thermal dependence of the pressure sensor.

3.3.1.1 Design of the Probe

Figure 3.7 shows a schematic design of the sensor probe used, with the two low-finesse cavities included. For the design of the temperature sensor, instead of quartz we used a capillary metal tube (with an internal diameter providing a sliding fit for the jacketted fibre), with a plane glass mirror cemented at the end; the reason was that the thermal expansion coefficient of the metal is higher than the quartz.

In the pressure sensor (figure 3.7) the PZT acts as a simulator, producing a linear displacement equivalent to the displacement of a thin diaphragm under the action of an uniformly applied differential pressure, which arises solely from bending forces, provided that the total displacement is small. As a consequence, the displacement is linearly dependent on the differential pressure [56]. This displacement, was produced by applying a high DC voltage to the PZT disc.

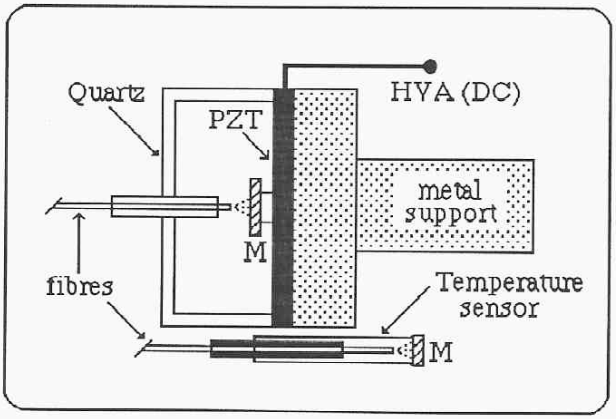

Figure 3.7 - Scheme of the sensor head,
showing the pressure and temperature sensors.

To determine the length of the cavity (in order to work in the low visibility region of the autocorrelation function of the laser light), the receiving interferometer was removed and the

optical power from the output port of the directional coupler, which illuminates the receiving interferometer, was measured as a function of the cavity length (L_{cav}). The length variation was performed with a translation stage attached to the fibre in the cavity. This result is shown in figure 3.8. The distance, d, between the far end of the fibre and the mirror (M) in the cavity (see inset box in figure 3.6) must be, at least, 550 μm; in this situation, the optical beams reflected by the fibre end (P1), and reinjected into the fibre after reflection in the mirror (P2), will have similar power levels; therefore, the visibility of the interferometer fringes will be maximized. Also, this length will be in the region where the visibility of the autocorrelation function of the laser light is low.

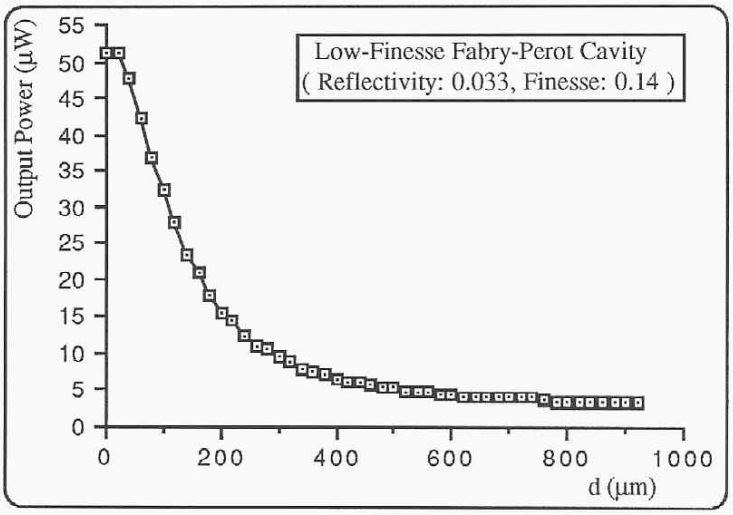

Figure 3.8 - Optical power reinjected into the single mode fibre as a function of the cavity length (laser HLP5400).

A sinusoidal test signal (amplitude: 17.7 V; frequency: 44.4 Hz) was applied to the PZT disk, and the length of the cavity was set to be ≈ 620 μm. By tuning the path-length imbalance of the receiving interferometer to be equal to the path-length imbalance of the low-finesse Fabry-Perot cavity, the interference pattern at the output of the receiving interferometer was found to have a visibility of 0.38 (figure 3.9). The detected optical power was 0.4 μW.

The interference pattern observed had the shape shown in figure 3.9, which can be theoretically described by relation (18), because the transfer function for this type of Fabry-Perot cavity is approximately the transfer function of a two-beam interferometer.

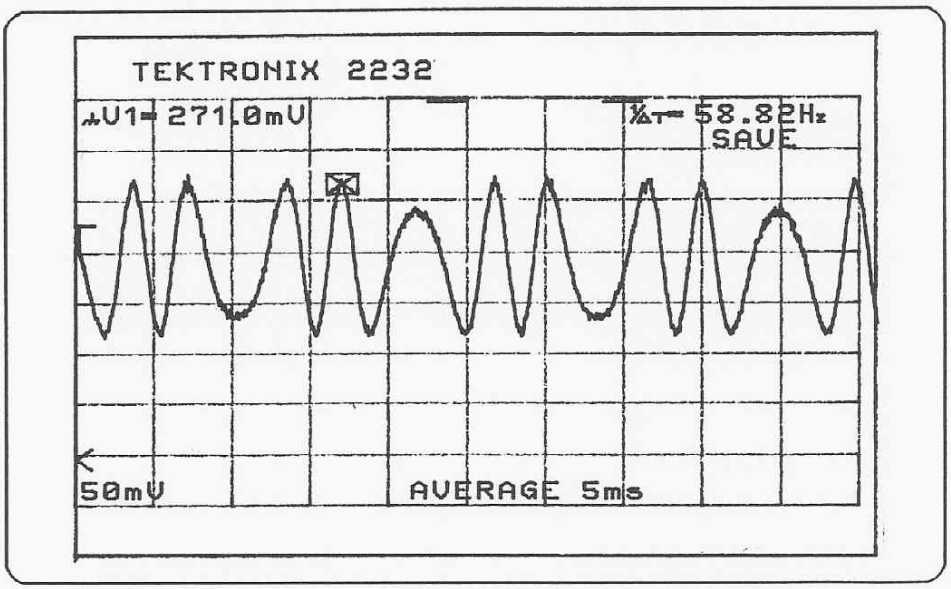

Figure 3.9 - Fringe interference pattern observed at the output of the receiving interferometer, when $\Delta L_{receiver} = \Delta L_{cav} \approx 620\ \mu m$.

The transfer function of a Fabry-Perot interferometer in a reflective configuration, with two identical mirrors (ie, having the same reflectivities) is [13]:

$$I_{cav.out} = I_o \left[1 - \frac{(1-R)^2}{1+R^2 - 2R\cos \Delta\phi} \right] \tag{42}$$

where R is the power reflectivity of the cavity mirrors, I_o is the optical power into the cavity and $\Delta\phi$ is the optical phase difference, which is given by $\Delta\phi \approx 4\pi n_{cav} d/\lambda$ ("n_{cav}" is the refractive index of the cavity, "d" is the length of the cavity and "λ" is the wavelength of the light source). If the reflectivities of the two mirrors are equal and small ($R<<1$), and neglecting the terms arising from the interference of the beams that undergo more than one reflection in the mirrors, expression (42) will be approximated by:

$$I_{cav.out} = 2RI_o (1 - \cos \Delta\phi) \tag{43}$$

which is the transfer function of a two-beam interferometer.

The finesse of the cavity is given by [13]:

$$F = \frac{4R}{(1-R)^2} \tag{44}$$

It has been shown [57] that, for a Fabry-Perot cavity with a finesse of 0.14 illuminated by a coherent source, the error introduced by approaching the Fabry-Perot transfer function by a two-beam transfer function is less than 6%. However, if the cavity is kept in a quadrature position by using some kind of servo system, the error introduced by this approximation is less than 1%, for reflectivities smaller than 10%. In the case of "white-light" processing using a receiving interferometer, a two-beam transfer function is generated independently of the reflectivity [57]. So, by using the system presented in this work, the measurement of differential pressure via displacement of a pressure responsive element is possible, with several advantages, such as intrinsic safety, small size, EMI/EMP immunity, remote monitoring and multiplexing ability.

3.3.1.2 Resolution

To evaluate the minimum phase resolution of the system, a small phase signal (amplitude: 140 mrad; frequency: 260 Hz), was applied to the PZT disc in the cavity.

From figure 3.10, the measured sensitivity, for a signal-to-noise ratio of one and with the system at quadrature, was ≈ 0.8 mrad/√Hz (this was calculated using equation (41)).

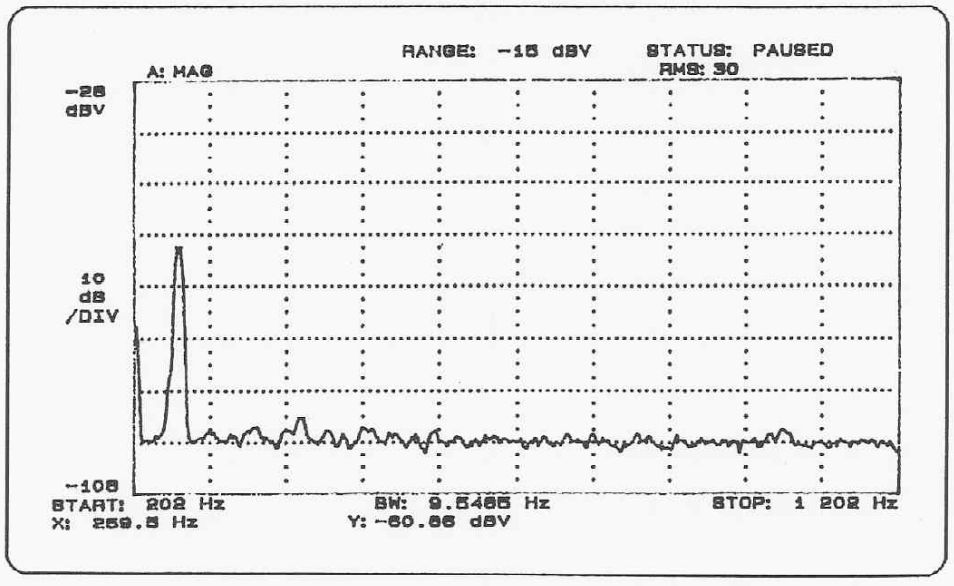

Figure 3.10 - Output of the system when a test signal of 140 mrad (peak amplitude) was applied to the cavity mirror.

The sensitivities of the pressure sensor (which, in this particular case, will be the displacement sensitivity achieved by this type of sensor) and the temperature sensor were estimated using the following relations [13]:

$$S_{displacement} = \frac{\Delta\phi_{min}\,\lambda}{2\pi} \qquad [m/\sqrt{Hz}] \qquad (45)$$

$$S_{temperature} \approx \frac{\Delta\phi_{min}\,\lambda}{2\pi}\left[\frac{1}{n_{cav}\,\alpha}\right] \qquad [K\ m/\sqrt{Hz}] \qquad (46)$$

where "n_{cav}" is the refractive index of the Fabry-Perot cavity (n_{cav} =1), and $\alpha = \frac{\partial L}{L \partial T}$ is the thermal expansion coefficient of the metal tube (α= $5x10^{-5}$ K^{-1} [27]). Using the values $\Delta\phi_{min}$=0.8 mrad/$\sqrt{Hz}$ and λ=1318 nm in the relations (45) and (46), the corresponding sensitivities are $1.65x10^{-10}$ m/$\sqrt{Hz}$ (for the displacement) and $3.4x10^{-6}$ K.m/$\sqrt{Hz}$.

The mirror (M) in the cavity was translated by applying an high DC voltage to the PZT disc. With the receiving interferometer in quadrature, coherently tuned to the sensor (ie, $\Delta L_{receiver} = \Delta L_{cav} \approx 620$ μm), we measured the corresponding variation of the servo feedback voltage. This feedback voltage variation, as a function of the mirror displacement, is given in figure 3.11. Figure 3.12 shows a fraction of the plot of the figure 3.11 for the same experimental conditions. The slope of the linear relation was $\Delta d/\Delta V_{feed}$ = 118.6 nm/V.

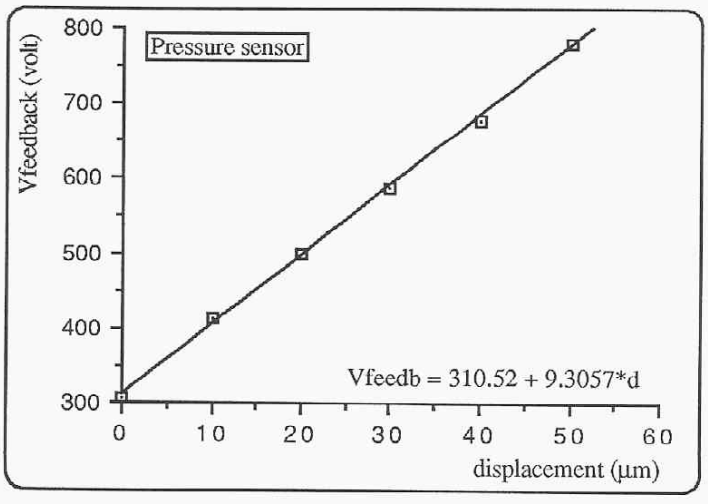

Figure 3.11 - Feedback voltage versus displacement, induced by the voltage applied to the PZT disc.

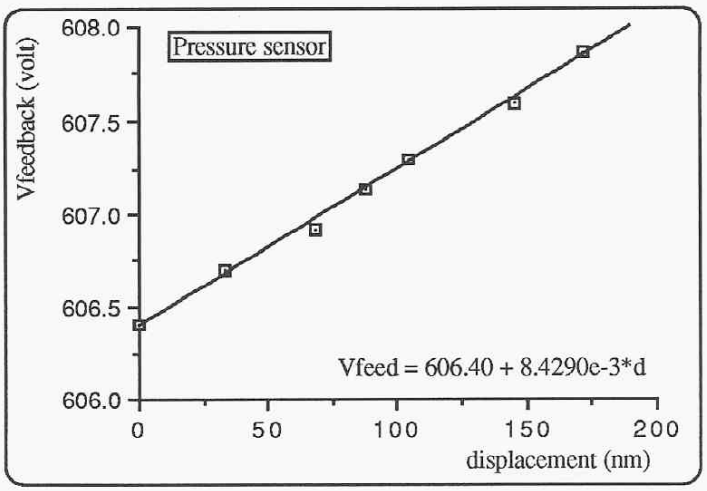

Figure 3.12 - Feedback voltage versus displacement, induced by the voltage applied to the PZT disc.

The temperature sensor interferometer was placed inside a furnace, with the temperature monitored with a thermocouple. With the same experimental conditions as before, we measured the corresponding feedback voltage. Figure 3.13 shows the results. The linear relation obtained had a slope of $\Delta T/\Delta V_{feed} = 0.2$ °C/V.

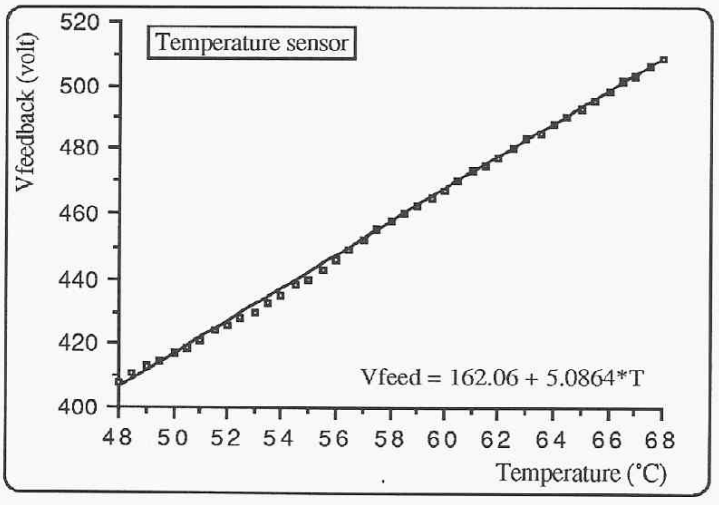

Figure 3.13 - Feedback voltage versus temperature variation.

3.3.2 The Bulk Michelson (miniature) Sensor

For the case where the optical source was the SLED, we used a bulk Michelson (miniature) interferometer (figure 3.14) for the sensor head, and multimode graded-index fibre for the guidance of the optical information. The path-length imbalance of the interferometer was chosen to be higher than the coherence length of the SLED(> 10 μm, see figure 3.1), in order to meet the condition of "white-light" interferometry. The beam splitter cube (BS) had one of the sides silvered, thus providing the other mirror necessary to implement the Michelson interferometer. The opposite side had index matching gel (IM), in order to eliminate the Fresnel reflection on that side. The other mirror was cemented at the center of the PZT disc, used once again to simulate the pressure effect. The microscope objective had a numerical aperture of 0.40 and an operating focal length of 1.9 mm. The SLED was operated at a bias current of 110 mA, and the detected power at the output of the receiving interferometer was 1.6 μW.

The fringe visibility at the output was found to be 0.20, when the interferometers were balanced.

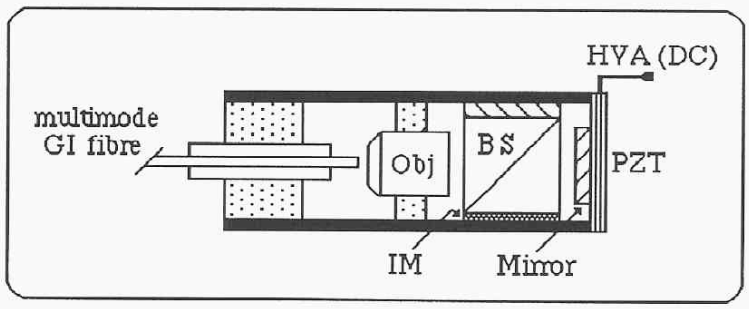

Figure 3.14 - Design of the sensor head.

(BS: Beam Splitter Cube, IM: Index Matching Gel)

(Obj: Microscope Objective, GI: Graded Index)

3.3.2.1 Resolution

The minimum phase signal detected by the system was measured when a small phase signal (amplitude: 120 mrad; frequency: 210 Hz), was applied to the PZT disc in the sensing interferometer. The low frequency signal was 34.5 dB above the noise floor (= - 86 dBV) in a baseband bandwidth of 4.77 Hz. Thus, the resolution of the system, for a signal-to-noise ratio of one and with the system in quadrature, was found to be ≈ 1.0 mrad/√Hz.

The corresponding displacement sensitivity is $\approx 1.4 \times 10^{-10}$ m/$\sqrt{\text{Hz}}$ (calculated using relation (45)). The feedback voltage variation as a function of the mirror displacement is given in figure 3.15, and the slope obtained was $\Delta d/\Delta V_{feed} = 0.13$ μm/V.

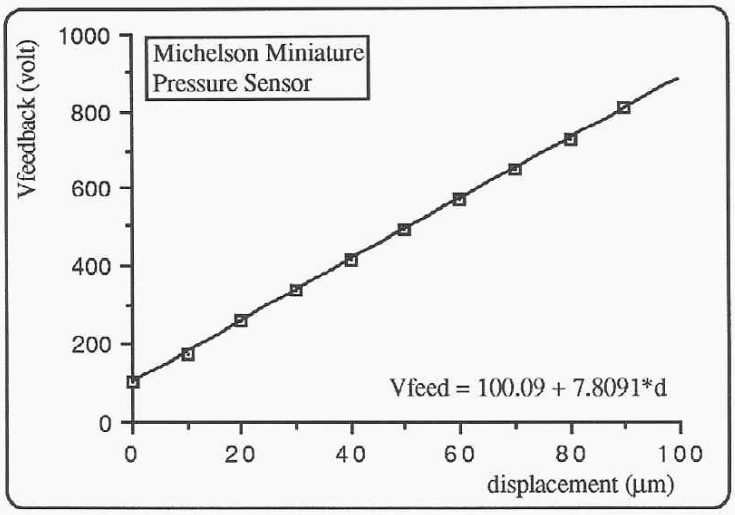

Figure 3.15 - Feedback voltage versus displacement induced by the voltage applied to the PZT disc.

3.4 Multiplexing Scheme

The method proposed is Time Division Multiplexing with Coherence Sensing (TDMCS) [15,22], ie., the reflective array of optical fibre sensors will be multiplexed in time and their status read using coherence sensing, with a directly modulated low coherence source.

The combination of time division multiplexing (TDM) with coherence sensing is an attractive concept because it enables the sensors to have a large unambiguous dynamic range and supports sensor self-initialization, which is particularly important for the measurement of slowly varying parameters; also, it allows the sensors to have the same path-length imbalance (making it feasible to fabricate identical sensor units with identical specifications).

Figure 3.16 shows the proposed experimental arrangement for the implementation of the TDMCS technique.

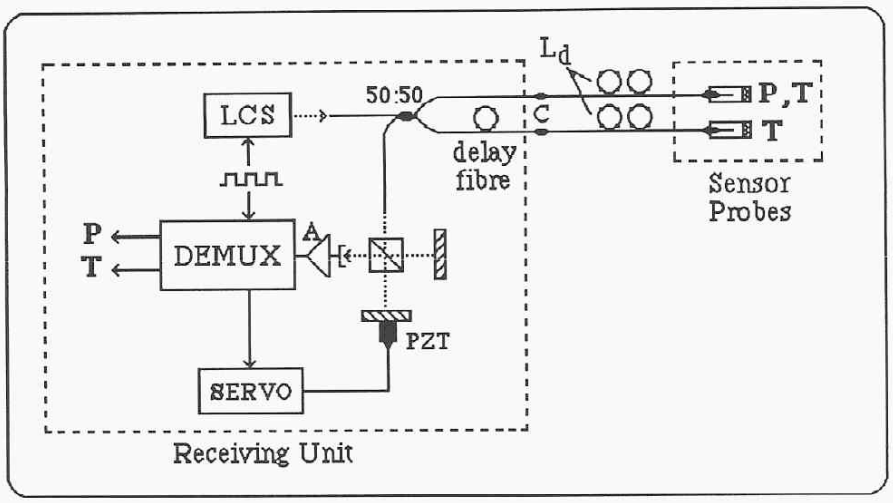

Figure 3.16 - Multiplexing scheme proposed for the measurement of absolute pressure (P) and temperature (T). (C: Optical Connectors, Ld: Lead Fibre, A: Amplifier)

Time division substantially reduces the level of source induced noise present in a system based uniquely on coherence multiplexing [59]. Also, reflective topologies have the important advantage that the total length of fibre is reduced, as well as the number of couplers and splices, when compared with equivalent transmissive topologies. In addition, because the light traverses each sensor twice, the sensitivity is doubled. The feedback effects due to the back reflected light into the laser cavity are negligible for multimode laser diodes, which makes the use of optical isolation unnecessary [22].

To ensure time division, the following conditions must be satisfied [22]:

$$a \leq \frac{2n_c L_{delay}}{c} \tag{47}$$

$$T \geq \frac{2(N-1)n_c L_{delay}}{c} + a \tag{48}$$

where "N" is the number of sensors, "n_c" is the effective refractive index of the fibre mode, "L_{delay}" is the length of the delay fibre between the channels, and "c" is the vaccum speed of light. The parameters "a" and "T" are defined by the modulation drive current applied to the

laser cavity, given in figure 3.17. With time division multiplexing each sensor is sampled in time and hence, to have complete signal recovery, the Nyquist criterion† must be satisfied.

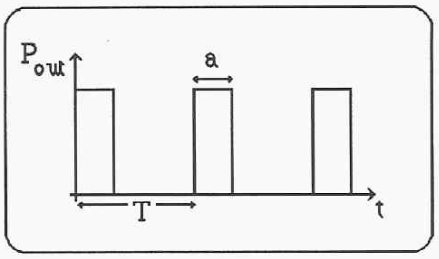

Figure 3.17 - Laser optical power output after modulation.

Optical crosstalk will be negligible if the duty cycle (a/T) of the emitted light waveform is less than 50%, which enables a good time separation of the sensor signals. In general, to maximize the average power in the network, the duty cycle (a/T) of the emitted waveform must be 1/N. This condition is also the most demanding in terms of crosstalk, because it just avoids the overlap of the optical pulses on the photodetector [22]. The main disadvantage of using time division multiplexing is the need of fast electronics , unless long optical delays are used in the system. Electronic crosstalk will always be present, but, by proper choice of the demultiplexing electronics, its value will be acceptable for most applications.

Yet, the scheme has some advantages such as: use of simple electronic decoding; single source and detector; can accomodate a large number of sensors.

The use of a bulk Michelson interferometer in the detection module will degrade the accuracy of the reading, because of the moving parts or mechanisms, which generally offer poor reliability features. The effect of scattering and residual reflections of the light in the bulk interferometer can be originated in the mirrors, beamsplitter, or in impurities and density fluctuations that can be present along the interferometer arms. The use of a beamsplitter with high quality AR coatings will reduce these effects [59].

If the mirrors in the reading interferometer are misaligned, so that the two interfering beams are no longer parallel at the detector, the output signal will be affected. It can be shown [59] that, even for very small angular misalignments, the number of fringes across the detector area can

---

† Nyquist criterion: to avoid signal degradation, the modulation period must be: $T \leq \frac{1}{2f_{max}}$, where it is assumed that the sensor frequency range does not exceed f_{max}.

be large and the detected intensity will approach an average value. The reduction of fringe visibility (and consequently of reading sensitivity) with mirror angular misalignment indicates that great care must be taken to keep the interferometer aligned.

To have a stable and reliable detection system, the system must be absolutely static and provide furthermore, a large adaptability of the choice of the detection bandwidth; this can be achieved using a dual-wavelength passive homodyne scheme [60], in order to remove the phase mismatch between the sensing and receiving interferometers and the 2π ambiguity in the phase determination. An important practical problem to be solved in the context of "white-light" interferometry, is to find and to track the first quadrature point of the visibility pattern. This can be done by finding the centroid of the interference region of interest, and then by a servo system, to move the receiving interferometer to one of the two first quadrature points [12].

This technique can be adapted to coherence reading in the context of Time Division Multiplexing systems.

4. Conclusion

4.1 Conclusions of the Work

The work accomplished and presented in this dissertation relates to the area of "white-light" interferometry in optical fibre based sensors for the measurement of both AC and DC measurands. Three different measurands were studied: acceleration, temperature and displacement (related to pressure).

A theoretical study of "white-light" interferometry , using different types of low coherence sources, and of its application to fibre optic sensing, was conducted. The advantage of using "white-light" techniques is the ability to initialise the system, to increase the unambiguous range of measurent and the independence from drifts in the source wavelength.

By using a multimode laser diode (as an alternative to conventional low coherence sources), an all-fibre receiving interferometric system with large tracking range and self-initialization, for remote signal processing of fibre optic accelerometers, was for the first time investigated. Phase resolution better than 1 mrad/√Hz at frequencies below 600 Hz was obtained, with a dynamic range of ≈ 90 dB.

Using the same interferometric technique, a fibre optic sensor for the measurement of absolute pressure and temperature in a down-hole environment was designed and investigated. The use of a 1300 nm wavelength laser diode source allows for the receiving interferometric unit to be very distant (several kilometres) from the sensor probe. The two measurands were obtained from the same output of the optical link, by tuning the receiving interferometer. A multiplexing scheme, based on time division multiplexing coherence sensing, was proposed for the processing of the two measurands.

4.2 Future Work

It naturally follows that an implementation of the pressure/temperature "white-light" sensor multiplexing scheme proposed could be tried. Other techiques of signal processing of the optical sensors, based on low-finesse Fabry-Perot cavities would be experimented, such as:

- Demodulation using two signal outputs in quadrature [50].
- Dual-wavelength approach [13].
- Electronical-scanning, using a "white-light" Fizeau interferometer and a linear CCD array [64,65,66].

Also, other configurations of the servo systems could be studied to realize a potentially more rugged systems for in "field" applications.

Appendix A

Polarization Controller

In the mechanical diagram of the polarization controller (only one section - see next page), the value for the internal radius (R_m) of the coil was calculated using relation (26).

Considering the following values for the parameters, the corresponding internal radii of the coils used were:

- Quarter-wave coil (m = 4), with one turn (N = 1) of single mode fibre of 125 μm nominal diameter, and $R_o = R_m + 3$ mm.

  @ $\lambda_o = 800$ nm => $R_m = R(4,1) = 16.38$ mm.

  @ $\lambda_o = 1300$ nm => $R_m = R(4,1) = 10.08$ mm.

The springs on both sides of the fractional-wave plate were used to induce a twist effect [25] on the polarization state of the light, when the coil is rotated. The rotation will directly rotate the orientations of the principal axes of the fibre, inducing birefringence and giving a behaviour analogous to that of a classical fractional-wave plate. Ulrich et al. [29] showed that this effect is due to a coupling between transversal and longitudinal components of the hybrid electromagnetic field, and they gave a value for the coefficient of the twist effect for any doped silica single mode fibre.

The polarization controller used in our experiments uses three of these elements in series, giving a complete control of the polarization state of the light [26].

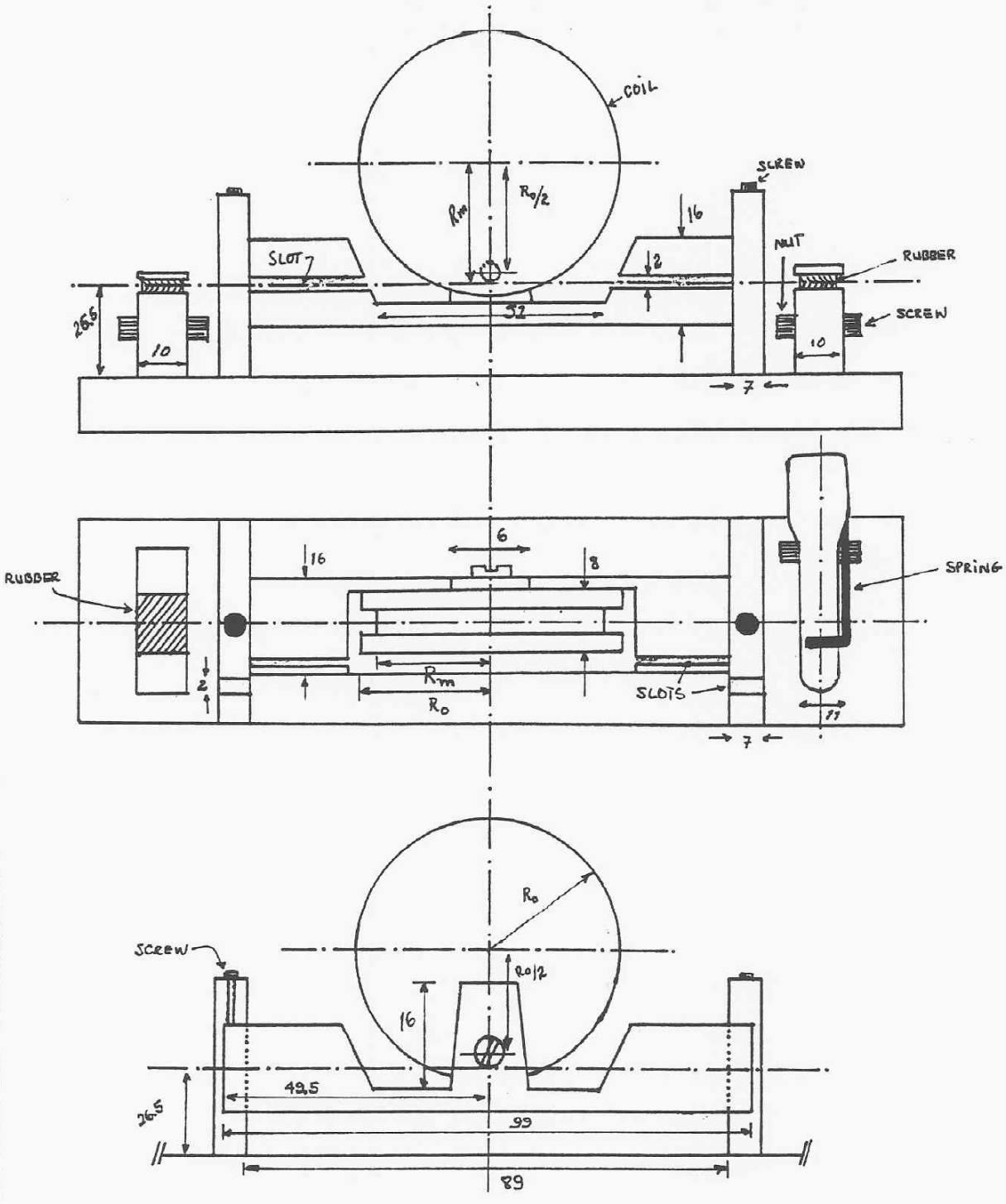

AUTHOR: António Lobo
DATE : MARCH 1991 V.2
UNIVERSITY OF KENT

Appendix B

Servo System Schematic Diagram

The interference pattern which is incident on the photodetector is converted to a voltage signal, through a current/voltage converter (appendix C1) and then fed to one of the inputs of the Lock/Integration block (INPUT). The first stage of this block is a differential operational amplifier [61] which gives zero output voltage when the interferometer is locked at quadrature. The output voltage from the photodetector is compared to a reference voltage (V_{quad}) equal to the mean output voltage of the photodetector (ie, corresponding to the quadrature position). The output error voltage of the differential amplifier is then fed to an integrator with reset [61], then amplified by the high voltage amplifier (HVA) block [61] and fed back to the piezoelectric cylinder in the receiving interferometer. The output signal going to this cylinder represents the correction signal required to keep the phase difference between the interferometer arms at $\pi/2$ radians, and it contains drift, noise, and signal information. The 5 kΩ potentiometers are adjusted to compensate for different currents from different intensities at the two inputs (INPUT and V_{quad}). If we wish to realize a second order type feedback loop, the switch can be changed to the position (B) and a second integrator follows. This second integrator works as a loop RC active low-pass filter with a - 6 dB/oct gain slope below the corner frequency $f_c = (2\pi R_2 C)^{-1}$, and a flat gain above this frequency [61]. The HVA block is a linear amplifier with a gain of 13 and a - 3 dB bandwidth of 50 kHz, and with a class AB push-pull stage [62] in order to produce sufficient current for the piezoelectric cylinder.

The Reset block works as follows: the output of the integrator is rectified by a precision rectifier stage and then compared to a reference voltage (V_{REF}). If the absolute value of the control signal exceeds V_{REF}, a short output pulse from the 555 timers triggers the monostables [61,62]. The first 555 turns on an LED for 0.16 seconds, to indicate that a reset has just taken place. When the system is locked at quadrature, the LED turns off. The other 555, closes two electronic switches (DG308) for a period of time given by $T=1.1\ R_oC_o$.

The switches discharge the capacitors in the intergrators producing the reset. The duration of this pulse (T) must be much larger than the time constant ($\tau = R_1C$) of the integrator.

For the experiment in chapter 2, the values were: R_1 = 220 kΩ, C = 0.86 nF, R_o = 1 MΩ and C_o = 22 nF; for the experiment in chapter 3, they were: R_1 = 10 kΩ, C = 0.22 μF, R_o = 510 kΩ and C_o = 1 μF, and the HVA block was removed. If the tracking range of the system is exceeded, a rapidly responding circuit resets the integrator, and hence the servo output, to zero. The servo then starts a new tracking cycle with the interferometer locked to an arbitrary quadrature point.

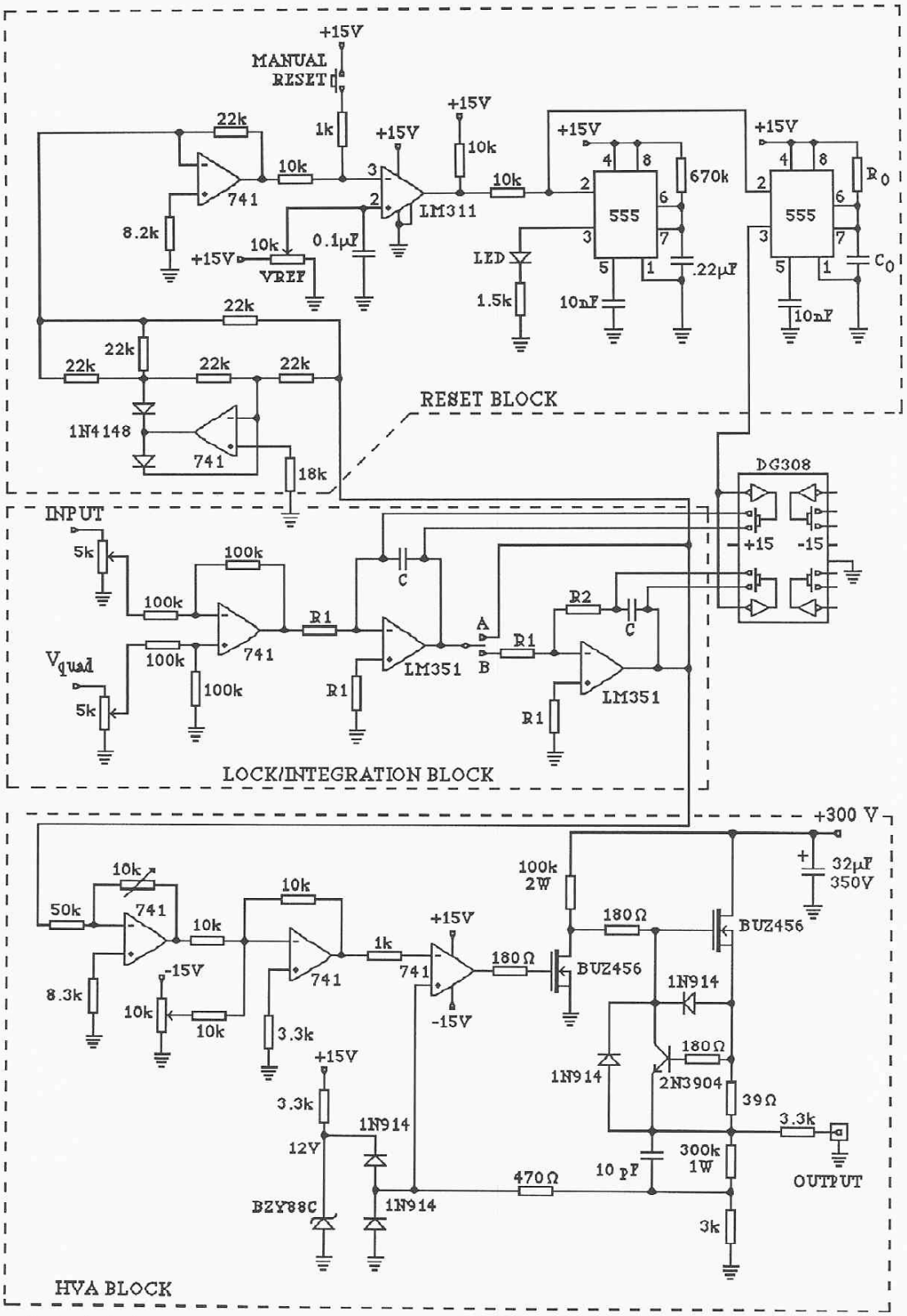
+15V
MANUAL RESET
1k
22k
10k
741
8.2k
LM311
0.1µF
VREF
LED
1.5k
555
670k
.22µF
10nF
R_0
C_0
RESET BLOCK
1N4148
18k
DG308
+15
-15
INPUT
5k
100k
R1
C
R2
A
B
V_{quad}
LM351
LOCK/INTEGRATION BLOCK
+300 V
50k
-15V
8.3k
3.3k
180Ω
BUZ456
1N914
2N3904
39Ω
300k 1W
10 pF
470Ω
12V
BZY88C
OUTPUT
3k
HVA BLOCK
Antonio Lobo
Physics Lab.-Univ.of Kent
9-5-1991 VERSION 1
BUZ456-800B
G D S
Pin View
2N3904
C B E

Appendix C

C1 - Infra-Red Photodetectors for $\lambda = 800$ nm

The photodiode (BPX65) is connected to a transimpedance amplifier (NE5534) in the "photoconductive mode" where the photodiode is reverse biased [63]. This mode of operation gives the fastest response, greatest bandwidth and maximum linearity; however, an increase in the shot noise, a dark current offset and a 1/f noise component will be introduced. The three following amplification stages are used only to produce the desirable gain. For more technical details in designing the photodiode amplifier circuits and their performance improvement, a brief look at reference [63] is useful.

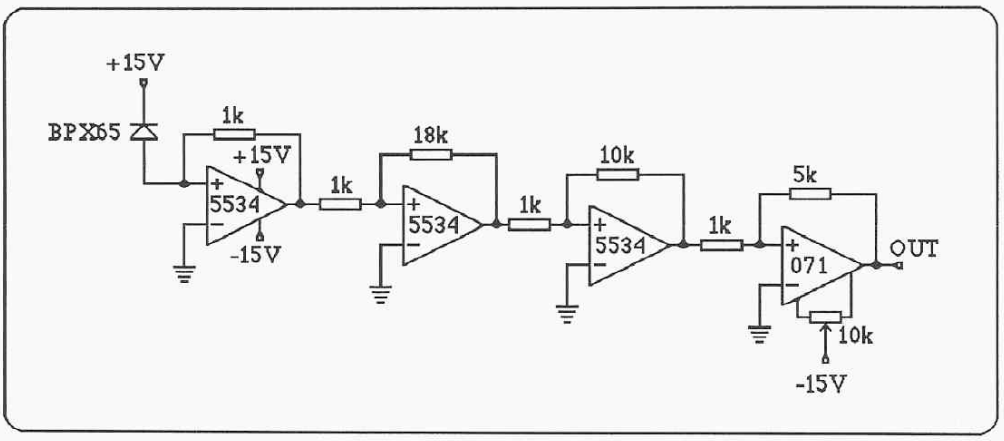

Technical characteristics measured: Gain = 3.9×10^5 V/W

Bandwidth (- 3 dB) ≈ 1.2 MHz

Noise floor = 5.73 $\mu V/\sqrt{Hz}$

C2 - Infra-Red Photodetectors for $\lambda = 1300$ nm

The PIN photodiode (PD7005) is connected in the "photoconductive mode" (as in the previous circuit) to a FET Operational amplifier (OP15) with a small bias current (± 15 pA), in order to achieve the highest sensitivity. A small capacitor across the feedback resistor (in this case, the 8.2 kΩ resistor across OP15) is frequently required to suppress oscillation or gain peaking [63], although it can affect the bandwidth. A small amount of capacitance will usually be required to ensure loop stability. This capacitance is accomplished using a capacitor T-network [63], which is capable of even subpicofarad tunable capacitance with little effect on stray capacitance in the tuning operation. The equivalent capacitance is given by:

$$C_{eq\text{-}tee} = \frac{C_1 C_2}{C_1 + C_2 + C_3} = 0.5 \text{ pF to } 5 \text{ pF}$$

The second stage is used to increase the gain of the circuit. The values for the capacitors used were: $C_1 = C_2 = 8.2$ pF and $C_3 = 5.5/56$ pF.

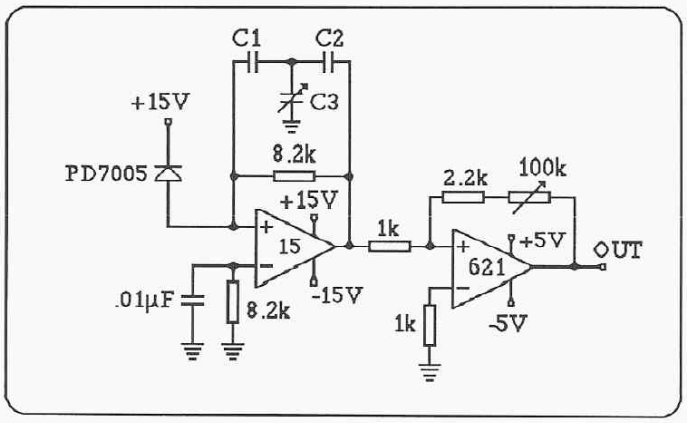

Technical characteristics measured: Gain = 6.94×10^5 V/W

Bandwidth (- 3 dB) ≈ 2.8 MHz

Noise floor = 2.6 μV/√Hz

References

[1] D.A. Jackson, "Monomode Optical Fibre Interferometers for Precision Measurement", J.Physics E: Sci. Instrum., vol.18, p.981 (1985).

[2] D.A. Jackson, J.D.C. Jones,"Fibre Optic Sensors", Optica Acta,vol.33, p.1469 (1985).

[3] P. Cielo, "Fibre Optic Hydrophone: Improved Strain Configuration and Environemental Proctection", Appl. Optics, vol.18, p.2933 (1979).

[4] J.P. Goedgebuer, J. Salcedo, J.C. Vienot, "Multiplex Communication Via Electrooptic Phase Modulation of White Light", Optica Acta, vol.29, p.471 (1982).

[5] S.A. Al-Chalabi, B. Culshaw, D. Davies, "Partially Coherent Sources in Interferometric Sensors", Proc. 1st Int. Conf. on Optical Fibre Sensors, London (1983).

[6] E. Hecht, H. Zajac, *Optics*, Addison-Wesley Publishing, Inc. (1974).

[7] A. Papoulis, *The Fourier Integral and its Applications* , McGraw-Hill (1962).

[8] J.W. Goodman, *Statistical Optics*, Wiley (1985).

[9] A. Yariv, *Introduction to Optical Electronics*, Holt Rinehart and Winston Publishing, Inc.(1971).

[10] A. Siegman, *Lasers*, University Science Books (1986).

[11] J. Goedgebuer, A. Hamed, H. Porte, N. Butterlin, "Analysis of Optical Crosstalk in Coherence Multiplexed Systems Employing a Short Coherence Laser Diode with Arbitrary Power Spectrum", J. Quantum Electron., vol.26, p.1217 (1990).

[12] A.S. Gerges, "Novel Fibre-Optic-Based Interferometric Sensors Exploiting Coherence and Low-Coherence Signal Processing Techniques", Ph.D. Thesis, University of Kent, U.K. (1990).

[13] "Workshop on Single-Mode Optical Fibre Sensor Technology", Course Notes, University of Kent and Sira Ltd., U.K. (1985).

[14] A.R. Reisinger, C. David, K.Lawley, A. Yariv, "Coherence of Room-Temperature CW GaAs/GaAlAs Injection Laser", J. Quantum Electron.,vol.15,p.1382 (1979).

[15] J.L. Santos, D.A. Jackson, "Coherence Sensing of Time Addressed Optical Fibre Sensors Illuminated by an Multimode Laser Diode", Appl. Optics, vol.30, p.5068 (1991).

[16] S.A. Al-Chalabi, B. Culshaw, D. Davies, "Partially Coherent Sources in Interferometric Sensors", Proc. 1st Int. Conf. on Optical Fibre Sensors, London (1983).

[17] F. Farahi, T. Newson, J.C. Jones, D.A. Jackson, "Coherence Multiplexing of Remote Fibre Optic Fabry-Perot Sensing Systems", Optics Commun.,vol.65,p.319 (1988).

[18] A.S. Gerges, F. Farahi, T. Newson, J.C. Jones, D.A. Jackson, "Interferometric Fibre Optic Sensor Using a Short Coherence Length Source", Electronic Lett.,vol.23,p.1110 (1987).

[19] D.A. Jackson, J.C. Jones, *Optical Fibre Sensors vol.2* , Ed. Dakin and Culshaw, Artech House Publishing (1990), Chap.10 - "Interferometers".

[20] Mitsubishi Optoelectronics Data Book (1990).

[21] W. Thomas Cathey, *Optical Information Processing and Holography*, John Wiley & Sons (1974), Chapter 4.

[22] J.L. Santos, D.A. Jackson, "Time Division Multiplexing of Coherence Tuned Optical Fibre Sensors Based Upon a Multimode Laser Diode", Opt. Commun., vol.83, p.37 (1991).

[23] A. Kersey, A. Dandridge, A. Tveten, "Recent Advances in Demodulation/Multiplexing Techniques for Interferometric Fibre Sensors", SPIE vol.734 Fibre Optics´87, Fifth Int. Conference on Fibre Optics and Opto-Electronics, p.261 (1987).

[24] J.P Dakin, "Multiplexed and Distributed Optical Fibre Sensor Systems", J. Phys. E:Scientific Instrum., vol.20, p.954 (1987).

[25] Vernitron Piezoelectric Ceramics Data Book (1969).

[26] G. Martini, "Analysis of a Single-Mode Optical Fibre Piezoceramic Phase Modulator", Optical and Quantum Electronics, vol.19, p.179 (1987).

[27] E. Gray , *American Institute of Physics Handbook*, McGraw-Hill (1972).

[28] J. Zelenka, *Piezoelectric Resonators and Their Applications*, Elsevier Publications, vol.24, Oxford.

[29] A.B.L. Ribeiro, J.L. Santos, D.A. Jackson, "Large Range Coherence Tuned Fibre Optic Interferometric System for Application in Accelerometers", to be published in the Rev. of Sci. Instrum. (1992).

[30] H.C. Lefevre, "Single-Mode Fibre Fractional Wave Devices and Polarization Controllers", Electronics Lett., vol.16, p.778 (1980).

[31] N.G. Walker, G.R. Walker, "Polarization Control for Coherent Communications", J.Lightwave Technology, vol.8, p.438 (1990).

[32] B.G. Koehler, J.E. Bowers, "In-line Single-Mode Fibre Polarization Controllers at 1.55, 1.30 and 0.63 μm", Appl. Optics, vol.24, p.349 (1985).

[33] R. Ulrich, "Polarization Stabilization on Single Mode Fibre", Appl. Physics Lett., vol.35, p.840 (1979).

[34] R. Ulrich, A. Simon, "Polarization Optics of Twisted Single Mode Fibres", Appl. Optics, vol.18, p.2241 (1979).

[35] V. Ramaswamy, R.H. Stolen, M.D. Divino, W. Pleibel, "Birefringence in Elliptically Clad Borosilicate Single Mode Fibres", Appl. Optics, vol.18, p.4080 (1979).

[36] W.A. Shurcliff, *Polarized Light*, Oxford University Press (1962).

[37] D.A. Jackson, R. Priest, A. Dandridge, A.B. Tveten, "Elimination of Drift in Single Mode Optical Fibre Interferometer Using a Piezoelectrically Stretched Coiled Fibre", Appl. Optics, vol.19, p.2926 (1980).

[38] Floyd M. Gardner, *Phaselock Techniques*, 2nd Ed., J. Wiley & Sons (1979).

[39] K. Fritsch, G. Adumovsky, "Simple Circuit for Feedback Stabilisation of a Single Mode Optical Fibre Interferometer", Rev. of Sci. Instrum., vol.52, p.996 (1981).

[40] Shaohuili, B. Chong, Z.P. Zhang, "Phase Tracking System in an Optical Fibre Interferometer", Int. Journal of Optoelectronics, vol.3, p.465 (1988).

[41] Y. Hirose, Y. Tsuzuki, "Stabilization Scheme of Interference Signals in Optical Fibre Sensors by Optical Phase-Looked Loop", Proc. 7th OFS, p.117 (1990).

[42] C. Watts, N. Fürstenau, "Multistable Fibre Optic Michelson Interferometer with Electrooptic Feedback Exhibiting 95 Stable States", J. Quantum Electron., vol.25, p.3 (1989).

[43] D.L. Gardner, S.L. Garrett, "Fibre Optic Seismic Sensor", SPIE vol.838, Fibre Optic and Laser Sensors V, p.271 (1987).

[44] D.L. Gardner, T. Hofler, S.R. Baker, R.K. Yarber, S.L. Garrett, " A Fibre Optic Interferometric Seismometer", J. Lightwave Tech., vol.5, p.953 (1987).

[45] A.D. Kersey, D.A. Jackson, M. Corke, "High-Sensitivity Fibre Optic Accelerometer", Electron. Lett., vol.18, p.559 (1982).

[46] A.M. Yurek, A.B. Tveten, A. Dandridge, "High Performance Fibre Optic Hydrophones in the Artic Environment", Proc. 7th, OFS Conference, Sydney, Australia, p.321 (1990). Inst. of Radio & Electronics Engineers.

[47] Laser Diode Inc., Optilas Limited catalog (1990).

[48] Hitachi Optoelectronic Data Book (1989).

[49] G. Keiser, *Optical Fiber Communications*, 2nd Ed., McGraw-Hill, Inc. (1991).

[50] T. Yoshino, K. Kurosawa, K. Itoh, T. Ose, "Fibre Optic Fabry-Perot Interferometer and Its Sensor Applications", J. Quantum Electron., vol.18, p.1624 (1982).

[51] A.D. Kersey, D.A. Jackson, M. Corke, "A Simple Fibre Fabry-Perot Sensor", Optics Commun., vol.45, p.71 (1983).

[52] C. E. Lee, H. F. Taylor, "Fibre Optic Fabry-Perot Temperature Sensor Using a Low Coherence Light Source", J. Lightwave Tech., vol.9, p.129 (1991).

[53] C. Mariller, M. Lequime, "Fibre Optic 'White-Light' Birefringent Temperature Sensor", SPIE vol.798 Fibre Optic Sensors II, p.121 (1987).

[54] M. Lequime, C. Lecot, "Fibre Optic Pressure and Temperature Sensor for Down-Hole Applications", Fibre Optic Sensors IV Conf. (1990).

[55] J.L. Santos, D.A. Jackson, "Passive Demodulation of Miniature Fibre-Optic-Based Interferometric Sensors Using a Time Multiplexing Technique", Optics Lett., vol.16, p.1210 (1991).

[56] D.J. Webb, J.D.C. Jones, D.A. Jackson, "Interferometric Measurements of Diaphragm Displacements Under Pressure", Internal Technical Report from Applied Optics Group of University of Kent, Canterbury, U.K. (1987).

[57] J.L. Santos, A.P. Leite, D.A. Jackson, "Optical Fibre Sensing with a Low-Finesse Fabry-Perot Cavity", Submitted to Appl. Optics (1992).

[58] R.H. Wentworth, "Theoretical Noise Performance of Coherence-Multiplexed Interferometric Sensors", J. Lightwave Tech., vol.7, p.941 (1989).

[59] A.P. Leite, J.L. Santos, M.V. Moreira, A.L. Ribeiro, A.Cunha, Project NOSCA - Task 2/Sub-Task 2.5, Internal Report of INESC - Porto (1991).

[60] M. Lequime, C. Lecot, "A Dual-Wavelength Passive Homodyne Detection Unit for Fibre-Coupled White-Light Interferomters", SPIE vol.1267 Fiber Optic Sensors IV, p.288, (1990).

[61] P. Horowitz, W. Hill, *The Art of Electronics*, 2nd Ed., Cambridge Univ. Press.

[62] M. Hartley Jones, *A Pratical Introduction to Electronic Circuits*, 2nd Ed., Cambridge Univ. Press (1985).

[63] Burr-Brown, *The Handbook of Linear IC Applications*, Burr-Brown Inc. Technical Books, p.182 (1985).

[64] S. Chen, A.J. Rogers, B.T. Meggitt, "Electronically-Scanned White-Light Interferometry with Enhanced Dynamic Range", Electron. Lett., vol.26, p.1663 (1990).

[65] S. Chen, A.J. Rogers, B.T. Meggitt, "Electronically Scanned Optical-Fibre Young´s White-Light Interferometer", Optics Lett., vol.16, p.761 (1991).

[66] S. Chen, A.W. Palmer, K.T.V. Grattan, B.T. Meggitt, S. Martin, "Study of Electronically-Scanned Optical-Fibre White-Light Fizeau Interferometer", Electron. Lett., vol.27, p.1032 (1991).